

DISSERTATION

INVESTIGATIONS OF THE EFFECTIVE TEMPERATURE OF SHEARED COLLOIDS AND
DYNAMIC BEHAVIOR OF GLASS-FORMING LIQUIDS

Submitted by

Min Zhang

Department of Chemistry

In partial fulfillment of the requirements

For the Degree of Doctor of Philosophy

Colorado State University

Fort Collins, Colorado

Spring 2013

Doctoral Committee:

Advisor: Grzegorz Szamel

Branka Ladanyi

Elliot Bernstein

Eugene Chen

R. Mark Bradley

Copyright by Min Zhang 2013

All rights reserved

ABSTRACT

INVESTIGATIONS OF THE EFFECTIVE TEMPERATURE OF SHEARED COLLOIDS AND DYNAMIC BEHAVIOR OF GLASS-FORMING LIQUIDS

There are three projects in my dissertation. In chapter 2, a simple colloidal suspension under shear is studied. Four different methods are used to define the so-called effective temperature. The effective temperature calculated from the extended fluctuation-dissipation theorem is independent of the choice of the observables, and it controls the density distribution profiles. All the effective temperatures are larger than the bath temperatures. The effective temperature along the velocity gradient direction is somewhat larger than that along the vorticity direction. In chapter 3, a binary Lennard-Jones mixture at different temperatures is investigated. Due to the presence of shear flow, the ergodicity is recovered when the temperature is below glass transition. The dynamic behavior of the system is investigated. Above the glass transition, the dynamics is primarily controlled by the temperature, while below the glass transition, shear flow plays a dominant role. The violation of the Stokes Einstein relation, as well as the exponential tails in the self-part of the van Hove function are observed. In chapter 4, a binary hard-sphere mixture is researched. Four-point correlation functions are calculated, which suggest the presence of dynamic heterogeneity. To calculate four-point correlation functions, we need to specify the ‘measuring stick’ (the parameter a in the overlap function $F_o(a, t)$). When a is large enough, the four-point susceptibility at the structural relaxation time is independent of the choice of a . The dynamic correlation length is estimated from the Ornstein-Zernike fits for the four-point structure factor. We speculate that the maximum value of the dynamic correlation length is also independent of the ‘measuring stick’.

ACKNOWLEDGEMENT

I am sincerely and heartily grateful to my advisor, Professor Grzegorz Szamel for his guidance, encouragement, support and patience over the years. He not only taught me the knowledge and techniques in this field, but also let me know how to research, how to think scientifically. He helped me come up with all the topics in the dissertation and guided me through the whole process of development. This dissertation would not have been possible without his help.

I would like to express sincere gratitude to my committee members Professor Branka Ladanyi, Professor Elliot Bernstein, Professor Eugene Chen, and Professor Mark Bradley for their guidance. Professor Branka Ladanyi devoted a lot of time to reading my dissertation. She provided numerous helpful suggestions, which are precious to me. Professor Elliot Bernstein introduced me to Colorado State University seven years ago. I spent very important years of my life in Colorado. Many inspiring questions asked by Professor Mark Bradley and Professor Eugene Chen motivated me to broaden my view and to rethink my projects in different ways.

I am grateful to Dr. Elijah Flenner for many valuable discussions on the subject of four-point correlation functions and dynamic correlation length. I would like to thank a former member in Professor Szamel's group, Dr. Prasanth Jose for sharing his simulation code and help me develop a Brownian dynamics program for the simulation of a colloidal suspension. I am so lucky to have been working with these wonderful people. It is a great pleasure to thank everyone who helped me write my dissertation successfully. I want to give special thanks to my friend Dongmei Zhang. She helped me a lot when I was not on campus.

TABLE OF CONTENTS

Abstract	ii
Acknowledgement	iii
1 Introduction	1
1.1 Nonequilibrium systems	1
1.1.1 Aging glass	2
1.1.2 Nonequilibrium stationary state and shear flow	3
1.1.3 Effective temperatures	6
1.2 Glasses	8
1.2.1 How to form glasses	8
1.2.2 Dynamic behavior of supercooled liquids	10
1.2.3 Glass formers	14
1.3 Approaches for research	15
1.3.1 Theories	15
1.3.2 Experiments	20
1.3.3 Simulations	22
1.4 Organization of the dissertation	28
2 Effective temperatures in a sheared colloidal suspension	35
2.1 Introduction	35
2.2 Simulation	38
2.3 Static structure of a sheared simple liquid	40
2.3.1 Pair distribution function	40
2.3.2 Static structure factors	43
2.4 Effective temperatures	46
2.4.1 From the Einstein relation	47
2.4.2 Fluctuation-dissipation violation	50
2.4.3 Static linear response function	56
2.4.4 Density distribution fit	60
2.5 Discussion	64

3	Supercooled liquids and glasses under shear	73
3.1	Introduction	73
3.2	Simulations	74
3.3	Static structure of the binary Lennard-Jones system under shear	76
3.3.1	Pair distribution function	76
3.3.2	Static structure factor	80
3.4	Dynamical behavior of a sheared binary Lennard-Jones system	83
3.4.1	Mean square displacement	83
3.4.2	Diffusion coefficient	87
3.4.3	Self-intermediate scattering function	91
3.4.4	Structural relaxation time	94
3.4.5	Breakdown of Stokes-Einstein relation	97
3.4.6	Van Hove function	100
3.5	Discussion	104
4	Dynamic heterogeneity and dynamic correlation length in a hard-sphere glass former	109
4.1	Introduction	109
4.2	Simulation	111
4.3	Results	112
4.3.1	Overlap function	112
4.3.2	Structural relaxation time	115
4.3.3	Four-point susceptibility	119
4.3.4	Four-point structure factor	123
4.3.5	Dynamical correlation length	128
4.3.6	Four-point pair correlation function	130
4.4	Discussion	132
5	Summary	136
5.1	Effective temperatures of nonequilibrium systems	136
5.2	Dynamic behavior of glass-forming liquids	137

Chapter 1

Introduction

In the first chapter of the dissertation, two very important topics will be introduced. The first topic, which is concerned with the nonequilibrium states and the notion of effective temperature, is discussed in the first section. The second one is about glasses and the glass transition, as well as supercooled liquids. They are discussed in the second section. The third section will be devoted to discussing briefly some theories and common approaches to study the aforementioned subjects. The organization of the whole dissertation will be outlined in the last section.

1.1 Nonequilibrium systems

No physical system is ever in thermodynamical equilibrium. (Cugliandolo [1])

For an equilibrium system, time translational invariance (TTI) is valid; thus the one-time physical properties such as pressure or volume can be described statistically without considering the time evolution [2]. Consider two observables $A(t)$ and $B(t)$, their two-time correlation function is defined as,

$$C_{AB}(\tau) \equiv \langle A(t)B(t_w) \rangle - \langle A(t) \rangle \langle B(t_w) \rangle , \quad (1.1)$$

where τ is the time interval $\tau = t - t_w$. Suppose that a time-dependent perturbation $h_B B(t)$ is imposed on the system from time $t = t_w$, then the new Hamiltonian is,

$$H = H_0 + h_B B(t) . \quad (1.2)$$

The response function due to the perturbation is [1, 3],

$$R_{AB}(\tau) \equiv \frac{\delta \langle A(t) \rangle}{\delta h_B(t_w)} . \quad (1.3)$$

Integrating $R_{AB}(t)$ between times 0 and t , we can define the susceptibility $\chi_{AB}(t)$ as [1],

$$\chi_{AB}(t) \equiv \int_0^t dt' R_{AB}(t') . \quad (1.4)$$

In the linear response regime, correlation function and response function satisfy the fluctuation-dissipation theorem (FDT) [1, 4],

$$R_{AB}(\tau) = \frac{1}{T} \frac{\partial C_{AB}(\tau)}{\partial t_w} . \quad (1.5)$$

FDT can also be expressed as,

$$\chi_{AB}(\tau) = \frac{1}{T} [C_{AB}(0) - C_{AB}(\tau)] . \quad (1.6)$$

On the contrary, the situation for a nonequilibrium system is very complicated. First the definition of temperature is questionable. Basically, one cannot define a universal time-independent temperature for a nonequilibrium system as people usually do for the equilibrium cases. It is commonly accepted that the concept ‘effective temperature’ may be used to substitute the ordinary temperature. However, the definitions of the effective temperatures are probably different from case to case, and the calculated values T_{eff} depend on the observables [1]. In addition, the effective temperatures also vary with time, at least, are different within distinct time scales [1, 5]. Secondly, when the system is out of equilibrium, time translational invariance may no longer be valid, the dynamic behavior is hard to analyze. Correlation functions and response functions are not only dependent on the time interval t , but also depend on the two times t_0 and $t_0 + t$ individually [6]. The fluctuation-dissipation theorem is no longer valid. Although intensive investigations have been performed [1, 2, 5, 6], nonequilibrium systems have not been understood very well.

In this section, we will focus on two important nonequilibrium systems, aging glass and stationary nonequilibrium states. Then we will introduce the notion of ‘effective temperature’ in these two nonequilibrium situations.

1.1.1 Aging glass

When a liquid is suddenly quenched to a temperature below the glass transition temperature T_g , the equilibrium relaxation time becomes very large, the system cannot reach an equilibrium state on experimental time scales [7, 8]. Physical properties of the glass will evolve very slowly and depend on waiting time t_w , the time spent after quenching. This phenomenon is called ‘aging’ [7, 8]. For an aging system, time translational invariance (TTI) is violated. The ‘one-time’ quantities, such as energy, density etc. change very slowly with t_w [7, 9]. With those one-time observables, one cannot obtain much information about the aging behavior [9], because these quantities evolve very slowly [7]. Usually the two-time dependent quantities are used, such

as time correlation functions and response functions [9]. Unlike equilibrium cases, those functions in aging systems are not only dependent on the time interval $\tau = t - t_w$, but also depend on t and t_w separately [6]. In the aging regime, the relaxation time, which is often estimated from the time-dependent correlation function, increases with waiting time [5, 7]. As soon as the liquid is quenched into a glass, the motion of particles are still quite large. Thus the system relaxes quickly and the relaxation time is small. As the system ages (t_w increases), particles move more slowly, causing the growth of the relaxation time. Finally, the relaxation time will exceed experimental time scale and the glass is formed [7]. This procedure can be explained by the trap model introduced by Bouchaud and Monthus [10]. Generally speaking, this model assumes that there are many distributed potential wells on the energy landscape. An equilibrium system may be temporarily trapped in a well and then escapes [10]. On the contrary, if a liquid is quenched into a glass state, the depth of well become larger when the age of the system increases. As a result, the system has to spend longer time in the well before getting out, implying that the relaxation time is enhanced [7, 10]. Eventually, when the waiting time is large enough, the particles cannot escape from the traps during experimental time window and the glass transition is completed.

Since an aging glass remembers its complete history (t_w), or more generally speaking, the physical properties of the system depend on how the glass was created [1, 7], it is reasonable to expect that some characteristics of the glass can be adjusted by using different ways to produce the glass [7]. This speculation was demonstrated by Swallen et al. [11]. They prepared an organic glass in two methods, the first one is by quenching the liquid suddenly, the second one is via the vapor deposition with a low deposition rate. Then they carefully compared many physical properties of these two samples, and found that the vapor-deposited glass has some salient features, such as larger density, higher kinetic and thermodynamic stability. The vapor deposition technique which can create more stable glass may be used in pharmaceuticals [11].

Before closing this subsection, it is worth pointing out that the aging process can be stopped by an external driving force (such as shear), and a stationary state can be reached [5, 7]. Both the dynamic correlation functions and response function in the steady state are time translationally invariant [5]. Due to the drive, the system can overcome the free energy barriers more easily [12], and the structure relaxes faster. The structural relaxation time depends on both the temperature and the strength of drive. In chapter 3, we will show that below the glass transition shear controls the dynamics of the system primarily.

1.1.2 Nonequilibrium stationary state and shear flow

Now let us discuss one very important example of a nonequilibrium case, namely, the steady state. Compared with aging systems we discussed above, nonequilibrium stationary systems have a remarkable

feature: time translational invariance is recovered [1, 13]. As a consequence, the macroscopic observables, such as density, volume etc. are independent of time [14]. Moreover the two-time correlation functions, as well as the response functions are only dependent on the time intervals [1], making it easier to study nonequilibrium stationary systems by numerical simulations or experiments [13]. Furthermore, stationary systems also exhibit similar behavior as aging systems, such as the effective temperatures [1, 5].

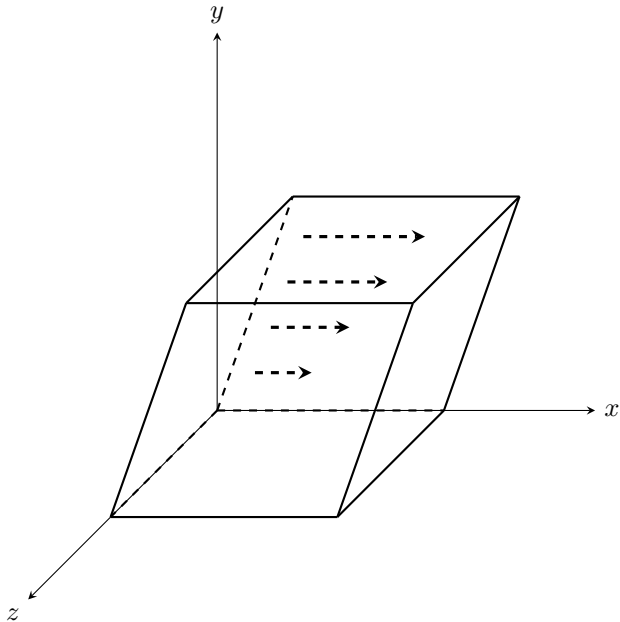


Figure 1.1: A schematic figure illustrating a system under shear. The flow is along \hat{e}_x direction, and the velocity gradient is in the \hat{e}_y direction. The sizes and shapes of all kinds of particles vary for different systems and are not shown in the figure.

There are many ways to generate a stationary state, such as heat conduction, electrical conduction and shear [14]. Since in our work we mainly created the systems at stationary state by imposing a steady shear flow characterized by the shear rate $\dot{\gamma}$ (a gradient of velocity [15]), we will only consider this generic situation here. Figure 1.1 shows how we applied shear on the systems. Specifically, in chapter 2, we will impose moderate and high shear rates on a monodisperse colloidal suspension. Particles in the system interact with one another via a pairwise additive, repulsive screened Coulomb potential [16]. In chapter 3, we will apply a very small shear to a binary Lennard-Jones system (Kob-Andersen model) with the temperatures in the range from 0 to 0.6 (temperatures are expressed in the reduced units for Lennard-Jones potential).

The first order melting transition due to shear was first observed in colloidal crystals [17, 18]. Later it was found that colloidal glasses can also be melted by the imposed shear [19, 20]. In the glassy state, the ergodicity is broken, particles are trapped in the cages formed by their neighbors. With the help of shear, the nonergodic arrest is prohibited, and the particles can escape from the cages, moving like those

in liquids [21, 22]. In this case, the glass is fluidized [18], and arrives at a stationary state eventually [21]. Recently by investigating the dynamic behavior of colloidal suspensions under shear, Eisenmann et al. [18] found that the shear induced melting procedure is very similar to the cases that the glass is melted by increasing temperature or by decreasing volume fraction. In chapter 3, we will show that even a very small shear can destroy the glass phase.

On the other hand, above the glass transition, a small shear cannot drive a system out of equilibrium [8] and the linear response relation still holds. When the shear rate is large enough, a steady state can be generated. More than twenty years ago, Hess, Hanley and collaborators have investigated the shear-dependent structures in many kinds of liquids by theoretical analysis [23, 24], computer simulations [25, 26], and experiments [27]. The structure distortion (anisotropy) in the fluids under shear has been observed with the help of the pair distribution function and the static structure factor. It is commonly accepted that the rheological behavior of sheared liquids can be related to the shear-induced change in the structure of the system [28]. Here we briefly introduce some very important rheological phenomena due to shear. Now they are quite popular topics in this field. The influence of shear on the effective temperatures will be discussed in the following part.

Shear thinning In the Newtonian regime, the viscosity of a fluid remains constant when the imposed shear rate is increased, while it varies outside the Newtonian regime [27]. The notion of ‘shear thinning’ means that the viscosity and the relaxation time decrease with increasing shear rate (or generally speaking the driven force [5]). This phenomenon has been observed in many different systems, such as supercooled liquids [29], colloidal suspensions [30], polymers [31] and gels, [5] etc. Shear thinning is easy to understand in the context of phase-space energy landscape. Without shear, the motion of particles in a system are retarded by the energy barriers. On the contrary, with the help of shear, the displacements of particles are enhanced and the system becomes more fluid [32]. Actually, shear thinning is widely present in our daily life. For example, if one squeezes a tube of paint, it will flow and come out. On the other hand, without a driven force, the paint will stay on the wall without flowing [33].

Shear thickening In contrast to shear thinning, shear thickening denotes that the viscosity grows, sometimes discontinuously, with increasing shear rate [34]. The shear-thickened materials have wide applications in industry. For example, by adding some polymers of surfactant in the fluids flowing in the cylinder pipes, the turbulent friction near the solid surface can be decreased effectively, reducing the energy consumption [35, 36]. So far, a fully theoretical understanding of shear thickening, especially for the case of the dilute solution, is still an open question [37]. Some models and explanations for shear thickening have been reviewed by Cates and Fielding [38].

Shear banding Besides shear thinning and thickening, some materials split into several bands with different apparent viscosities when shear is imposed [37, 39]. This phenomenon is called shear banding, which is believed to be concomitant with the shear-induced transitions for the structures of the fluids [40, 41]. Shear banding can take place in many complex fluids, such as colloidal suspensions, foams, polymer solutions, wormlike micelles, etc. [37, 42]. The shear bands are not stable [37], and the reasons for the instability are not clear yet. Recently, the shear-banding phenomenon attracts a lot of interest [37, 39]

1.1.3 Effective temperatures

For a system in an equilibrium state, temperature plays a very important role in describing the thermodynamic properties [43]. Moreover it links the fluctuations of physical quantities and the response due to a small external perturbation via the fluctuation-dissipation theorem (FDT) [4]. FDT can be formulated in different ways, including Einstein relation relating mobility to self-diffusion coefficient, Nyquist’s formula which links electrical resistance to voltage noise [6, 44], and Green-Kubo relation connecting the corresponding conductivities to the current fluctuations [45]. Considering different observables, a specific form of FDT is chosen to study the system [4].

On the other hand, for nonequilibrium systems, the issue becomes very complicated. The usual concepts of equilibrium thermodynamics do not apply for nonequilibrium systems [1], and an ‘ordinary’ temperature of a nonequilibrium system can not be defined. Moreover, the fluctuation-dissipation theorem is violated. Cugliandolo et al. [1] studied two nonequilibrium cases mentioned above, namely, driven stationary systems and aging glasses. In a driven stationary system, equilibrium tends to recover when the strength of external driving force D goes to zero. In an aging system, the waiting time t_w plays the same role as D . Cugliandolo and coworkers [1] propose a so-called ‘effective temperature’ T_{eff} for nonequilibrium systems. They argued that T_{eff} deserves the name ‘temperature’ because it controls the direction of a heat flux [1], energy will transfer from a system at a higher effective temperature to the one at a lower T_{eff} . The effective temperature has several important features. First, it depends on the observation time scale. Second, the formulas for the FDT (equations 1.5 and 1.6) are still valid within each time scale if the effective temperature is used. For example, for aging systems one can simply have [1],

$$R_{AB}(t, t_w) = \frac{1}{T_{\text{eff}}(t, t_w)} \frac{\partial C_{AB}(t, t_w)}{\partial t_w}. \quad (1.7)$$

Later on, this generalized fluctuation-dissipation theorem is widely used to calculate the effective temperatures in nonequilibrium systems, such as sheared stationary states.

After Cugliandolo et al. [1] proposed the concept of ‘effective temperature’ for the nonequilibrium system, many efforts have been devoted to investigating the effective temperatures in different systems, i.e. glasses [44], jamming scenario [46], granular materials [47], etc. by the methods of numerical simulations [47], experiments [44] and also theoretical analysis [2, 5, 6, 48]. Berthier et al. [5, 8, 13] imposed a steady shear on a binary Lennard-Jones mixture to generate a stationary state. They studied the system at different temperatures, ranging from the glass state to the supercooled state. In the glass, due to the imposed shear aging is stopped and a stationary state is reached eventually [5, 7]. The dynamic quantities, such as the two-time correlation functions and response functions behave in a way similar to those in supercooled liquids [8]. From the modified fluctuation-dissipation theorem, the effective temperatures were calculated [8, 13]. The values of T_{eff} are not the same in different time scales. On a short time scale the effective temperature coincides with the bath one, while on a long time scale the effective temperature is higher than the bath one. (Usually when the ‘effective temperature’ is mentioned, it stands for the long time scale effective temperature.) When shear rate is increased, the effective temperature goes up. On the other hand, in supercooled liquids, the system is equilibrium and the fluctuation-dissipation theorem is valid until the shear rate is large enough. With high shear, the system is out of the Newtonian regime and the two-temperature pattern is also observed [13]. The effective temperature for the slow mode is higher than the bath one, while for the fast mode the FDT holds [5, 8, 13]. Maybe most importantly, they found that the effective temperatures calculated by the generalized FDT definition are not dependent on the choice of observables for the nonequilibrium stationary system [13].

All the effective temperatures we mentioned above are related to the dynamical quantities, namely, the time dependent correlation functions and response functions. Liu and Nagel et al. [46, 49] tried to define the effective temperatures via the static linear response. They found with some observables (such as pressure, shear stress, etc.), the calculated effective temperatures are comparable with the results obtained from the generalized fluctuation-dissipation relation. However, with some other quantities, such as the diffusion coefficient, this method did not work well. Their finding raised a question: in which situation can the static linear response be used to define the effective temperature? To the best of my knowledge, there is not a satisfactory answer to this question so far.

Some other attempts have also been made to define and calculate the effective temperatures for nonequilibrium systems. For example, Hayashi et al. [45] studied the effective temperature outside the linear response regime. By the generalized Einstein relation, they calculated the effective temperature in a nonequilibrium Langevin system, which was used as a thermometer to measure the temperature in a Hamiltonian system. They found that the kinetic temperature in the Hamiltonian system is indeed equal to the effective temperature of the thermometer.

Recently, several investigations of effective temperature suggest that the effective temperature may control some quantities of a system. Lu et al. [50] studied the effective temperature in a gene network and showed that the energy flow between the biochemical species is controlled by the effective temperature and also it may help to understand the reasons for the noises in the stochastic cell biology. Ilg and Barrat [51] found that the effective temperature defined by the fluctuation-dissipation theorem can determine the reaction rates in their glassy system under shear.

Despite much progress, we are still far from understanding the effective temperatures completely. Many issues have not been resolved so far. For example, is it possible to define a universal effective temperature regardless the details of various systems? If this kind of temperature exists, how to define it? How to use the effective temperature to calculate the thermodynamic quantities in nonequilibrium systems?

In chapter 2, we will calculate the effective temperatures in a simple monodisperse colloidal suspension with four different definitions. Two of them are based on the generalized fluctuation-dissipation theorem, the other two are from the static response relations. More details will be given at the end of this chapter.

1.2 Glasses

The deepest and most interesting unsolved problem in solid state theory is probably the nature of glass and the glass transition. (Anderson [52])

Glasses are widely used in everyday life, the windows, mirrors, bottles, fish tanks, lenses in the cameras, etc. In industry, various glasses with desired mechanical or optical properties are produced [7]. Although the history of creating glass can be traced back to thousands years ago [53], till now the nature of the glass is still a conundrum and cannot be explained by classical statistical mechanics and solid state theory [53]. According to everyday experience, glasses are rigid solids as crystals, however, essentially they are totally different. As we know, crystals have the periodic structures and are very stable, while glasses have amorphous configuration [53] like liquids. It is very surprising that glasses can also be mechanically rigid as crystals, but without periodic arrangement of the particles [7, 53, 54]. To understand the behavior of glasses, it is important to figure out how a glass is formed. In this section, we will mainly discuss the dynamics in supercooled liquids close to the glass transition.

1.2.1 How to form glasses

In an ‘ordinary’ situation (as we have learned from most textbooks on the liquids and solids), when a liquid is cooled down or compressed, a first-order transition happens and the liquid transforms into a

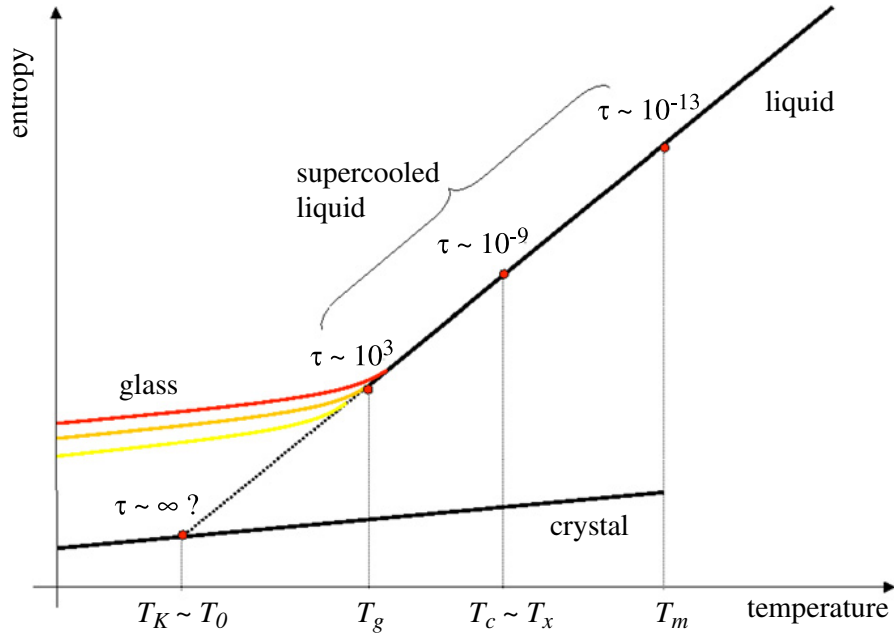


Figure 1.2: The evolution of the entropy as the temperature decreases. A comparison is made between glass transition and crystallization. In the figure τ is the relaxation time. Along the x axis, different critical temperatures are labeled. Specifically, T_m is the melting temperature, at which the first-order transition happens. T_c is the critical temperature predicted by the mode coupling theory. T_x is the Goldstein temperature, the thermal activation becomes important in the dynamics when $T \leq T_x$. T_g is the dynamic glass transition, at which the relaxation time is larger than 10^3 s. T_k is the Kauzmann temperature, at which the excess entropy extrapolates to zero. T_0 is the temperature at which a Vogel-Fulcher-Tamman (VFT) fit of the relaxation time diverges. Figure is adapted from reference [55].

crystalline state [56]. During this procedure, both symmetry and ergodicity are broken, the formed solid is a periodic crystal [53, 57]. The sudden appearance of the long-range order at a certain temperature causes the discontinuities of some thermodynamic quantities, such as the density and the entropy [53, 56]

On the other hand, if a liquid is suddenly quenched to a temperature below its glass transition temperature T_g , an amorphous solid is formed, which is called glass [7, 56, 58]. Crystallization is avoided due to large cooling rate (the cooling rate is about 0.1 – 100 K/min in the experiments). T_g is not a phase transition temperature, it is a purely conventional point, which depends on glass preparation and timescale in our experiments [7, 55, 57]. In practice, the glass transition temperature T_g is defined when the viscosity of the system is about 10^{13} Poise [7]. T_g is smaller than the melting point T_m , at which the liquid-crystal transition occurs [55]. The amorphous material at a temperature between T_g and T_m is called supercooled liquid. As the temperature is reduced, the structural relaxation time also grows dramatically, becomes $10^{14} - 10^{16}$ times larger than that at the melting temperature (see figure 1.2) [7, 55]. The temperature dependence of the α -relaxation time (as well as the viscosity) can be fitted by the Vogel-Fulcher-Tamman law (VFT) very

well [7],

$$\tau_\alpha = \tau_0 \exp\left(\frac{DT_0}{T - T_0}\right). \quad (1.8)$$

In the equation, D is a constant and has different values for different glass formers [53]. τ_0 and T_0 are fitting parameters. According to this equation, the α -relaxation time diverges at T_0 [7].

As illustrated by figure 1.2, the entropy of supercooled liquid decreases continuously with reducing temperature, but it is always higher than that of the corresponding crystal. The difference is called excess entropy, which is extrapolated to zero at a finite temperature, denoted as T_K (Kauzmann temperature) [7, 53]. It is remarkable that for most materials T_K is found to be close to T_0 . Only for few samples, T_K and T_0 are observed different, but the discrepancy is not larger than 20% [7]. A clear conclusion that these two temperatures are the same is still missing. It would be extraordinary if this can be confirmed. In that case the thermodynamics and dynamics of glasses appear be linked [7, 55].

Before leaving this subsection, two more points need to be mentioned. First, although the glass is mechanically stable, it still tends to recover the ergodicity. The relaxation towards an equilibrium state never stops, but the relaxation time is very long, i.e. longer than millions of years [7, 53]. The physical properties of the glass depend on its ‘age’. This phenomenon is named ‘aging’. Secondly, in contrast to the liquid-crystal transition, when a liquid transforms into a glass state, the static structure is hardly changed, but the dynamic behavior varies strikingly [7, 56, 59], which is the topic of next subsection.

1.2.2 Dynamic behavior of supercooled liquids

When cooled down or compressed quickly enough, many different systems can undergo the glass transition, such as molecular supercooled liquids, colloidal suspensions, polymers, biomaterials, metals, and molten salts, etc. [60]. Although these materials have different properties, they exhibit similar dynamic behavior during the glass transition [60]. In this subsection, we will mainly introduce two important phenomena in supercooled liquids approaching the glass transition, namely, the two-step relaxation and dynamic heterogeneity.

Two steps relaxation

To investigate the dynamic behavior of a system, the two-time correlation functions are often used. Among them, the self-intermediate scattering function $F_s(k, t)$ is widely exploited, since it can be measured from both experiments and simulations [13, 62]. $F_s(k, t)$ can be expressed as,

$$F_s(\mathbf{k}; t) = \frac{1}{N} \left\langle \sum_{i=1}^N \exp\{i\mathbf{k} \cdot [\mathbf{r}_i(t) - \mathbf{r}_i(0)]\} \right\rangle, \quad (1.9)$$

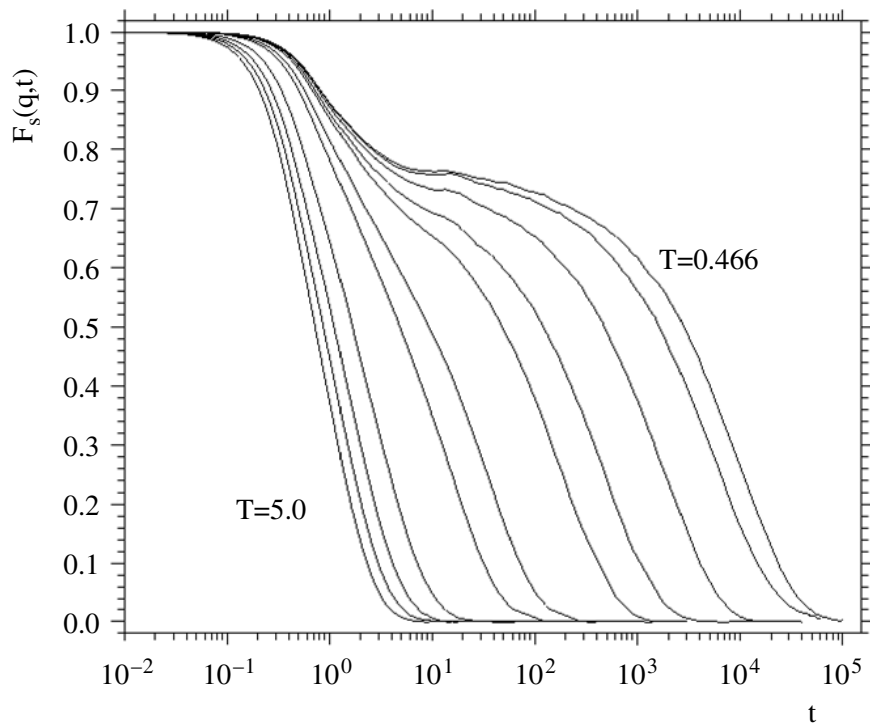


Figure 1.3: The self-intermediate scattering function in a binary Lennard-Jones system at different temperatures. The temperatures from left to right are $T = 5.0, 4.0, 3.0, 2.0, 1.0, 0.8, 0.6, 0.55, 0.5, 0.475, 0.466$. (Temperatures are expressed in the reduced units for Lennard-Jones potential, and the details will be discussed in chapter 3.) When the temperature is high ($T \geq 1.0$) the decay is simply exponential. A two-step relaxation happens in supercooled liquids ($T \leq 0.8$). Figure is adapted from reference [61].

where N is the total number of particles in the sample and where $\mathbf{r}_i(t)$ is the coordinate of the i th particle at time t . From the self-intermediate scattering function an α -relaxation time τ_α can be defined as,

$$F_s(\mathbf{k}; \tau_\alpha) = e^{-1} . \quad (1.10)$$

Figure 1.3, published by Kob and Andersen [61], gives a typical example of the evolution of $F_s(k, t)$ when a system approaches the glass transition. At high temperature $F_s(k, t)$ decays to zero exponentially. When temperature decreases, the relaxation in $F_s(k, t)$ is gradually separated by a plateau. The decay is no longer purely exponential. As the supercooled liquid becomes closer to the glass transition, the time that the plateau lasts increases rapidly, causing the intensive growth of τ_α [55, 61]

To understand the two-step relaxation in the self-intermediate scattering function, it is helpful to connect this phenomenon to the fact that a plateau also exists in the plot of mean square displacement (MSD), (see figure 1.4 which was composed by Kob and Andersen [63]). The behavior of MSD can be explained by the so-called cage effect directly. At the very beginning, the particles move ballistically in the case of Newtonian

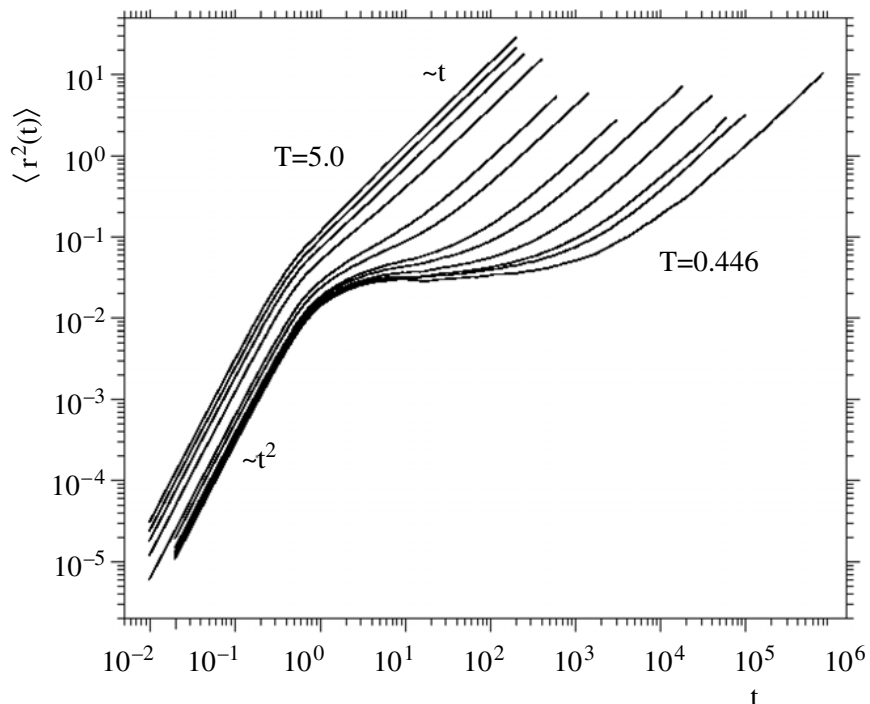


Figure 1.4: The mean square displacement in a binary Lennard-Jones system at different temperatures. The temperatures from left to right are $T = 5.0, 4.0, 3.0, 2.0, 1.0, 0.8, 0.6, 0.55, 0.5, 0.475, 0.466$. (Temperatures are expressed in the reduced units for Lennard-Jones potential, and the details will be discussed in chapter 3.) When the temperature is high ($T \geq 1.0$) a ballistic transport crosses over into a diffusive motion immediately. A plateau occurs and separates the two regimes when temperature is low ($T \leq 0.8$). Figure is adapted from reference [63].

dynamics, (for Brownian dynamics simulations, it is different, which will be described in chapter 3). The ballistic regime is followed by a plateau, where particles are trapped in the cages formed by their neighbors, only some vibrations around their positions can take place. Finally, particles can get rid of the cages and enter into a diffusive regime [55, 63]. The slow relaxation towards plateau in $F_s(k, t)$ can be related to the vibrations in the cage. When temperature is lowered, the particle needs longer time to get out of the cage. In other words, the relaxation time grows [55]. The plateaus in both $F_s(k, t)$ and MSD become longer.

Dynamic heterogeneity

Near the glass transition, the dynamics in supercooled liquid is spatially heterogeneous. It means that dynamics in one region may be strikingly distinct from dynamics in other parts of the system [64]. Dynamical heterogeneity plays a key role to understand the transport properties in supercooled liquids and the kinetics of chemical reactions [64]. In recent years, it is a central subject of glass-forming liquids and attracts intensive research activities [7, 64, 65, 66]. Here we briefly discuss three aspects about the heterogeneous dynamics:

the stretched exponential decay in the self-intermediate scattering function; the violation of Stokes-Einstein relation; the growth of dynamic length scales.

Stretched exponential As shown in figure 1, Kob and Andersen found when the system is approaching the glass transition, in addition to the two-step relaxation, the long time relaxation (beyond the plateau) is not exponential, but exhibits stretched exponential behavior, which can be described by the Kohlrausch-Williams-Watts (KWW) function,

$$\phi(t) \approx A \exp [-(t/\tau)^\beta] . \quad (1.11)$$

The exponent β equals 1 for the liquids at high temperature ($T \geq 1.0$), and in the supercooled regime it decreases as T is reduced [55, 61]. This phenomenon is usually ascribed to dynamic heterogeneity. One common explanation is that many small regions exist in a supercooled system and relaxation might be nearly exponential in each region. However, dynamics in distinct regions are different with the relaxation time varying, resulting the stretched exponential behavior in the relaxation of the whole system [7, 55, 59].

Violation of Stokes-Einstein relation When the temperature of a liquid is high enough, the diffusion coefficient D and the viscosity η obey the Stokes-Einstein relation [62],

$$D \propto \frac{T}{\eta} . \quad (1.12)$$

With the assumption $\tau_\alpha \propto \frac{\eta}{T}$ the Stokes-Einstein relation can also be expressed as [67],

$$D\tau_\alpha \sim \text{const} . \quad (1.13)$$

If the temperature of supercooled liquids is reduced, the breakdown of Stokes-Einstein relation is observed [55, 67], which can also be attributed to the heterogeneous dynamics [55]. At low temperature, particles in some regions have larger mobility, while other particles may belong to immobile regions [64]. The diffusion is determined by mobile particles, and the structural relaxation is controlled by immobile ones. As a result, the diffusion coefficient and the relaxation time for the whole system do not follow the Stokes-Einstein relation, although in each small region it is still valid [7, 55]. With decreasing temperature, the deviation from Stokes-Einstein relation becomes larger [55]. The existence of mobile and immobile regions can be confirmed directly by the self-part of the van Hove function, which will be discussed in Chapter 3.

Dynamic length scales The dynamic heterogeneous behavior has been discussed above. Mobile and immobile regions are found in supercooled liquids. It is natural to ask: what are the typical sizes of these

regions? As temperature goes down, will these sizes increase or decrease? Can the change of length scales be related to dynamical slowing down in supercooled liquids? To answer these questions, one has to study dynamic length scales of glass-forming liquids. However, the traditional two-time correlation functions cannot give information about it. Fortunately, scientists found higher-order correlations can be used to extract dynamic length scales [7, 9].

The four-point susceptibility $\chi_4(t)$ is commonly investigated. Given an observable $o(\mathbf{r}, t)$, (which can be the local density fluctuation at position \mathbf{r} and at time t , or the excess energy, etc.), an instantaneous local two-time correlation function can be defined as [68, 69],

$$C(t) = \frac{1}{V} \int d\mathbf{r} o(\mathbf{r}, t) o(\mathbf{r}, 0) . \quad (1.14)$$

The four-point susceptibility $\chi_4(t)$ is expressed as,

$$\chi_4(t) = N(\langle C^2(t) \rangle - \langle C(t) \rangle^2) . \quad (1.15)$$

At a fixed temperature, $\chi_4(t)$ increases with time from zero to a maximum at the time around τ_α , showing the growth of dynamic heterogeneity. After that, it decays back to zero for longer time. When the temperature is lowered, the peak value in $\chi_4(t)$ continuously becomes larger, indicating the increase of dynamic length scales [7]. In chapter 4, we will investigate the four-point susceptibility and the dynamic correlation length of a system when it approaches the glass transition.

1.2.3 Glass formers

Many liquids can transform into the glassy state, if crystallization is avoided. In this subsection, two glass formers will be briefly discussed, for they are intensively investigated by experiments and simulations. Other glass formers, such as polymer, network glass formers, biomaterials, metallic glass formers [60, 70] are also very important, but will not be discussed here, for they are not closely related to our research.

Molecular glass formers Many molecular supercooled liquids can form glasses when the temperature is reduced or the pressure is increased very quickly [58]. All the dynamic behavior mentioned above, such as the dramatic increases of the relaxation time, the heterogeneous dynamics has been observed in molecular glass formers [9]. The dynamic slowing down in molecular glass formers has been observed in the time scale as long as fifteen decades via experiments. In contrast, for colloidal systems, information about the dynamic behavior can only be probed within about five decades or less [9, 71]. However, four-point susceptibility

in molecular liquids is not accessible in experiments so far, since it is difficult to measure the time-resolved dynamics in a small region with a typical size of the order of a few nanometers [7]. In contrast, $\chi_4(t)$ in some colloidal systems can be measured via experiments.

Colloids A colloid is the mixture in which small particles disperse in other substance, such as gas, liquid, and solid. Colloidal glass formers have been demonstrated to exhibit all salient features of the glass transition when the volume fraction is increased [72]. Compared with molecular and atomic glass formers, colloidal systems are much easier to probe. The size of colloids is about 100 – 1000 nm, much larger than that of molecules; thus the dynamic light scattering techniques can be exploited to investigate the dynamics during the glass transition [9, 72]. Moreover, the motion of colloids are much slower than those of molecules, and can be captured directly by many video cameras [9]. Actually, colloidal suspension is not only a good model for studying the glass transition, but also very helpful to understand the rheological properties of supercooled liquids and glasses, i.e. the so called shear thinning effect [42].

1.3 Approaches for research

1.3.1 Theories

As alluded to above, there are many unsolved issues regarding nonequilibrium states and the glass transition. A lot of theoretical approaches have been proposed in the last three decades. Here, I will only present three theories, namely, the mode-coupling theory (MCT), the kinetic constrained models (KCM), and the random first-order transition (RFOT) theory. These theories can predict the behavior of some physical quantities, such as the relaxation time, viscosity. Thus their validity can be tested by experiments [7]. I have to admit that it is almost an impossible task to give a full review on these theories. Each of them has many topics, including motivations, derivations, applications, limitations, etc. Recent reviews [7, 55, 57, 73, 74] and books [9, 53, 56, 59] give good resources for studying these theories. Here only some important predictions made by them will be introduced.

Mode-coupling theory

Mode-coupling theory (MCT) was proposed independently by Bengtzelius et al. [58] and Leutheusser [75]. Within MCT, using the static structure factor as input information [56], many dynamic properties of supercooled liquids can be obtained, such as the dynamic structure factor, the self-intermediate scattering function and the mean square displacement [7, 58]. The predictions made from the MCT have been scrutinized by both simulations and experiments [61, 76]. So far it is the only theory which can be used to calculate the

dynamic properties quantitatively for glass-forming liquids [59]. However, this theory fails if a system is too close to the glass transition [7, 53].

MCT predicts that the temperature dependence of the relaxation time [61],

$$\tau_\alpha = C(T - T_c)^{-\gamma} , \tag{1.16}$$

where C , T_c , and γ are predicted by MCT. With simulation data, these parameters are obtained by fitting the power law to the data. T_c is the mode-coupling temperature, at which the relaxation time diverges and the diffusion coefficient vanishes [61]. Usually, T_c is found to be about 20% – 30% higher than T_g . Equation 1.16 can only fit τ_α within a time scale of 2-3 decades [7]. Remember that the time window during the glass transition is typically larger than 14 decades, MCT works only in a narrow regime. Despite this limitation, MCT is still very useful in investigating the glass transition phenomenon in various systems, such as molecular supercooled liquids and colloidal suspensions. Especially, for colloids the dynamics usually lies in the millisecond regime (compared to the typical microscopic time scale for molecules which is in picosecond range); thus only the first 5 to 6 decades corresponding to the onset of glassy dynamics in colloidal suspensions can be studied by experiments. In this case, MCT plays an even more important role in examining the experimental results for colloidal systems.

Recently, MCT is also used to investigate dynamic heterogeneity of glass formers [53] Some of the predictions about the four-point correlation functions and dynamic length scales have been examined and confirmed by computer simulations [9]. Efforts have also been devoted to extending MCT to nonequilibrium systems, such as sheared liquids, where some rheological behavior was predicted [21, 72]. Exploring the applications of MCT remains an active domain of research.

Successes of MCT have been simply introduced above, now we want to discuss some limitations of MCT. First, as already mentioned, MCT can only cope with the system which is moderately supercooled [7]. Actually, thermal activation over the finite energy barriers already begins to occur at a temperature higher than T_c . Close to T_c , the long-time part of the relaxation function cannot be explained solely by MCT [53] It is conjectured by Biroli et al. [77] : when the temperature is lowered to approach T_c , the relaxation function in the short time scale can be described by MCT, while its long-time behavior is controlled by the rare activated events. When temperature is further reduced, the thermally activated behavior becomes more dominant and the mode coupling theory cannot deal with this very well [7, 53]. Moreover, the relaxation time does not diverge at T_c . The glass transition predicted by MCT is actually not a real phase transition but a crossover in the dynamics [7]. For the temperature around and below T_c , other theories are needed.

Kinetically constrained models

Kinetically constrained models (KCMs) are a class of simple models, which display rich dynamical behavior during the glass transition as a result of geometrical constraints acting at the level of kinetic rules [7, 9]. One of the most popular models is devised by Kob and Andersen twenty years ago [78]. The Kob-Andersen model (not the binary Lennard-Jones mixture which is also denoted as Kob-Andersen model) is a three dimensional lattice gas, where particles interact by hard core constraint [78, 79]. At a given time, the occupation number n_i on a lattice site i equals 1 if there is a particle in the site, and it is equals to 0 if the site is unoccupied. To move a particle to one of its nearest neighbor sites (in a 3-D lattice gas there are 6 nearest neighbor sites around it), the following three conditions must be satisfied: (i) the neighbor site is empty; (ii) the particle has fewer than m neighbors (Kob and Andersen studied the model with $m = 4$); (iii) the particle will still have few than m neighbors after it has moved to the new site [78, 79].

The kinetically constrained lattice gases are conservative KCMs [9], in which the total number of particles is constant [9, 78]. In contrast, spin-facilitated models, such as the Fredrickson-Andersen model [80], the East model [81], are non-conservative KCMs [9]. In these models, the occupation number n_i can be interpreted as up ($n_i = 1$) and down ($n_i = 0$) spins [80]. A spin can be flipped only when a local constraint (i.e. at least a minimal number of its neighbor sites are at $n_i = 0$ state) is satisfied. Compared to kinetically constrained lattice gases, $\sum_i n_i$ is not conserved in spin-facilitated models [9, 78].

Although these models have different kinetic rules, they display similar dynamics. To give a clear illustration of the dynamics in KCMs, the excitation line - bubble plot is often employed [7]. Figure 1.5 shows the typical dynamics of mobile defects for the 1-D Fredrickson-Andersen model with $k = 1$ (at least one of the nearest neighbor site is 'empty'). In kinetically constrained lattice gases, mobile defects are the clusters of empty sites. The excitation lines stand for mobile defects which can only propagate along the lines, while the bubbles show the inactivated area [7]. As illustrated in figure 1.5, a mobile defect can not occur automatically in an immobile region, it can only be created when its neighbors (at least one) are mobile. In other words, a defect can facilitate the motions of its neighbors, and eventually cause the relaxation of the whole system. At low temperature defects are sparse, while immobile regions are large. It takes longer time for defects to visit all the immobile regions. Thus the structural relaxation time of the system increases [7, 9]. Although KCMs are very simple and abstract models, they actually exhibit the physical intuition similar to that in glasses. A particle in a glass can diffuse only when mobile regions are present around it [7, 9]. It has been confirmed that KCMs display some dynamic behavior which is reported for realistic glass formers, such as the super-Arrhenius slowdown and stretched relaxation, dynamic heterogeneity, aging effects, etc. [9]. Moreover, ergodicity breaking transition is observed in the KA lattice gas [73].

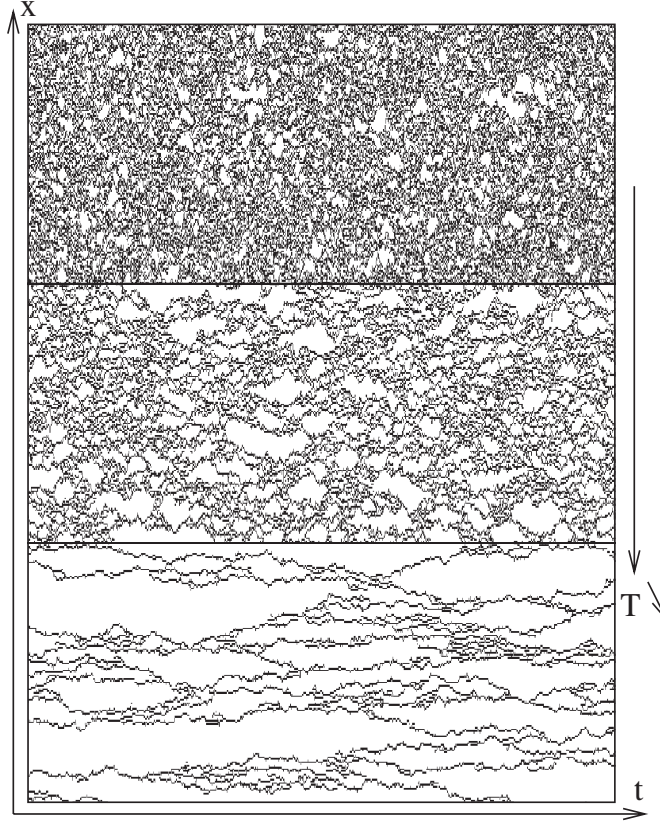


Figure 1.5: Excitation line - bubble plot for the 1-D Fredrickson-Andersen model with $k = 1$ (at least one of the nearest neighbor site is ‘empty’). Black lines stand for mobile cells, and white bubbles show immobile regions. Temperature in the top panel is the highest, at which the dynamics is homogeneous. The bottom panel show that the dynamics is heterogeneous at low temperature. Figure is adapted from reference [7].

A major success of KCMs is its ability to account for dynamic heterogeneity during the glass transition [7, 9]. They are actually natural consequences of the cooperative motions in KCMs [9]. The four-point susceptibilities $\chi_4(t)$ have been calculated for many kinetically constrained models, and the results are in good agreement with those obtained for realistic supercooled liquids. $\chi_4(t)$ at a fixed temperature has non-monotonic evolution with time. On small time scales, $\chi_4(t)$ increases with time and reach a maximum at time t^* (t^* is close to τ_α). After that $\chi_4(t)$ decreases. The height of the peak increases with reducing temperature [7, 9]. The dynamic correlation length in KCMs is found to increase with t when time is smaller or around τ_α . When temperature is lowered to a critical point (this critical temperature is dependent on models), both relaxation time scales and dynamic length scales increase to infinity [7]. Furthermore, KCMs give predictions for the relation between dynamic length scales and time scales [7, 9].

As we have mentioned before, the violation of the Stokes-Einstein relation is a consequence of dynamic heterogeneity [55]. KCMs successfully explain the breakdown of the Stokes-Einstein relation [82]. As illustrated in figure 1.5, at high temperature mobile regions are very large, the persistence time t_p (which means

the waiting time for a tracer to move for the first time, given an arbitrary initial time for observation) is comparable with the exchange time t_x (which counts the time between moves). As temperature is reduced, the bubbles take major part, t_p becomes much longer than t_x . The relaxation time τ_α is approximately equal to t_p , while the diffusion time is related to the exchange time by $D \sim t_x^{-1}$. As a result, $D\tau_\alpha$ is not constant at low temperature, the Stokes-Einstein relation is violated [7, 9].

Above discussion indicates that kinetically constrained models are very useful in investigating the dynamic behavior of glass formers. In contrast, the thermodynamic properties of supercooled liquids are not considered by KCMs at all. This may be the main limitation of KCMs. However, it is still on debate: whether the thermodynamics is relevant or not to the glass transition [9]. The second issue is about a fundamental assumption for KCMs: it is still not explained why there are only very few mobile regions which can occur automatically, and why the number of such regions becomes smaller when temperature goes down [7]. Another small limitation of KCMs is that the dynamics within very short time scales ($t \ll \tau_\alpha$) cannot be explained [9].

Random First-Order Transition Theory

The random first-order transition theory (RFOT) was first introduced by Kirkpatrick, Thirumalai and Wolynes in the late 80s [83, 84]. The name is generalized from the ordinary first-order transition to crystalline state, with assumption that the glass transition involves a set of aperiodic structures instead of periodic orders in crystals [57]. Simply speaking, RFOT assumes there are many ‘cavities’ in supercooled liquids. The size of these cavities is l^* . The region inside a cavity are ideal glass, where ergodicity cannot be restored and the dynamic correlation functions cannot relax to zero even after a very long time [9, 53]. On the other hand, the regions outside cavities are liquid, there are exponentially large number of configurations can be explored, the dynamic structure factor can decay to zero [9, 53]. Due to the thermal fluctuations, the relaxation of cavities can happen through the cooperative rearrangements [9, 55]. The relaxation time for the whole system is then equal to that of a cavity with size l^* [53]. A crucial assumption for RFOT is that the value of l^* is only determined by the thermodynamics [9, 53]. This is in sharp contrast to kinetically constrained models discussed previously, where the thermodynamic aspects are totally missing.

So far, RFOT has been used to explain various phenomena for many different systems, such as the dynamic behavior in supercooled liquids, quantum effects in glasses (with temperature below 1 K), and rheological behavior nonequilibrium systems [53, 57]. One advantage of RFOT is that the thermodynamic properties of a system, such as the configurational entropy and the specific heat are considered and related to dynamics [53]. For instance, RFOT asserts that the dramatic slowing down of the relaxation is caused by the reduction of configurational entropy [53]. Moreover, RFOT confirms the equality between T_k and T_0 ,

implying that the thermodynamics and the dynamics of supercooled liquids can indeed be related [7]. RFOT also predicts dynamic heterogeneity in glass formers [53], and suggests that the dynamic correlation length grows as the temperature is reduced [57]. In addition to those successes in dealing with supercooled systems, RFOT is also used to explain the shear thinning phenomenon, where the energy barriers are lowered due to shear, and the flow of the liquid is accelerated [53].

Despite many successful predictions that RFOT can yield, there are still some issues. First, a lot of uncontrolled assumptions for RFOT limit its applications [7]. Compared to MCT, RFOT can work in a broad temperature range. Moreover, it is demonstrated that RFOT is effectively equivalent to MCT around the dynamical crossover [57]. However the MCT/RFOT crossover is still not clear and needs to be understood [77]. The third issue is that the dynamic correlation length ξ , which is larger than the size of cavity l^* , cannot be calculated from RFOT directly [77]. It is easy to understand that within a cavity ($R < l^*$), particles move cooperatively, but it is not clear how the collective motions extends outside the cavity to a larger length scale ξ . [9].

1.3.2 Experiments

During the last two decades, experimental techniques have been developed, so that the dynamic behavior of glass-forming liquids can be investigated more precisely. We will briefly introduce two important experiments: dynamic light scattering and confocal microscopy. Both methods are very powerful in exploring the dynamics of the glass transition, specifically, dynamic heterogeneity. The emphasis will be laid on the features and applications of these experiments. The details of the techniques (i.e. how to set up the apparatus) will not be discussed.

Dynamic light scattering

As we know, the structure of a sample can be probed by static light scattering [85]. The static structure factor $S(q)$ can be calculated from the intensity of scattered component [62]. However, the dynamic behavior of the system cannot be obtained from static light scattering. This task can be accomplished by a dynamic light scattering experiment, which probes the temporal fluctuations of the scattered intensity of light [9, 85]. Given the scattering angle θ and the wavelength of incident light λ , the scattering wave vector can be determined as $q = (4\pi/\lambda)\sin(\theta/2)$ [9, 85]. The length scale on which the dynamical properties can be measured is $\sim 2\pi/q$ [71].

DLS is a very useful technique to study glassy colloidal suspensions, because collective motions of the particles can be probed [9]. From DLS, the intermediate scattering function can be obtained directly by nor-

malizing the intensity autocorrelation function. Furthermore other dynamic quantities, such as mean-squared displacement, velocity autocorrelation function, and the non-Gaussian parameters can be calculated [86]. In addition, DLS is also exploited to study the violation of the Einstein relation and the notion of effective temperature in the nonequilibrium system [4, 87].

There are several advantages for the dynamic light scattering experiment. First, many particles can be probed at the same time, generating good statistics for the averages. Secondly, the samples probed by DLS usually contain smaller particles than those in the optical microscopy measurements. Thus the gravitational effects are less important, and the typical time scales for DLS are smaller than other techniques, providing more details about the dynamics [9].

Some disadvantages also exist for conventional DLS technique. First, a very important event in the DLS is the single scattering, from which the dynamic properties can be generated. However, for the intensively turbid samples multiple scattering is dominant, preventing one from obtaining useful information about the sample [9, 85]. This limitation was overcome by some techniques, such as the two-color light scattering, diffusing wave spectroscopy, etc. [9, 88]. The second shortcoming is that the local events cannot be detected via conventional DLS, because the average is taken over a large ensemble and time [9, 85]. To solve this issue, new techniques have been designed recently. One of them is the photon correlation imaging [9, 89]. With this novel method, dynamic heterogeneity can be tested [9, 89].

Confocal microscopy

Conventional optical microscopy was widely used to study a sample in real space and real time. Information about the structure and mechanism on a length scale ranging from $0.5 \mu\text{m}$ to $1.5 \mu\text{m}$ can be obtained [9]. Thus it is very useful for investigating biological systems and colloidal suspensions [85]. However, when the samples are highly concentrated, conventional optical microscopy cannot work well, because the light is multiply scattered by the particles in the system, making the image blurry [9, 85].

To overcome the shortcoming in conventional optical microscopy, a screen with a pinhole aperture is set up in front of the detector [85]. Only the light from the focal point can pass through the pinhole and be captured by the detector; while the out-of-focus light is rejected [7]. With this improvement, the particles can be seen with higher definition. Given each single image is taken for the $x - y$ plane, then the 3-D information can be achieved if one takes many pictures at different heights along z direction [9]. The confocal microscopy experiment is a very powerful tool to study supercooled colloidal systems. At room temperature, a colloidal particle with the diameter $\sigma = 1 \mu\text{m}$ diffuses in water with a velocity around $1 \mu\text{m}/\text{s}$ [9]. With confocal microscopy technique, 2-D images can be taken every 10 ms to several seconds, and 3-D images need longer time, about 2 to 20 seconds [9]. In this case, the motion of colloidal particles can

be tracked in a confocal microscopy experiment, since the displacement of the particle during the scanning time is comparable with the interparticle distance [9]. The trajectories of particles can be captured and stored in computers, the dynamic correlations, such as the mean square displacement, van Hove functions, and so on, can be calculated with these configurations [18, 85].

1.3.3 Simulations

To investigate the glass transition and nonequilibrium systems, in addition to theories and experiments, numerical simulations are intensively employed too. Thanks to the rapid development of computer hardware, the operational speed and the storage capacity are both largely improved. Moreover, many new codes and software have also been developed. All these achievements make one able to study larger systems containing several thousands particles, with lower temperatures or higher concentrations. In other words, a system which closely approaches the glass transition can be explored [56]. In this subsection, computer simulations will be discussed with four aspects. First of all, we will address the fundamental question: why are computer simulations necessary? Then several models and methods will be described. Finally, we will focus on the limitations of simulations and how to improve their performance.

Why simulations?

To answer this question, let us recall a typical procedure of doing research. Scientists design many experiments in the laboratory, record the data, and propose some theories to explain the results. For the systems containing large numbers of particles (i.e. atoms, molecules, colloids, etc.), statistical mechanics is usually used to do the theoretical analysis. However, in many cases the solutions are hard to obtain analytically [90]. Fortunately, with the help of computers, researchers can make models to mimic systems in the lab, and study these models via numerical simulations. For instance, as in the case of supercooled liquids, many dynamic quantities can be calculated with the saved trajectories generated from the simulations. One can compare these results with the measurements achieved by experiments and assess the models. On the other hand, theoretical analysis can be performed on these models, predicting the dynamic behavior, and the comparison between the theory predictions and the simulated results can be made. In a word, computer simulations plays an important role in connecting the theories and experiments [90].

The necessity of simulations can also be confirmed if one recognizes the limitations of the experiments. Research involving very small length scales and long time scales cannot be performed experimentally so far, or at least one cannot get accurate enough measurements by experiments. For example, the four-point susceptibilities and dynamic length scales for the molecular glasses cannot be generated from experiments,

but can be calculated numerically by the simulations [7]. Besides, to form a glass, the supercooled liquid needs to be quenched suddenly to avoid crystallization. Compared to experiments, the cooling rate in a simulation can be selected and fixed more easily. Moreover, it has also been shown that the experiments are not convenient to investigate the effective temperatures for the nonequilibrium systems [4, 13, 47]. For instance, Berthier et al. argued that the dynamic correlation function and response function cannot be measured simultaneously [13], while they can be calculated from the unperturbed trajectories at the same time by the simulations [91]. Computer simulations also have other advantages. Various models with different interparticle potentials can be tested precisely. The parameters, such as the temperature, volume fraction etc. can be controlled easily [9].

Models

To simulate the sample numerically, it is important to know the forces exerted on the structureless particles, which can be calculated from the potential,

$$V = \sum_i V_1(\mathbf{r}_i) + \sum_i \sum_{j>i} V_2(\mathbf{r}_i, \mathbf{r}_j) + \sum_i \sum_{j>i} \sum_{k>j>i} V_3(\mathbf{r}_i, \mathbf{r}_j, \mathbf{r}_k) + \dots \quad (1.17)$$

In the equation, r_i is the position of particle center. The first term $\sum_i V_1(\mathbf{r}_i)$ on the right side represents the external potential imposed on the system. The second term gives the pairwise interactions between the particles. The third component shows the interparticle potential involving three particles [90]. The potentials between four and more particles are usually very small and can be neglected. Although the triplet-molecule contribution is important and needs to be considered, the calculation is time-consuming [90]. To improve the efficiency of simulations, the ‘effective’ pair potential V_2^{eff} is defined which includes part of V_3 [90], and the total potential can be written as,

$$V \approx \sum_i V_1(\mathbf{r}_i) + \sum_i \sum_{j>i} V_2^{\text{eff}}(r_{ij}) \quad (1.18)$$

We will briefly introduce three models for the pair interparticle potential which were used for the simulations in our research.

Hard sphere model The hard sphere potential is a very simple ideal model to mimic the interaction between particles [90],

$$V^{\text{HS}}(r) = \begin{cases} \infty & (r < \sigma) \\ 0 & (r \geq \sigma) \end{cases} \quad (1.19)$$

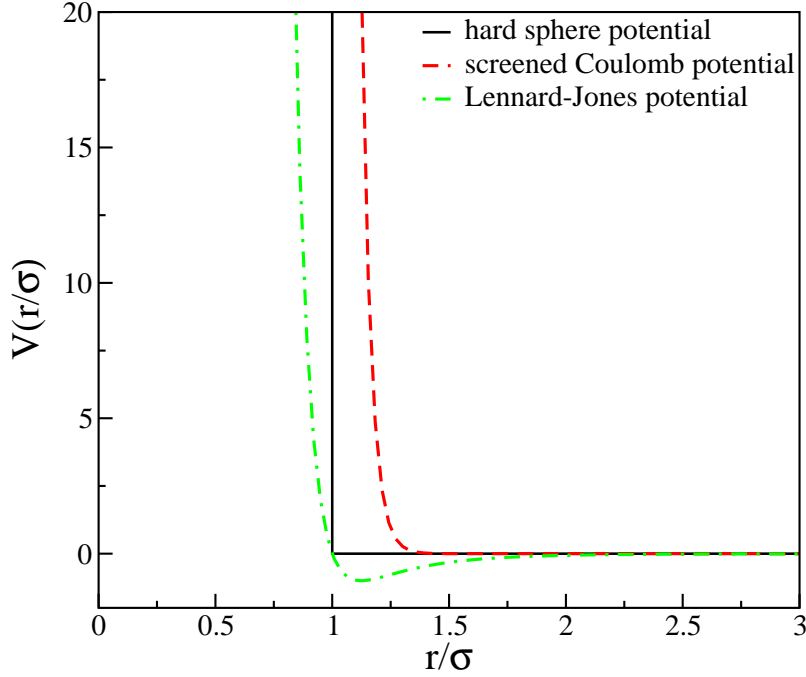


Figure 1.6: A schematic figure showing different potentials. For the screened Coulomb potential, the parameters are $A = 475k_B T$ with $k_B = 1.0$ and $T = 1.0$, $\kappa\sigma = 24$. The meaning of these parameters are described in the text. For the Lennard-Jones potential $\epsilon = 1.0$, see the text for details.

In this model, the attractive interactions between the particles are omitted. It is because even for the dense phases of matter, the structures of the systems are still determined by the repulsive forces between the particles [90]. This simplification makes the hard spheres be very useful as a theoretical model, and it is very easy to implement this model in computer simulations [90]. The glass transition of hard-sphere colloidal suspensions have been investigated intensively [9, 56]. The only control parameter is the volume fraction [9]. The hard-sphere colloidal system will undergo the glass transition if the volume fraction is increased.

Screened Coulomb model In chapter 2, we will use a screened Coulomb potential with parameters first introduced by Rastogi et al. [16],

$$V(r) = A \frac{\exp[-\kappa(r - \sigma)]}{r}. \quad (1.20)$$

In this equation, $A = 475k_B T\sigma$ measures the potential strength, κ is the inverse Debye length with $\kappa\sigma = 24$, r is the position of the particle, and σ is the diameter. The model with these parameters represents the realistic sample which contains 100 nm spherical colloids with 4790 surface charges suspended in a solvent. The solvent is a 1.1 mM solution of a 1 : 1 electrolyte [16].

Kob-Anderson Model To study the properties of supercooled liquids, Kob and Anderson [63] proposed a model which is a binary mixture (80 : 20) of Lennard-Jones particles. The pairwise potential has the form,

$$V_{\mu\nu} = 4\epsilon_{\mu\nu}[(\sigma_{\mu\nu}/r)^{12} - (\sigma_{\mu\nu}/r)^6]. \quad (1.21)$$

The parameters in the above equation are $\sigma_{AA} = 1.0$, $\sigma_{BB} = 0.88$, $\sigma_{AB} = 0.8$, $\epsilon_{AA} = 1.0$, $\epsilon_{BB} = 0.5$, and $\epsilon_{AB} = 1.5$. This potential is similar to the one proposed by Weber and Stillinger which describes the amorphous $\text{Ni}_{80}\text{P}_{20}$ [92]. In the last fifteen years, the Kob-Anderson Model have been intensively employed to study the glass transition of supercooled liquids [93].

Simulation methods

Since early 1950s computers have been used to perform numerical simulations in various fields, helping understand many issues in physics, chemistry and biology [90, 94]. Many methods have been proposed to deal with different systems, efforts were also devoted to developing new algorithms to improve the performance. Regarding the simulation methods, many issues can be discussed. For instance, which ensemble is chosen for a simulation? How to set up the thermostat if necessary? How to cope with the boundaries? How to calculate the thermodynamic and dynamic quantities from a simulation? The instructive answers for these questions can be found from many textbooks, two very classic books among them are references [90] and [94]. Here we will briefly give sketches of three methods which are intensively employed to investigate the glass transition and supercooled liquids.

Molecular dynamics simulation Among the three methods, molecular dynamics (MD) simulation is very similar to a realistic experiment [94]. Consider a sample which contains N particles, the motion of them can be described by the Newton's Equations. By solving these equations, the trajectories and velocities of the particles can be obtained in the configuration space [90, 94, 95]. To start a simulation, one need initialize the system by randomly generating the positions and velocities of particles. In practice, it is necessary to use auxiliary algorithms to set up the initial condition and to make sure that the particles do not overlap each other and that no overflow errors happen. The interaction forces can be calculated with the chosen model (i.e. Lennard-Jones potential), the particles then have small displacement due to the forces exerted on them. The positions and velocities are updated. With these new positions, the interparticle forces are calculated again. Following this loop, the trajectories of particles can be generated [94]. After the system is equilibrated, many physical quantities about the thermodynamics, static structure, and dynamics of the system can be calculated from the trajectories and velocities of the particles.

A general procedure of a MD simulation is briefly introduced above. Two more points need to be mentioned here. First, the most time-consuming part during simulation is to solve the Newton's equation of motion. The time step δt cannot be arbitrarily large. To select a proper time step, three factors (maybe more) need to be considered. First, δt should be short enough so that the displacement of the particle during the time is smaller than the size of the particle [90]. Second, the steeper the potential is, the shorter δt should be. Third, different algorithms may need different time steps [96]. To make sure that the calculated quantities have good statistics, the total time of simulation should be at least hundreds times of the relaxation time. This is extremely difficult for supercooled liquids, because the relaxation time grows rapidly as the system approaches the glass transition [95]. Thus an efficient algorithm is demanded. The Verlet algorithm is commonly used, because it has many advantages, including small memory requirement, satisfying time-reversible, energy conservation, and simplicity for implementing [90]. The second point we want to mention is that different ensembles, in addition to the microcanonical one (constant NVE) [94], may need to be considered. However, to use some ensembles, such as NVT, NPT, one of the difficulties is that the temperature and pressure have to be constant. To fix the temperature during a simulation, Andersen thermostat or Nosé-Hoover thermostat is usually connected to the sample [94]. To keep the pressure constant, the size and even shape of the simulation box have to be varied [90].

Monte Carlo simulation Monte Carlo method was introduced by von Neumann, Ulam, and Metropolis in the 1940s [97, 98]. The basic idea is that the mathematical calculations can be regarded as the stochastic problem, which can be solve by repeating random sampling [90]. The Monte Carlo simulation has been widely used in physics, chemistry, and biology to simulate the many body systems, including liquids, disordered condensed matters, and solids [99].

Now let us consider a typical procedure for simulating a liquid with the Metropolis algorithm which improves the effectiveness of the Monte Carlo method. Given a system containing N particles, their initial positions are generated with considering some initial distribution. A particle i is selected at random, its energy E_i is calculated. Then let the particle move with a random distance in a cubic box (for 3-D case), calculate the energy E'_i with the new position. Decide if this move is accepted or not by calculating the probability [94],

$$\text{acc}(o \rightarrow n) = \min(1, \exp\{-\beta[E'_i - E_i]\}) , \quad (1.22)$$

where β is inverse of the temperature. In every Monte Carlo step, there are N attempts to make such displacement for a randomly selected particle [93].

Brownian dynamics simulation For colloids and polymers, the microscopic dynamics is close to Brownian behavior [95]. What is more, for a colloidal system, the molecular dynamics simulations are time-consuming and unnecessary, since the details about the motions of the larger numbers of solvent molecules are not important. In this case, the Brownian dynamics simulation can be exploited, in which only the motion of colloidal particles are considered, the total effects of the solvent molecules on the colloids are represented by a friction term and the random noise [90]. The motion of the particles are described by the Langevin equation.

Compared with the molecular dynamics simulation, the Brownian dynamics method has several features. First, there is no momentum in the equation of motion, only positions are updated during the simulation. Second, within a short time the dynamic quantities calculated from the BD simulation are different from those generated by MD. For example, the mean square displacement calculated by MD shows that particles move ballistically at very short time, while from the BD simulation, the short time part in MSD exhibits diffusive behavior. For long time, the dynamic behavior is not affected by the simulation method [9, 95].

Disadvantages of simulations

To do research with computer simulations, one first needs to choose a good model to mimic a realistic system. This is actually not easy, since each system has specific microscopic characteristics, and it is very hard to include all those important features in a simple model. Even if one has already found a ‘perfect’ model, there are still limitations for simulations, which mainly originate from two aspects. First, the size of the sample cannot be arbitrarily large, it can contain at best several thousands particles [56], while for many types of supercooled liquids, including colloidal suspensions, molecules, and polymers, finite-size effects have been observed during the glass transition [9], which is hard to prevent in the simulation. Experiments, on the other hand, can get better results because a realistic sample usually contains a large number of particles. The second difficulty for the simulation is the time. So far, the simulations are limited to a temperature window, in which the relaxation time increases by about 10^5 times. However, as we have mentioned at the very beginning, during the glass transition, the relaxation time increases from $\sim 10^{-2}$ s to $\sim 10^{12}$ s, over 14 decades. This time issue limits the ability of computer simulations to search the glass transition point T_g .

Improve the performance of simulations

Above, we discussed the two main disadvantages of simulations. To improve the performance, those two points need to be considered. To shorten the simulation time, several ways can be tried. First, one can choose a simpler model. However, a simple model may cause less accuracy. Secondly, a better algorithm is always needed. For example, for the Brownian dynamics simulation, the second-order algorithm has higher

efficiency than the first-order one. In the equation of motion, the step is a combination of two first-order steps [100] (the details will be discussed in chapter 2). Thirdly, many programs have been developed recently (i.e. Lammmps [101]), and they have quite good performance. Fourth, one can also try parallel programming, which is also contained in some programs, such as Lammmps. For example, if we need to simulate a large system to a long time, the system can be divided into several parts. Each part is calculated on a slave processor, and the results are sent back to the master processor, which then assigns new tasks to the slaves. In this case, the simulation time is shorter than the one with single processor.

1.4 Organization of the dissertation

In chapter 2, we study a monodisperse colloidal suspension, in which the particles interact with each other via the pairwise additive, repulsive screened Coulomb potential [16]. We apply moderate and high shear on the system, and find the strong anisotropy in the liquid. Four different effective temperatures are defined and calculated for the system with various shear rates. The first definition is based on the modified Einstein relation. The second effective temperature is calculated from the generalized fluctuation-dissipation theorem. We obtain the third one by using the linear response function. The last one is evaluated from the density distribution function out of the linear-response regime. The effective temperatures measured from the first, second, and fourth methods are in consistent with one another, but the third definition gives different results.

In chapter 3, we investigate the Kob-Andersen model (binary Lennard-Jones mixture) at different temperatures ($T \leq 0.6$), ranging from the supercooled regime to the glassy state. By imposing the systems with a small shear, the ergodicity is restored when temperature is below the glass transition point. All the system behave as supercooled liquids. Both the static and dynamic quantities of the systems are calculated. As expected, the static properties hardly change, while the dynamic behavior strongly depends on the temperature and shear. Specifically, the cage effect is observed from the mean square displacement. The diffusion coefficient goes down with the temperature, but is not vanish even at the lowest T due to shear. The dynamic slowing down is evident from the self-intermediate scattering function. However, all the time correlation functions decay to zero eventually, aging is stopped because of shear. The α -relaxation time increases relatively slow when the temperature is lowered, but it does not diverge even at $T = 0.0$. The reason is again shear! Dynamic heterogeneity are suggested by the violation of the Stokes-Einstein relation and the exponential tails in the self-part of the van Hove function.

The motivation for chapter 4 is to research dynamic length scales and time scales, as well as their dependence on the choice of the ‘measuring stick’ a . First of all, the average overlap function (which is

similar to the self-intermediate scattering function) is calculated with different parameter a . It is found that the parameter plays a similar role as the wave vector did for the inter-mediate scattering function, but with an opposite way. The relaxation time increased with a , and for different volume fraction, the a -dependence tends to fall onto a master equation. The four-point susceptibility χ_4 is calculated. The dynamic correlation length is evaluated from the Ornstein-Zernike fits for the four-point structure factor $S_4(q, t)$. Four-point pair correlation function is calculated and analyzed with the envelope fits.

Bibliography

- [1] L. F. Cugliandolo, J. Kurchan, and L. Peliti, *Phys. Rev. E* 55, 3898 (1997).
- [2] J. Kurchan, *Nature* 433, 222 (2005).
- [3] L. Berthier and J.-L. Barrat, *Phys. Rev. Lett.* 89, 095702 (2002).
- [4] B. Abou and F. Gallet, *Phys. Rev. Lett.* 93, 160603 (2004).
- [5] L. Berthier, J.-L. Barrat, and J. Kurchan, *Phys. Rev. E* 61, 5464 (2000).
- [6] N. Pottier and A. Mauger, *Physica. A* 332, 15 (2004).
- [7] L. Berthier and G. Biroli, *Rev. Mod. Phys.* 83, 587 (2011).
- [8] J.-L. Barrat and L. Berthier, *Phys. Rev. E* 63, 012503 (2000).
- [9] L. Berthier, G. Biroli, J.-P. Bouchaud, L. Cipelletti, and W. Van Saarloos, *Dynamical Heterogeneities in Glasses, Colloids and Granular Media* (Oxford University Press, New York, 2011).
- [10] C. Monthus and J.-P. Bouchaud, *J. Phys. A: Math. Gen.* 29, 3847 (1996).
- [11] S. F. Swallen, K. L. Kearns, M. K. Mapes, Y. S. Kim, R. J. McMahon, M.D. Ediger, T. Wu, L. Yu, and S. Satija, *Science* 315, 353 (2007).
- [12] F. Varnik, *J. Chem. Phys.* 125, 164514 (2006).
- [13] L. Berthier and J.-L. Brarat, *J. Chem. Phys.* 116, 6228 (2002).
- [14] S.-i. Sasa and H. Tasaki, *J. Stat. Phys.* 125, 125 (2006).
- [15] *Shear rate*, Wikipedia.com, http://en.wikipedia.org/wiki/Shear_rate (Feb 07, 2013).
- [16] S. R. Rastogi, N. J. Wagner, and S. R. Lustig, *J. Chem. Phys.* 104, 9234 (1996).
- [17] R. Lahiri and S. Ramaswamy, *Phys. Rev. Lett.* 73, 1043 (1994).
- [18] C. Eisenmann, C. Kim, J. Mattsson, and D. A. Weitz, *Phys. Rev. Lett.* 104, 035502 (2010).
- [19] T. G. Mason and D. A. Weitz, *Phys. Rev. Lett.* 75, 2770 (1995).
- [20] G. Petekidis, A. Moussaïd, and P. N. Pusey *Phys. Rev. E* 66, 051402 (2002).
- [21] M. Fuchs, *Adv. Polym. Sci.* 236, 55 (2010).

- [22] F. Varnik, *AIP Conf. Proc.* 982, 160 (2008).
- [23] S. Hess and H. J. M. Hanley, *Phys. Rev. A* 25, 1801 (1982).
- [24] S. Hess and H. J. M. Hanley, *Phys. Lett.* 98A, 35 (1983).
- [25] H. J. M. Hanley, J. C. Rainwater, and S. Hess, *Phys. Rev. A* 36, 1795 (1987).
- [26] T. Weider, U. Stottut, W. Loose and S. Hess, *Phys. A* 174, 1 (1991).
- [27] S. Hess and W. Loose, *Ber. Bunsenges. Phys. Chem.* 94, 216 (1990).
- [28] S. Hess, *International Journal of Thermophysics*, 23, 905 (2002).
- [29] A. Furukawa, K. Kim, S. Saito, and H. Tanaka, *Phys. Rev. Lett.* 102, 016001 (2009).
- [30] M. Fuchs and M. E. Cates, *Phys. Rev. Lett.* 89, 248304 (2002).
- [31] J.-F. Berret and Y. Séréro, *Phys. Rev. Lett.* 87, 048303 (2001).
- [32] M. Sellitto and J. Kurchan, *Phys. Rev. Lett.* 95, 236001 (2005).
- [33] *Shear thinning*, Wikipedia.com, http://en.wikipedia.org/wiki/Shear_thinning (Feb 07, 2013).
- [34] J. R. Melrose, J. H. van Vliet, and R. C. Ball, *Phys. Rev. Lett.* 77, 4660 (1996).
- [35] A.V. Shenoy, *Colloid Polym. Sci.* 262, 319 (1984).
- [36] S. Lerouge and J.-F. Berret, *Adv. Polym. Sci.* 230, 1 (2010).
- [37] P. D. Olmsted, *Rheol. Acta.* 47, 283 (2008).
- [38] M. E. Cates and S. M. Fielding, *Advances in Physics*, 55, 799 (2006).
- [39] A. Nicolas and A. Morozov, *Phys. Rev. Lett.* 108, 088302, (2012).
- [40] S. Manneville, *Rheol. Acta.* 47, 301 (2008).
- [41] M. E. Helgeson, L. Porcar, C. Lopez-Barron, and N. J. Wagner, *Phys. Rev. Lett.* 105, 084501 (2011).
- [42] P. Schall and M. van Hecke, *Annu. Rev. Fluid Mech.* 42, 6 (2010).
- [43] H. H. Rugh *Phys. Rev. Lett.* 78, 772 (1997).
- [44] T. S. Grigera and N. E. Israeloff, *Phys. Rev. Lett.* 83, 5038 (1999).
- [45] K. Hayashi and M. Takano, *Phys. Rev. E* 76, 050104(R) (2007).

- [46] I. K. Ono, C. S. O'Hern, D. J. Durian, S. A. Langer, A. J. Liu, and S. R. Nagel, *Phys. Rev. Lett.* **89**, 095703 (2002).
- [47] H. A. Makse and J. Kurchan, *Nature (London)* **415**, 614 (2002).
- [48] G. Szamel, *Phys. Rev. Lett.* **93**, 178301 (2004).
- [49] C. S. O'Hern, A. J. Liu, and S. R. Nagel, *Phys. Rev. Lett.* **93**, 165702 (2004).
- [50] T. Lu, J. Hasty, and P. G. Wolynes, *Biophys. J.* **91**, 84 (2006).
- [51] P. ILG and J.-L. Barrat, *EPL*, **79**, 26001 (2007).
- [52] P. W. Anderson, *Science* **267**, 1615 (1995).
- [53] P. G. Wolynes and V. Lubchenko, *Structural Glasses and Supercooled Liquids: Theory, Experiment, and Applications*, Published by John Wiley & Sons, Inc., New Jersey (2012).
- [54] R. Besseling, E. R. Weeks, A. B. Schofield, and W. C. K. Poon *Phys. Rev. Lett* **99**, 028301 (2007)
- [55] A. Cavagna, *Phys. Rep.* **476**, 51 (2009).
- [56] W. Götze, *Complex Dynamics of Glass-Forming Liquids: A Mode-Coupling Theory*, Oxford University Press, New York (2009).
- [57] V. Lubchenko and P. G. Wolynes, *Annu. Rev. Phys. Chem.* **58**, 235 (2007).
- [58] U. Bengtzelius, W. Götze, and A. Sjölander, *J. Phys. C: Solid State Phys.* **17**, 5915 (1984).
- [59] K. Binder and W. Kob, *Glassy Materials and Disordered Solids: An Introduction to Their Statistical Mechanics*, World Scientific Publishing, Singapore (2005).
- [60] A. Ottochian, C. De Michele, and D. Leporini, *J. Chem. Phys.* **131**, 224517 (2009).
- [61] W. Kob and H. C. Andersen, *Phys. Rev. E* **52**, 4134 (1995).
- [62] J. -P Hansen and I. R. McDonald, *Theory of Simple Liquids (2nd edition)*.
- [63] W. Kob and H. C. Andersen, *Phys. Rev. E* **51**, 4626 (1995).
- [64] M. D. Ediger, *Annu. Rev. Phys. Chem.* **51**, 99 (2000).
- [65] L. Berthier, *Phys. Rev. E* **69**, 020201(R) (2004).
- [66] D. Chandler, J. P. Garrahan, R. L. Jack, L. Maibaum, and A. C. Pan, *Phys. Rev. E* **74**, 051501 (2006).

- [67] G. Tarjus and D. Kivelson, *J. Chem. Phys.* *103*, 3071 (1995).
- [68] L. Berthier, G. Biroli, J. -P. Bouchaud, W. Kob, K. Miyazaki, and D. R. Reichman, *J. Chem. Phys.* *126*, 184503 (2007).
- [69] L. Berthier, G. Biroli, J. -P. Bouchaud, W. Kob, K. Miyazaki, and D. R. Reichman, *J. Chem. Phys.* *126*, 184504 (2007).
- [70] J. Schroers, *ADVANCED MATERIALS* *22*, 1566 (2010).
- [71] D. EI Marsri, G. Brambilla, M. Pierno, G. Petekidis, A. B. Schofield, L. Berthier, and L. Cipelletti, *J. Stat. Mech.* P07015 (2009).
- [72] M. Fuchs and M. E. Cates, *J. Rheol.* *53*, 957 (2009).
- [73] F. Ritort and P. Sollich, *Adv. Phys.* *52*, 219 (2003).
- [74] D. Chandler and J. P. Garrahan, *Annu. Rev. Phys. Chem.* *61*, 191 (2010).
- [75] E. Leutheusser, *Phys. Rev. A* *29*, 2765 (1984).
- [76] L. Berthier and G. Tarjus, *Phys. Rev. E* *82*, 031502 (2010).
- [77] G. Biroli and J.-P. Bouchaud, *arXiv:0912.2542v1* (2009); P. G. Wolynes and V. Lubchenko, *Structural Glasses and Supercooled Liquids: Theory, Experiment, and Applications*, Published by John Wiley & Sons, Inc., New Jersey (2012). Chapter 2
- [78] W. Kob and H. C. Andersen, *Phys. Rev. E* *48*, 4364 (1993).
- [79] S. Franz, R. Mulet, and G. Parisi, *Phys. Rev. E*, *65*, 021506 (2002).
- [80] G. H. Fredrickson and H. C. Andersen, *Phys. Rev. Lett.* *53*, 1244 (1984).
- [81] J. Jäckle and S. Eisinger, *Z. Phys. B: Condens. Matter* *84*, 115 (1991).
- [82] Y. Jung, J. P. Garrahan, and D. Chandler, *J. Chem. Phys.* *123*, 084509 (2005).
- [83] T. R. Kirkpatrick and D. Thirumalai, *Phys. Rev. Lett.* *58*, 2091 (1987).
- [84] T. R. Kirkpatrick and P. G. Wolynes, *Phys. Rev. A* *37*, 3072 (1987).
- [85] V. Prasad, D. Semwogerere and E. R Weeks, *J. Phys.: Condens. Matter* *19*, 113102 (2007).
- [86] W. van Megen, *Phys. Rev. E* *76*, 061401 (2007).

- [87] L. F. Cugliandolo, *J. Phys. A: Math. Theor.* *44*, 483001 (2011).
- [88] P. N. Pusey, *Curr. Opin. Colloid Interf. Sci.* *4*, 177 (1999).
- [89] A. Duri, D. A. Sessoms, V. Trappe, and L. Cipellett, *Phys. Rev. Lett.* *102*, 085702 (2009).
- [90] M. P. Allen and D. J. Tildesley, *Computer Simulation of Liquids* (Oxford University Press, New York, 1987).
- [91] L. Berthier, *Phys. Rev. Lett.* *98*, 220601 (2007).
- [92] T. A. Weber and F. H. Stillinger, *Phys. Rev. B* *31*, 1954 (1985).
- [93] L. Berthier and W. Kob, *J. Phys.: Condens. Matter* *19*, 205130 (2007).
- [94] D. Frenkel and B. Smit, *Understanding Molecular Simulation - From Algorithms to Applications* (2nd Edition), Academic Press, New York (2002).
- [95] W. Kob, *arXiv:cond-mat/0212344v1* (2002).
- [96] Wei Cai, 2007, *An Overview of Molecular Simulation*, <http://micro.stanford.edu/~caiwei/me346/Notes/me346-handout-01-08.pdf> (Feb 07, 2013).
- [97] S. Ulam, R. D. Richtmyer, and J. von Neumann, *Statistical Methods in Neutron Diffusion*. Los Alamos Scientific Laboratory report LAMS-551, April 9, 1947.
- [98] N. Metropolis and S. Ulam, *The Monte Carlo method*. *Journal of the American Statistical Association* *44*, 335 (1949).
- [99] *Monte Carlo method*, Wikipedia.com, http://en.wikipedia.org/wiki/Monte_Carlo_simulation (Feb 07, 2013).
- [100] A. Iniesta and J. G. de la Torre, *J. Chem. Phys.* *92*, 2015 (1990).
- [101] *LAMMPS Molecular Dynamics Simulator*, lammmps.sandia.gov, <http://lammmps.sandia.gov/>(March 13, 2013).

Chapter 2

Effective temperatures in a sheared colloidal suspension

2.1 Introduction

The content of this chapter can also be found in the two articles [1, 2].

Temperature is a very important concept in physics, chemistry, biology, etc. In an equilibrium system, the temperature has been well defined and studied. Not only the thermodynamic properties but also their fluctuations are controlled by the temperature [3]. In the linear response regime close to the equilibrium, the fluctuation-dissipation theorem (FDT) is satisfied, which connects the dynamical quantities, such as the time dependent correlation functions and the response functions, to the temperature.

On the other hand, when the system is out of equilibrium, the notion of temperature is poorly defined and understood. Furthermore the fluctuation-dissipation theorem is not valid any more. Cugliandolo et al. [4, 5] first introduced the concept of so called ‘effective temperature’ by generalizing FDT to nonequilibrium systems. They pointed out that for either the aging glass or a system continuously perturbed by an external driving force, there exist two or more time scales. In each time scale, FDT can be extended by using an effective temperature instead of the bath temperature. Cugliandolo et al. [5] further showed that the effective temperature played the same role in the nonequilibrium state as the ordinary temperature did in the equilibrium system. For instance, the effective temperature controls the direction of the heat flow in a simple spin-glass model [5]. The shortcoming is that the effective temperature depends on the choice of the observables [5]. Their important findings have generated intensive interest in investigating the effective temperatures of the nonequilibrium state [6, 7, 8, 9, 10].

For aging systems, calculations of the effective temperatures from the modified fluctuation-dissipation theorem are not easy to do, because of the failure of time translational invariance (TTI). The time correlation functions and the response functions are not only dependent on the time intervals, but also depend on the waiting time. Fortunately, for a stationary nonequilibrium system, TTI is recovered and those dynamic

quantities can be calculated simply [11, 12]. Berthier et al. [11, 13] applied a shear on glassy system and supercooled liquids to generate a stationary state. By simulating the binary Lennard-Jones mixture (Kob-Andersen model) [14], they found a two-temperature pattern. On short time scales, FDT holds with the bath temperature, implying that shear does not affect the system yet [3]. On the contrary, for the slow modes, the effective temperatures, which are calculated by the modified FDT, are larger than the bath temperature. They calculated the effective temperatures based on the definitions involving different observables and found that the effective temperature was not dependent on the observables, showing important thermodynamic characteristics [13]. Moreover, they found for the sheared glassy system, the effective temperatures went down with decreasing shear rate, and finally reduced to a temperature, which was recognized as the effective temperature of the corresponding undriven glass with the same bath temperature [11]. This result provided a method to study the glassy system by introducing a limiting drive [11, 12].

Although in most of the investigations the effective temperatures are defined and calculated from the time-dependent quantities, Liu and Nagel et al. [3, 15] attempted to generate the effective temperatures from the static linear responses, since in an equilibrium situation those methods indeed yield the thermodynamic temperature. They considered a binary mixture and used three different interparticle potentials on the system separately [3]. For each model, the effective temperatures were calculated via the fluctuation-dissipation theorem and the static linear response with various observables. In most of the cases, the effective temperatures evaluated from the static quantities matched well with those calculated from the dynamic properties. Especially they argued that the static linear response could generate good results in the long wave length limit [3]. In contrast, for some other cases, FDT and the static linear response did not yield identical results. They thus concluded that it is not clear in which situation the FDT method should be employed and when the effective temperature can be calculated from the static linear response.

The nonlinear response regime for a system out of equilibrium has been studied by Hayashi and Sasa et al. [16, 17, 18]. They made a series of investigations on the effective temperatures of the systems at the nonequilibrium steady states (NESS). The extended Einstein relation is valid even beyond the linear response regime (for example, the system is perturbed by a large external force), and the effective temperature can be defined from the extended Einstein relation [16, 17, 18]. More importantly, they found that this kind of effective temperature has some the features that the normal temperature possesses. For instance, the effective temperature can determine the probability density in a large-scale description [16]. Moreover, if one employs a Langevin system in the NESS as a moving thermostat and let it contact with a Hamiltonian system, the kinetic temperature of the Hamiltonian system will finally coincide with the effective temperature of the thermostat, and the direction of the heat flow is controlled by T_{eff} [18].

In addition to a lot of investigations on various definitions and calculations of the effective temperatures for different nonequilibrium systems, many efforts have also been devoted to researching the relations between the effective temperature and other physical quantities. Here we briefly introduce three inspiring research results reported in the past five years. Haxton et al. [19] explored a driven glassy system and showed that the effective temperature did have an influence on some properties such as the shear stress and the average inherent structure energy by helping the system to overcome the energy barriers. Furthermore, it is appropriate to say that the effective temperature, rather than the bath temperature, is the one to determine the dynamic properties of the system [19]. Ilg et al. [20] studied a model for the sheared glassy system. They found that the reaction rates to overcome the energy barriers are controlled by the effective temperature. Lu et al. [21] studied the effective temperature in the gene networks and showed that it can be used to figure out the reason of the noise distribution in the stochastic cell biology. Their works encourage people to extend the applications of effective temperatures to the biological area. A recent review on the effective temperature, which gives a full introduction to this subject, was composed by Cugliandolo [22].

So far, most investigations are focused on the glassy system and supercooled liquid under small steady shear [3, 11, 12, 13]. In these cases, the shear rates are usually too small to distort the structure of the system [13]. In this chapter, we utilize the Brownian dynamics simulation to study a monodispersed colloidal system which is far from the glass transition. Thus it is equilibrium if without drive. Stationary states are generated by imposing large shear on the liquid. As a consequence, our systems are strongly anisotropic due to high shear rates. The structure distortion can be observed from the pair distribution function and the static structure factor [23, 24]. Thus it is reasonable to suspect that the effective temperatures in the highly sheared liquids are anisotropic too. To examine this speculation, we calculate the effective temperatures along both the velocity gradient direction and the vorticity direction. We do observe the difference in the results along these two directions. The effective temperatures are defined and calculated in four different ways. Two of them are generated from the modified fluctuation-dissipation theorem and the other two are calculated from static quantities. Specifically, the first one is defined based on the generalized Einstein relation and the second one is evaluated from the parametric plot involving the self-intermediate scattering function [13]. Inspired by Liu et al. [3], we calculate the third effective temperature according to the static linear response relation with the long wavelength limit. The last one is yielded from the particle distribution of the system perturbed by a large external force (nonlinear response regime). All the four effective temperatures have the same shear-rate dependence. Three of them, except the third one defined by the static linear response, give considerably the same results. The effective temperatures along the velocity gradient direction are somewhat larger than those in the vorticity axis.

This chapter is organized in the following way. In section 2, we introduce the details of simulation. In section 3, by employing the pair distribution function and the static structure factor, we first study the structures of the liquid subjected to the steady shear. In section 4, we utilize four different methods to define and calculate the so called effective temperature for the system with various shear rates. In section 5, we summarize the main conclusions of this chapter and suggest some future investigations.

2.2 Simulation

We conduct numerical simulations of a simple system containing only one component of spherical colloidal particles. Following the previous studies done by Szamel [25], the total number of particles is $N = 1372$. The dimensionless density $(N/V)\sigma^3 \equiv n\sigma^3$ equals 0.408 (V is the volume of the system and σ is the diameter of the spherical colloidal particle). By comparing the structure factors of this model with those predicted for the hard-sphere suspensions [26], Szamel [25] found that the density of our system corresponds to an effective hard-sphere volume fraction $\phi = 0.43$, which is moderately dense.

To determine the interparticle force, the repulsive screened Coulomb potential is employed [27],

$$V(r) = A \frac{\exp[-\kappa(r - \sigma)]}{r} . \quad (2.1)$$

In this equation, r is the position of the particle, κ is the inverse Debye length with $\kappa\sigma = 24$, $A = 475k_B T\sigma$ measures the potential strength. In our simulation the Boltzmann constant k_B is set equal to 1.0, and the system is simulated with the temperature $T = 1.0$. For computational efficiency the potential is truncated and shifted at $r = 3\sigma$. With this potential, the interparticle force can then be calculated,

$$\mathbf{F}(r) = -\nabla V(r) . \quad (2.2)$$

In this work we aim to study the non-equilibrated liquid. Thus the shear is imposed along x -direction and the shear gradient is in y -direction. The motion for the i th particle can be described by the Langevin equation [26],

$$\dot{\mathbf{r}}_i(t) = \frac{1}{\xi_0} \sum_{j \neq i} \mathbf{F}(|\mathbf{r}_i(t) - \mathbf{r}_j(t)|) + \boldsymbol{\eta}_i(t) + \dot{\gamma} y_i(t) \hat{\mathbf{e}}_x . \quad (2.3)$$

In equation 2.3, $i = 1, \dots, N$ are the particle indices, $\mathbf{r}_i(t)$ is the position vector of the i th particle at time t , ξ_0 is the friction coefficient of an isolated particle which is taken to be 1.0 in our simulation, $\dot{\gamma}$ is the shear rate, y_i is the coordinate of particle i along the y axis, $\hat{\mathbf{e}}_x$ is the unit vector along the x direction. The

random noise η_i satisfies the fluctuation-dissipation theorem expressed as [26],

$$\langle \eta_i(t) \eta_j(t') \rangle = 2D_0 \delta(t - t') \delta_{ij} I, \quad (2.4)$$

where $D_0 = k_B T / \xi_0$ is the diffusion coefficient and I is the unit tensor. The parameters σ and σ^2 / D_0 define the units of length and time, respectively. All other quantities in this chapter will be presented as a combination of these reduced units.

The Lee-Edwards boundary conditions are applied when we simulate the sheared fluid [28]. The second-order Brownian dynamics algorithm, which combines two steps of first-order BD procedures [29], is used to solve the Langevin equation. First of all, the force on the i particle $\mathbf{F}_i = \sum_{j \neq i} \mathbf{F}(|\mathbf{r}_i(t) - \mathbf{r}_j(t)|)$ is calculated with the positions of all particles and via equation 2.3 the new temporary coordinates $\mathbf{r}'_i(t + \delta t)$ after a time step δt are evaluated. With these temporary positions of particles, the force $\mathbf{F}'_i = \sum_{j \neq i} \mathbf{F}(|\mathbf{r}'_i(t + \delta t) - \mathbf{r}'_j(t + \delta t)|)$ is again measured. Finally the coordinates of the particles at time $(t + \delta t)$ are updated by the average of the two steps,

$$\mathbf{r}_i(t + \delta t) = \mathbf{r}_i(t) - \frac{1}{\xi_0} (\mathbf{F}_i + \mathbf{F}'_i) \delta t / 2 + \boldsymbol{\eta}_i(t) \delta t + \dot{\gamma} \hat{\mathbf{e}}_x (y_i(t) + y'_i(t)) \delta t / 2. \quad (2.5)$$

The second-order algorithm has been demonstrated to be more efficient and to generate better results in comparison with other approaches, such as the first-order Brownian dynamics algorithm and the smart Monte Carlo method [30].

To figure out the effects of the imposed shear on the liquids, various shear rates $\dot{\gamma} = 2, 5, 10,$ and 20 have been selected. To make a complete comparison, we also simulate the corresponding equilibrium system ($\dot{\gamma} = 0$). For $\dot{\gamma} = 0, 2, 5$, the time step is $\delta t = 10^{-4}$, and for larger shear rates $\dot{\gamma} = 10$ and 20 , a shorter time step $\delta t = 5 \times 10^{-5}$ is used. For the highest shear rate $\dot{\gamma} = 20$, we also carry out the simulations with $\delta t = 2 \times 10^{-5}$ to examine if the time step is small enough to generate satisfied accuracy. We found that the results calculated with $\delta t = 5 \times 10^{-5}$ agree very well with those generated from the smaller time step.

With each shear rate the system was equilibrated for about $40 - 200 \tau_\alpha$ (τ_α is the α relaxation time associated with some time correlation function) to make certain that the fluid has arrived at the steady state, where time translational invariance (TTI) has been restored. After that we collect the coordinates of all particles every 100 or 200 steps. We do not save the trajectories more often because the configurations do not have significant changes within the short time and the statistical errors of physical quantities decay as $\tau^{-1/2}$ (τ is the interval between two times at which the trajectories are recorded.) [31]. With the saved trajectories, the static properties (i.e. the radial distribution functions and the structure factors) and the

dynamic quantities (such as the mean square displacement) are calculated for the sheared liquid. We have at least four runs for each shear rate and the results are the averages over them.

To extract the effective temperatures T_{eff} , the sheared system may be perturbed by different kinds of external forces. We follow the same procedures described above to generate the quantities, such as the mobility of particles and the density profiles. The effective temperatures are then calculated from these values. On the other hand, we also use a more sophisticated protocol originally introduced by Berthier to achieve the effective temperature based on the fluctuation-dissipation relation [32]. The feature of this method is that the system is unperturbed. The details will be discussed later on.

2.3 Static structure of a sheared simple liquid

2.3.1 Pair distribution function

The pair distribution function $g(\mathbf{r})$, which gives the distribution of distances \mathbf{r} between two particles, is usually utilized to study the structure of the liquids [33]. For the system with pairwise additive potential, many thermodynamic properties, such as the isothermal compression, the pressure, and the internal energy can be expressed with $g(\mathbf{r})$ [26, 33]. For a homogeneous and isotropic system, the pair distribution function depends only on the distance r_{ij} between two particles. Thus it is called the radial distribution function [26]. However, for the nonequilibrium liquid subjected to a shear rate, $g(\mathbf{r})$ is anisotropic and can be written as,

$$g(\mathbf{r}) = \frac{V}{N(N-1)} \left\langle \sum_{i \neq j}^N \delta(\mathbf{r} - \mathbf{r}_j + \mathbf{r}_i) \right\rangle, \quad (2.6)$$

where the brackets $\langle \dots \rangle$ denote the steady-state average. It is hard to visualize the pair distribution function of the anisotropic system directly. Hess and Hanley et al. [23, 34] divided $g(\mathbf{r})$ into a scalar contribution $g^s(r)$ and many different anisotropic corrections.

The scalar component to $g(\mathbf{r})$ can be written as the orientational average of the pair distribution function [23, 34],

$$g^s(r) = \frac{1}{4\pi} \int d\hat{\mathbf{r}} g(\mathbf{r}). \quad (2.7)$$

Notice that $g^s(r)$ depends on the shear rate and is not equal to the radial distribution function $g_{eq}(r)$ for the corresponding equilibrium system [34]. On the other hand, $g^s(r)$ does reduce to $g_{eq}(r)$ as the shear rate vanishes [35].

Amongst the anisotropic components, the term $g_+(r)$, which is the projection of the pair distribution function onto the $\hat{x} - \hat{y}$ plane, make the largest contribution to $g(\mathbf{r})$ [23, 34]. Thus in this work we only

analyze the first two terms for $g(\mathbf{r})$,

$$g(\mathbf{r}) = g^s(r) + g_+(r)\hat{x}\hat{y} + \dots, \quad (2.8)$$

where $g_+(r)$ can be expressed in the following form [23],

$$g_+(r) = \frac{15}{4\pi} \int d\hat{\mathbf{x}}\hat{\mathbf{y}}g(\mathbf{r}). \quad (2.9)$$

When the shear rate is increased, $g_+(r)$ becomes substantial [34].

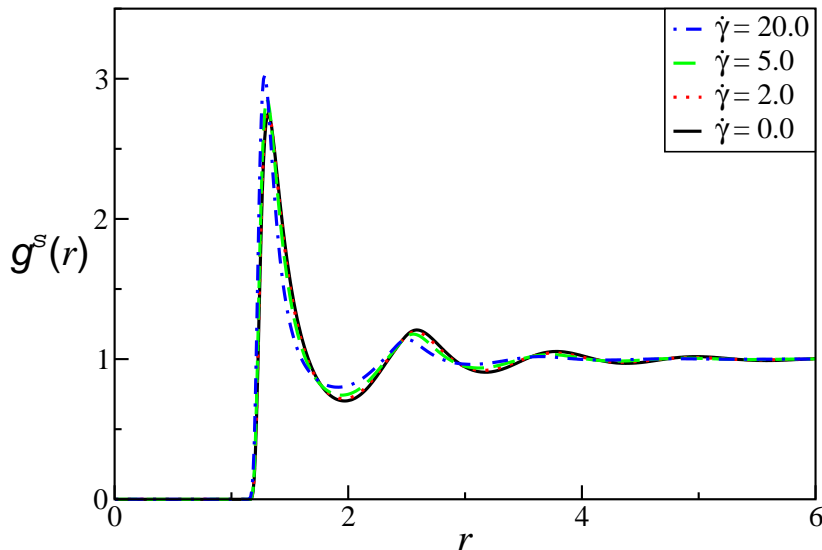


Figure 2.1: The isotropic contribution $g^s(r)$ to the pair correlation function is plotted versus the particle separation r for the system imposed with various shear rates.

First, let us study the isotropic part of the pair distribution function. As seen from figure 2.1, for the equilibrated system ($\dot{\gamma} = 0.0$), $g^s(r)$ is zero at very small pair-particle distance ($r < 1.15$) due to strong repulsive interparticle force [36]. There are two well-defined peaks in $g^s(r)$. The first one at $r = 1.315$ is very high and sharp. The second peak is located at $r = 2.585$ and its height is much shorter than the first one. Figure 2.1 illustrates that with various shear rates we explored, the position and height of the pronounced peak in $g^s(r)$ are almost independent of $\dot{\gamma}$, only the first valley and second peak change slightly. The whole shape of $g^s(r)$ does not change with the applied shear. The typical structures of $g^s(r)$ (two well-defined peaks and no long-range order) demonstrate that the system is still at liquid state even with the very large shear rate $\dot{\gamma} = 20.0$ [36, 37], the shear-induced ordering transition is not seen [35].

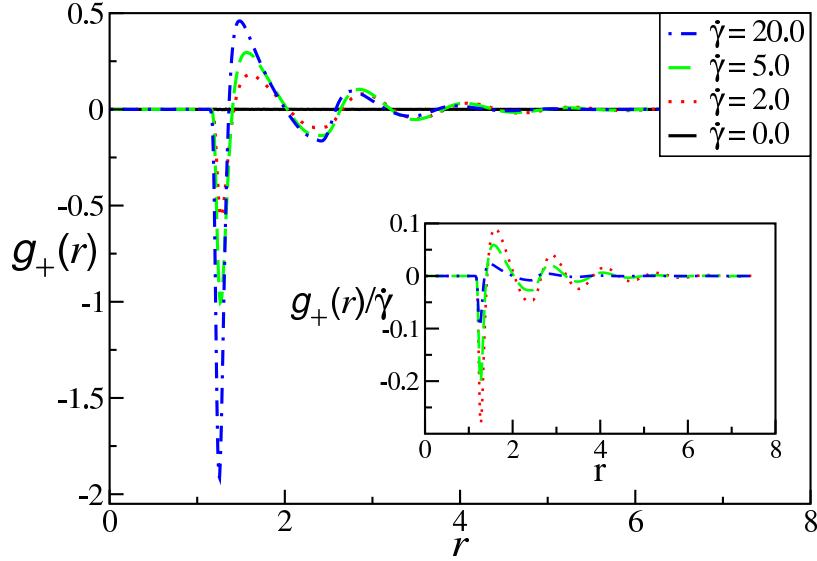


Figure 2.2: The first anisotropic contribution $g_+(r)$ to the pair distribution function is plotted versus the interparticle separation r . The insert figure shows $g_+(r)/\dot{\gamma}$ as a function of r .

Next, let us consider the first anisotropic contribution $g_+(r)$ to the pair distribution function. Although the imposed shear has limited influence on $g^s(r)$, figure 2.2 shows that $g_+(r)$ is affected by the shear. Both the heights of the peaks and the depths of the valleys in $g_+(r)$ increase substantially with larger shear rate. This change in $g_+(r)$ reflects the fact that the liquid becomes more anisotropic under higher shear. At the largest shear rate $\dot{\gamma} = 20.0$, $g_+(r)$ is comparable in magnitude to $g^s(r)$.

What is more, the $x - y$ component of the interparticle shear stress tensor σ_{xy} can be written as the integral of $g_+(r)$ [26, 27],

$$\sigma_{xy} = \frac{n^2}{2} \frac{4\pi}{15} \int_0^\infty dr r^3 \frac{dV(r)}{dr} g_+(r). \quad (2.10)$$

The nonlinear viscosity $\eta(\dot{\gamma})$ due to the pairwise additive interaction force can be related to σ_{xy} via [1, 27],

$$\eta(\dot{\gamma}) = \sigma_{xy}/\dot{\gamma}. \quad (2.11)$$

As illustrated by the insert in figure 2.2, in contrast to $g_+(r)$, $g_+(r)/\dot{\gamma}$ shrinks as the shear rate is higher. Thus according to equation 2.10 and 2.11 the viscosity $\eta(\dot{\gamma})$ decreases when the shear rate is increased. This phenomenon is the so called ‘shear thinning’, which has been observed in many fluids [35, 36, 37]. The reason behind this phenomenon is that the system is more fluid under shear.

Here we only considered the first two terms for the pair distribution function $g(\mathbf{r})$. Both terms depend on the shear rate, although the effect on the isotropic component $g^s(r)$ is very weak. The growth in the first anisotropic term $g_+(r)$ reflects the increase of the anisotropy in the structure of the liquid with higher shear rate. Actually not only $g_+(r)$, other anisotropic contributions become larger too [34]. For the system subjected to an extremely high shear stress, more anisotropic components need to be included to get a more accurate structure of the liquid. Actually, the presence of these anisotropic components is reflected in a rather complex shape of structure factor. The 2-D static structure factors (figures 2.4 and 2.5) will be analyzed in the following subsection.

2.3.2 Static structure factors

The static structure factor $S(\mathbf{k})$ is another very useful tool to explore the structure of the liquid, which can be expressed as the autocorrelation function of the Fourier components of the density $\rho(\mathbf{r}) = \langle \sum_{i=1}^N \delta(\mathbf{r} - \mathbf{r}_i) \rangle$ [26],

$$S(\mathbf{k}) = \frac{1}{N} \langle \rho(\mathbf{k})\rho(-\mathbf{k}) \rangle , \quad (2.12)$$

where $\rho(\mathbf{k})$ is the Fourier transform of the local density $\rho(\mathbf{r})$ and can be written in the following equation,

$$\rho(\mathbf{k}) = \sum_{i=1}^N \exp(-i\mathbf{k} \cdot \mathbf{r}_i) . \quad (2.13)$$

In the equation, \mathbf{k} is the wave vector. For a homogeneous liquid, the static structure factor is the spatial Fourier transform of the pair distribution function [26],

$$S(\mathbf{k}) = 1 + \rho \int \exp(-i\mathbf{k} \cdot \mathbf{r})(g(\mathbf{r}) - 1) d\mathbf{r} . \quad (2.14)$$

On the other hand, the pair distribution function can also be written as the Fourier transform of the static structure factor [26],

$$g(\mathbf{r}) = 1 + \frac{1}{(2\pi)^3 \rho} \int \exp(i\mathbf{k} \cdot \mathbf{r}) [S(\mathbf{k}) - 1] d\mathbf{k} . \quad (2.15)$$

In equation 2.14 and 2.15, $\rho = \langle \rho(\mathbf{r}) \rangle$ is the average density of the system [26]. Equation 2.15 is very meaningful, because the static structure factor can be measured directly by the X-ray or neutron scattering experiments, in which $S(\mathbf{k})$ is related to the cross-section [26]. Then the pair distribution function can be calculated via equation 2.15. It provides an alternative way to get $g(\mathbf{r})$, but this procedure is not always practical because it requires knowing $S(\mathbf{k})$ for a very large number of wavevectors.

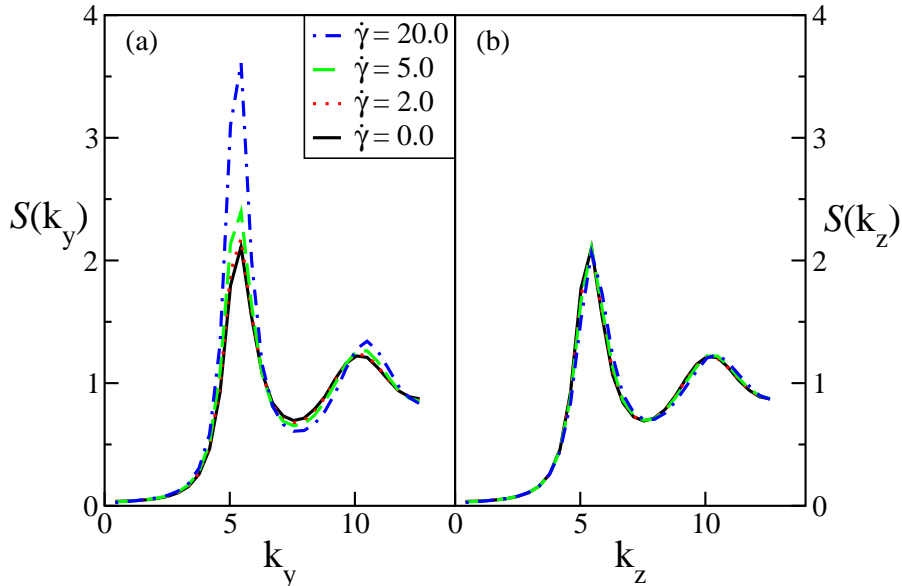


Figure 2.3: The static structure factor $S(k)$ versus the wave vector k at various shear rates along different directions: (a) velocity gradient direction $\hat{\mathbf{e}}_y$, (b) vorticity direction $\hat{\mathbf{e}}_z$.

With numerical simulations, the structure factors can be calculated from equation 2.12 and 2.13. As is clearly visible in figures 2.3, the static structure factors along the velocity gradient direction ($\hat{\mathbf{e}}_y$) and along the vorticity direction ($\hat{\mathbf{e}}_z$) are identical for the equilibrium case ($\dot{\gamma} = 0$), showing that the system is isotropic as expected. The principal peak is located at around $k_{\max} = 5.45$ and its height is about 2.1.

As illustrated in figure 2.3, when the shear rate is increased, $S(k)$ along the vorticity direction remains unchanged. In contrast, along the velocity gradient direction a prominent enhancement is observed in the primary peak, although the position of the peak does not move. Besides, the second peak in $S(k_y)$ also grows slowly and the first valley becomes somewhat deeper with increasing shear rate. As a consequence, the discrepancy between the static structure factors along the two directions perpendicular to the flow appears around $\dot{\gamma} = 5.0$ (possibly also at a smaller shear rate, however we do not have data between 2.0 and 5.0). This difference indicates anisotropy of the liquid, which was also evident from $g_+(r)$. The similar phenomenon for $S(\mathbf{k})$ has been seen by Xue et al. [38] in a fluid subjected to an oscillating shear flow. The growth in $S(k_y)$ is speculated due to the slight local layering along the velocity gradient direction [38].

Above we have shown that the structure factors along the velocity gradient direction and the vorticity direction have different variation as the the shear rate increases. Now it is natural to ask what the crossover between those directions looks like. To figure out this question, the contour plots of $S(\mathbf{k})$ in some specific

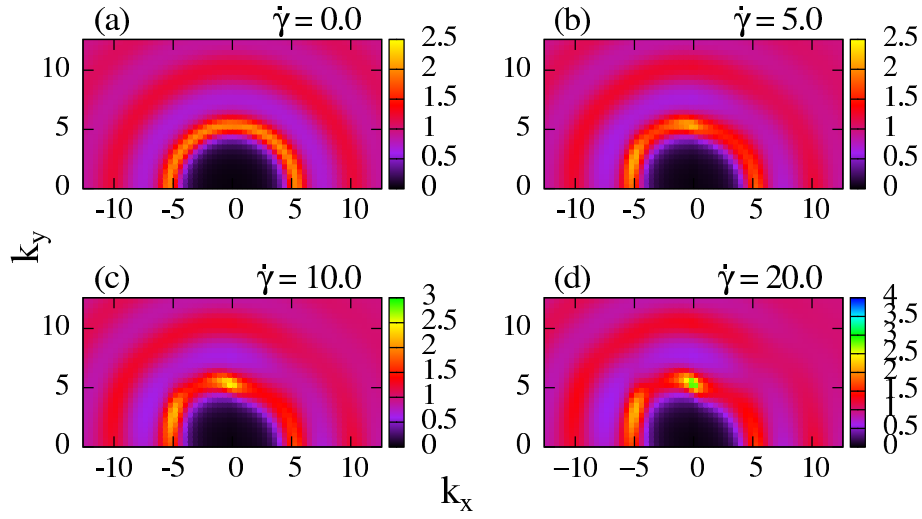


Figure 2.4: The contour plots for the static structure factor $S(\mathbf{k})$ on the flow-velocity gradient ($x - y$) plane at various shear rates.

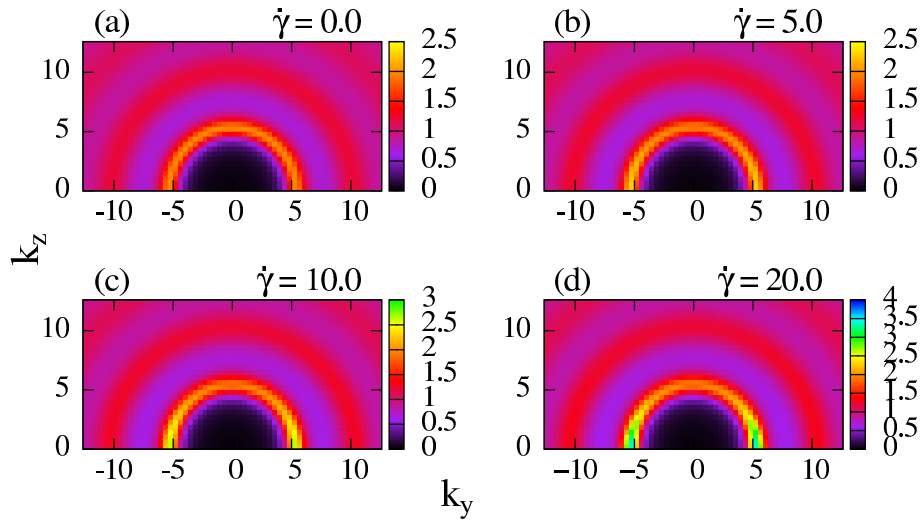


Figure 2.5: The contour plots for the static structure factor $S(\mathbf{k})$ on the velocity gradient - vorticity ($y - z$) plane at various shear rates.

planes in the wave vector space can be employed. The static structure factor $S(\mathbf{k})$ in the planes can also be measured directly via the multi-detector technique in the scattering experiments. Thus one can make a comparison between the experimental data and the simulation results [35]. The contour plots for $S(\mathbf{k})$ have been frequently used to illustrate the shear induced distortion in the nonequilibrium liquids [24, 35, 39].

In figure 2.4 we plot the structure factor $S(\mathbf{k})$ for various shear rates on the flow - velocity gradient ($x - y$) plane. Without shear the ring pattern is well structured, implying that the liquid is isotropic on the plane. After applying a small shear on the liquid ($\dot{\gamma} = 5.0$), a peak appears at around ($k_y = 5.45$) along $\hat{\mathbf{e}}_y$ direction, which is in consistent with figure 2.3. Another peak occurs enclosing the point ($k_x = 5, k_y = 2$). There is approximately a ‘symmetry’ axis between this two peak with an angle about 150° from the flow direction. When the shear rate is further increased, the peak along $\hat{\mathbf{e}}_y$ direction grows intensively, while the other peak seems unchanged. The ‘symmetry’ axis rotates to the velocity gradient direction. A similar phenomenon has been reported by Hess [24]. When the system is highly sheared ($\dot{\gamma} = 20.0$), the ring-like structure is deformed strongly.

The contour plots for $S(\mathbf{k})$ in the velocity gradient - vorticity ($y - z$) plane for different shear rates are depicted in figure 2.5. Again we see the isotropic ring if the shear rate is zero. As the shear rate grows, the increases in $S(\mathbf{k})$ are only observed along the velocity gradient direction at about $|k_y| = 5.45$. The deformation of the ring-like pattern does not happen even at the largest shear rate.

In this section, with the help of pair distribution function and static structure factor, we have investigated the microstructure of the nonequilibrium liquid driven by the shear flow. The isotropic part $g^s(r)$ of the pair distribution function shows very weak dependence on the shear rate, while the shear induced distortion is seen from the first anisotropic component of $g(\mathbf{r})$. With inspection the plots of $S(\mathbf{k})$ parallel to $\hat{\mathbf{e}}_y$ and $\hat{\mathbf{e}}_z$ directions, the anisotropy of the liquid is again demonstrated. Moreover, we also investigated the contour plots of $S(\mathbf{k})$ on the $x - y$ and $y - z$ planes, which give more complete pictures about the microstructure of the liquid under shear flow.

2.4 Effective temperatures

Our objective for this present study is to determine the effective temperatures based on four different definitions. The first effective temperature is extracted from the extended Einstein relation [9]. The self-diffusion constant is calculated for the particles in the steady state and the mobility is then extracted when the selected particles are perturbed by a constant external force. The second effective temperature is calculated from the generalized fluctuation-dissipation theorem. The self-intermediate scattering function is used as the correlation function and the susceptibility is calculated from the variation in the Fourier transform of the local particle density due to the external force. We calculate the susceptibility using the method proposed by Berthier [32]. The third effective temperature is generated from the static linear response, with considering the density variation due to the external potential. For the last method, a tracer particle in the sheared liquid is perturbed by a quite larger external potential (out of the linear response regime) along the two

directions transverse to the shear flow, separately, and the distributions of the tagged particle along relevant direction are calculated. After fitting the density profiles with the equation recently proposed by Szamel [2], the effective temperatures are determined. With considering the strong anisotropy of the highly sheared system, all the effective temperatures are evaluated along both the velocity gradient direction $\hat{\mathbf{e}}_y$ and the vorticity direction $\hat{\mathbf{e}}_z$.

2.4.1 From the Einstein relation

When a system is equilibrated, the self diffusion constant and the mobility of a tagged particle can be connected to the bath temperature according to the well-known Einstein relation, which is actually a specific form of the fluctuation-dissipation theorem [16, 26, 40],

$$D_{eq} = k_B T \mu_{eq} , \quad (2.16)$$

where the self-diffusion constant D_{eq} can be extracted from the spontaneous mean square displacement in the diffusive regime (t is large) [26],

$$D_{eq} = \lim_{t \rightarrow \infty} \frac{1}{6t} \langle |\mathbf{r}_i(t) - \mathbf{r}_i(0)|^2 \rangle_{eq} . \quad (2.17)$$

On the other hand, if a tagged particle is under action of a small constant external force F_0 from $t = 0$ onwards, the mobility, which is due to the friction between the particles, can be calculated from the systematic displacement of the labeled particle after a long time [9],

$$\mu_{eq} = \lim_{F_0 \rightarrow 0} \lim_{t \rightarrow \infty} \frac{1}{tF_0} \left\langle [\mathbf{r}_i(t) - \mathbf{r}_i(0)] \cdot \hat{\mathbf{f}} \right\rangle_{eq}^{F_0} . \quad (2.18)$$

In equation 2.17 and 2.18, $\langle \dots \rangle$ denotes an average over different initial times. $\hat{\mathbf{f}}$ is the unit vector, denoting the direction of external force.

Although the Einstein relation holds rigorously for the equilibrium system [9], it is violated for a system far from the equilibrium [41]. Specifically, for the nonequilibrium stationary system driven by a shear flow, the diffusion coefficients along various directions depend on the shear rate [38, 42, 43]. A theoretical analysis of the shear rate dependence for the self-diffusion coefficient and the mobility of a colloidal suspension in a semidilute solution has been made by Szamel et al. twenty years ago [41]. They found both the diffusion constant and the mobility depended on the shear rates, but in different ways. In fact, the difference in the behavior of D and μ with imposed shear gives the possibility to define the so called effective temperature via

the Einstein relation [1]. Later on, Berthier and Barrat demonstrated numerically that if the system is at stationary state, the modified Einstein relation is valid by introducing the the notion of effective temperature as the alternative to the ordinary temperature [13]. In other words, the effective temperature for a system in the steady state can be calculated by,

$$k_B T_{eff} = D/\mu , \quad (2.19)$$

where D is the self-diffusion coefficient of a tracer particle in the nonequilibrium stationary system and μ is its mobility if the particle is dragged by a small external force. The Boltzmann constant k_B is set equal to 1 in the calculation.

Given the strong anisotropy in our system due to high shear rate, we calculate the effective temperatures along the two directions transverse to the shear flow, namely, the velocity gradient axis $\hat{\mathbf{e}}_y$ and the vorticity axis $\hat{\mathbf{e}}_z$.

$$T_{eff}^\alpha = D_{\alpha\alpha}/\mu_{\alpha\alpha} \quad (2.20)$$

In the above equation $\alpha = y$ or z . The diagonal components of the self diffusion tensor can be calculated from the mean square displacement along the corresponding direction,

$$D_{\alpha\alpha} = \lim_{t \rightarrow \infty} \frac{1}{2t} \langle [\alpha_i(t) - \alpha_i(0)]^2 \rangle . \quad (2.21)$$

The diffusion coefficients can be calculated directly from the simulated trajectories of the particles in the sheared liquid. The only thing one may need to notice here is to ensure that the simulation time is long enough and the system has entered into the diffusive regime.

On the other hand, the mobility due to the force-induced displacement can be evaluated from,

$$\mu_{\alpha\alpha} = \lim_{F_0 \rightarrow 0} \lim_{t \rightarrow \infty} \frac{1}{tF_0} \langle [\alpha_i(t) - \alpha_i(0)] \cdot \hat{\mathbf{f}} \rangle^{F_0} . \quad (2.22)$$

To calculate the mobility along the direction $\hat{\mathbf{e}}_\alpha$ (α can be y or z), we use the final configurations of previous simulations (without external force) with the same shear rate as the initial coordinates of the particles in the system. Following the strategy introduced by Berthier and Barrat [13], at $t = 0$, we randomly choose 343 ($= N/4$) particles, exert a small constant force $F_0 = 0.1$ along the positive direction along $\hat{\mathbf{e}}_\alpha$ axis. At the same time, we randomly select another 343 particles, apply $F_0 = 0.1$ along the negative direction in $\hat{\mathbf{e}}_\alpha$ axis. In this case, the external forces do not cause a net drift of the whole system. As a results, the mobility can be evaluated from equation 2.22 with taking account of the sign of the force. To make sure

that this method is really acceptable, we repeat the procedure described above with exerting the force on 340 particles. Among them, $F_0 = 0.1$ is imposed on 170 particles along the positive direction in the relevant axis, and for the other 170 particles the force is along the opposite direction. We compare the results to the previous system, in which more particles (686) are imposed by force. As expected, the results are very similar, but with larger error bars. Finally, the effective temperatures of the system with each shear rate can be calculated via equation 2.20. The diffusion coefficient, the mobility and the effective temperatures along the two directions \hat{e}_y and \hat{e}_z are plotted versus shear rate in figure 2.6.

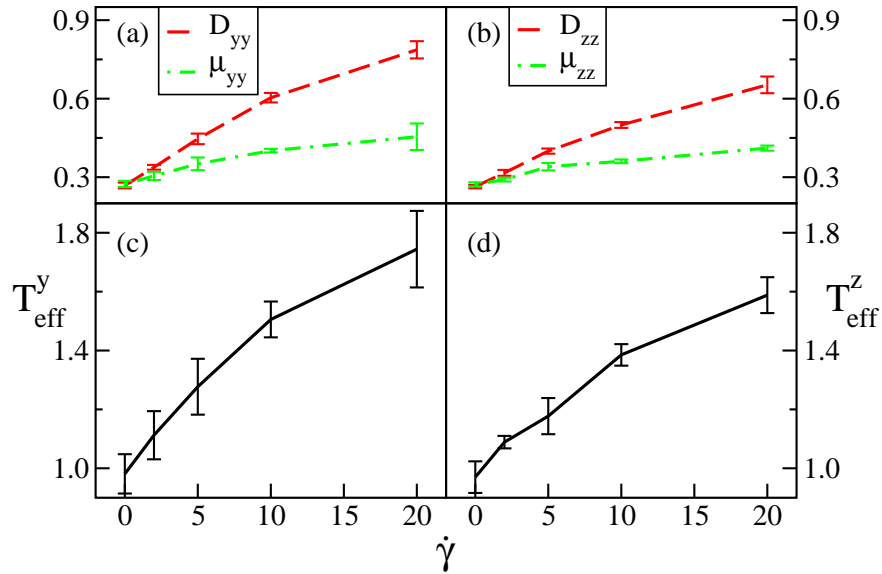


Figure 2.6: The upper two panels (a) and (b) show the diagonal elements of the self-diffusion tensor and the diagonal exponent of the self-mobility tensor of the liquid driven by various shear. The lower two panels (c) and (d) illustrate the shear dependence of the effective temperature calculated by equation 2.19. (a) and (c) show quantities measured along the velocity gradient direction \hat{e}_y ; (b) and (d) show them along the vorticity direction \hat{e}_z .

As seen in figure 2.6, both the diffusion coefficient and the mobility are enhanced monotonically when the system is driven by a higher shear flow. Similar observations have been reported before [38, 43, 44]. Moreover, we find that with larger $\dot{\gamma}$, D and μ along the velocity gradient axis are systematically bigger than those in the vorticity direction. Especially for the diffusion coefficient, the discrepancy grows with shear rate. Recently, Lander et al. [44] also investigated the diffusion and mobility of a model similar to ours, but they imposed on the system a much smaller shear ($\dot{\gamma} \leq 1.0$). As a consequence, their system was not anisotropic and the difference in the diffusion coefficients between the flow gradient direction and the vorticity direction was not observed in their case. The anisotropy in diffusion was reported by Xue et al. [38] long time ago,

where they applied an oscillating shear to the system. However, they found that the diffusion coefficient parallel to the velocity gradient axis was smaller than that along the vorticity gradient. Later on, Indrani et al. made a theoretical analysis on the system imposed by a steady shear flow. In contradiction with the results reported by Xue et al. [38], they found that with high shear rate, the diffusion coefficient along the velocity gradient direction was larger. Their finding is qualitatively consistent with ours.

Figure 2.6 also shows that without shear ($\dot{\gamma} = 0.0$), the diffusion constants are equal to the mobilities along each direction ($\hat{\mathbf{e}}_y$ and $\hat{\mathbf{e}}_z$). As a result, the effective temperatures along both directions are 1.0, reducing to the bath temperature. When the shear rate increases, the effective temperatures along both directions grow monotonically. Besides, T_{eff} along the velocity gradient direction are somewhat larger than those in the vorticity direction, especially in the case of larger shear rates. However, due to the quite big errors, we cannot make an assertion that the effective temperature is direction dependent.

2.4.2 Fluctuation-dissipation violation

For the equilibrium system, the susceptibility due to a small external perturbation can be linked to the time correlation function by the fluctuation-dissipation theorem in the linear response regime [5, 13, 45],

$$\chi_{A,B}(t)_{\text{eq}} = \frac{1}{k_B T} [C_{A,B}(t, t)_{\text{eq}} - C_{A,B}(t, 0)_{\text{eq}}] . \quad (2.23)$$

In the above equation, T is the bath temperature, $C_{A,B}(t, t')_{\text{eq}} = \langle A_{\text{eq}}(t) B_{\text{eq}}(t') \rangle$ is the time correlation function of two dynamic quantities $A_{\text{eq}}(t)$ and $B_{\text{eq}}(t)$ [26]. The susceptibility is the integral of the response due to a small perturbing field $h(t)$ [5, 32, 45],

$$\chi_{A,B}(t)_{\text{eq}} = \int_{t'}^t dt'' \left. \frac{\partial \langle A_{\text{eq}}(t) \rangle_h}{\partial h(t'')} \right|_{h \rightarrow 0} . \quad (2.24)$$

If we choose the two dynamic variables A and B as the following forms,

$$A_{\text{eq}}(t) = \frac{1}{N'} \sum_j^N \epsilon_j \exp[i\mathbf{k} \cdot \mathbf{r}_j(t)] , \quad (2.25)$$

$$B_{\text{eq}}(t) = 2 \sum_j \epsilon_j \cos[i\mathbf{k} \cdot \mathbf{r}_j(t)] , \quad (2.26)$$

then $C_{A,B}(t, t')_{\text{eq}}$ is the self-intermediate scattering function $F_{s,\text{eq}}(\mathbf{k}, t)$ [32]. In the expression of $A_{\text{eq}}(t)$, N' denotes the number of particles exerted by the external force. If one enforces a small external perturbation

$hB(t)$ with an constant amplitude h [32], then the force exerted on each selected particle is,

$$\mathbf{F}_j^{ext} = -\partial\{2h\epsilon_j \cos[i\mathbf{k} \cdot \mathbf{r}_j(t)]\}/\partial\mathbf{r}_j, \quad (2.27)$$

where $\epsilon_j = -1, 0, 1$, with $\sum_j^N \epsilon_j = 0$ chooses which particle is perturbed by the external force and also determines the direction of the force. The susceptibility of the system perturbed by the external force can be written as,

$$\chi_{s,eq}(k, t) = \frac{\partial}{\partial h} \left\langle \frac{1}{N'} \sum_j^N \epsilon_j \exp[i\mathbf{k} \cdot \mathbf{r}_j(t)] \right\rangle_{eq} \Big|_{h \rightarrow 0}^h. \quad (2.28)$$

Here N' gives the number of particles exerted by the external force ($\epsilon_j \neq 0$). In this case, the susceptibility gives the variation for the Fourier component of the density (defined by equation 2.13) of the system perturbed by a very small external driving force. According to the fluctuation-dissipation theorem,

$$\chi_{s,eq}(k, t) = \frac{1}{k_B T} [1 - F_{s,eq}(k, t)]. \quad (2.29)$$

However, for the out-of-equilibrium system equation 2.29 does not work. Berthier et al. showed numerically that the FDT could be generalized for a stationary nonequilibrium system by introducing the effective temperature [13]. In other words, we can defined the effective temperature by,

$$k_B T_{\text{eff}}^\alpha = \frac{1 - F_s(k_\alpha; t)}{\chi_s(k_\alpha; t)}, \quad (2.30)$$

where $\alpha = y$ or z . For a system under shear, but without external potential, the self-intermediate scattering function can be calculated directly by the following equation [13, 26],

$$F_s(\mathbf{k}; t) = \frac{1}{N} \left\langle \sum_{i=1}^N \exp \{i\mathbf{k} \cdot [\mathbf{r}_i(t) - \mathbf{r}_i(0)]\} \right\rangle. \quad (2.31)$$

It is quite difficult to measure the susceptibility from,

$$\chi_s(k; t) = \frac{\partial}{\partial h} \langle \exp [i\mathbf{k} \cdot \mathbf{r}_i(t)] \rangle_{eq} \Big|_{h \rightarrow 0}^h. \quad (2.32)$$

One can of course do another set of simulations by considering the perturbation on the system, then calculate the susceptibility numerically from the trajectories via equation 2.32. However, this method is obviously not efficient. Recently, Berthier [32] proposed an approach to extract the susceptibility from the unperturbed trajectories. In this case, the self-intermediate scattering function and the susceptibility can be generated

at the same time. To achieve this aim, a quantity $\phi_i = \partial \mathbf{r}_i / \partial h$ is necessary to be employed to calculate the susceptibility. Given an external force along the velocity gradient direction, the susceptibility along the relative direction can be expressed as,

$$\chi_s(k_y; t) = \frac{1}{N'} \left\langle \sum_{j=1}^N \epsilon_j k_y \sin(k_y y_j) \phi_{j,y} \right\rangle_0. \quad (2.33)$$

The details of the derivation are listed in the appendix.

In the simulation, we randomly choose 686 particles. Among them, an external force is exerted on 343 particles along the positive direction of the relevant axis, and the perturbation is along the opposite direction for the other 343 particles. For each combination of $\dot{\gamma}$ and k_α ($\alpha = y$ or z), we simulate four independent samples. For each sample, the susceptibilities is calculated by averaging over different initial time. Since the noise in the susceptibility becomes very large as the time goes on, the time interval in which the susceptibilities are calculated are not necessary to be long. In our case, we calculate $\chi_s(k_\alpha, t)$ for $t \leq 1.0$. Compared with the work of Berhier [32], there are two features for our system. First, with the Brownian dynamics simulation, there is no momentum. Thus only $\partial \mathbf{r}_i / \partial h$ needs to be considered. Secondly, the liquid under steady shear is at stationary state, and time translational invariance is valid, so we can calculate the dynamic quantities with a long run instead of many independent short runs. These two features make our simulations easier than those done by Berthier [32].

To illustrate how the shear rate affects the time evolution of the self-intermediate scattering function and the susceptibility, figure 2.7 is generated, in which the wave vector $k_y = 5.45$ is the peak position for $S(k_y)$. We only exhibit the results along the velocity gradient direction. $F_s(k_z, t)$ and $\chi_s(k_z, t)$ have similar shear-rate dependence, thus are omitted. Figure 2.7 shows that for very short time, both $F_s(k_y, t)$ and $\chi_s(k_y, t)$ are unchanged by the shear, while for longer time, the influence of shear is obvious. When the shear rate becomes larger, the self-intermediate scattering function decays to zero more quickly. As a result, the relaxation time τ , defined as $F_s(k_y, \tau) = e^{-1}$, decreases when the system is driven by higher shear flow, exhibiting ‘shear thinning’ behavior. The susceptibility is seen decreasing with increasing $\dot{\gamma}$. When time is longer than about 0.2, the noise in the susceptibility becomes very large, especially for the system with higher shear rate. To improve the quality of figure, the noise part is excluded.

We also did the wave vector analysis for the self-intermediate scattering function and the susceptibility of the system with shear rate $\dot{\gamma} = 20.0$. Again only the quantities along $\hat{\mathbf{e}}_y$ axis are depicted, since the wave-vector dependence is similar for $\hat{\mathbf{e}}_z$ direction. It is clearly seen in figure 2.8, with larger wave vector, $F_s(k_y, t)$ decreases and so does the relaxation time. The susceptibility is enhanced when the wave vector is bigger.

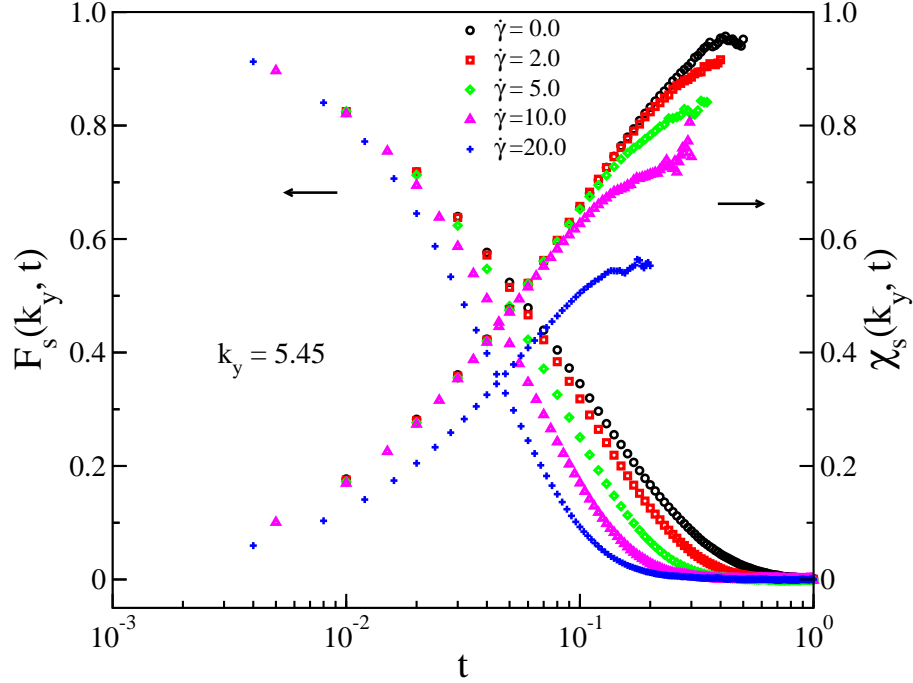


Figure 2.7: The self-intermediate scattering function $F_s(k_y, t)$ and the susceptibility $\chi_s(k_y, t)$ of the system with various shear rates are plotted versus the time along the velocity gradient direction \hat{e}_y . The wave vector $k_y = 5.45$ is the peak position in the static structure factor $S(k_y)$.

To extract the effective temperatures, we make the parametric susceptibility-correlation plots as suggested by Berthier et al. [13]. In figure 2.9, we give an example of this kind of plot, where we list four different wave vectors and the shear rate is $\dot{\gamma} = 20.0$. As is clearly visible in figure 2.9, in the shorter time scale, when the self-intermediate scattering function is large and the susceptibility is small (the right bottom corner in the graph), all the dots fall on the solid line $\chi(t) = C(t)$, denoting that for all the wave vectors the fluctuation-dissipation theorem holds with the bath temperature $T = 1.0$. For longer time, the dots deviate from the solid line. For each wave vector, the fittings for the dots in the long time scale are shown by the dashed line with the slope $-1/T_{\text{eff}}$. We find that the effective temperatures are higher than the bath temperature. This two-temperature scenario agrees very well with the prediction made by Berthier et al. [12].

It is also illustrated by figure 2.9 that all the dashed lines are parallel to each other in the long time range, indicating that the effective temperature is independent of the choice of the wave vector. The same conclusion has been made by Berthier et al. for a binary Lennard Jones mixture with the temperature in the vicinity of the critical temperature $T_c = 0.435$ predicted by the mode coupling theory [13]. The wave vector independence is useful. As we have shown in figure 2.8, with larger wave vectors, the correlation function decays to zero very quickly, with the result that only a few points can be used to fit in the parametric plots (see the case with $k = 10.48$ in figure 2.9). In this case, the effective temperature is not accurate enough.

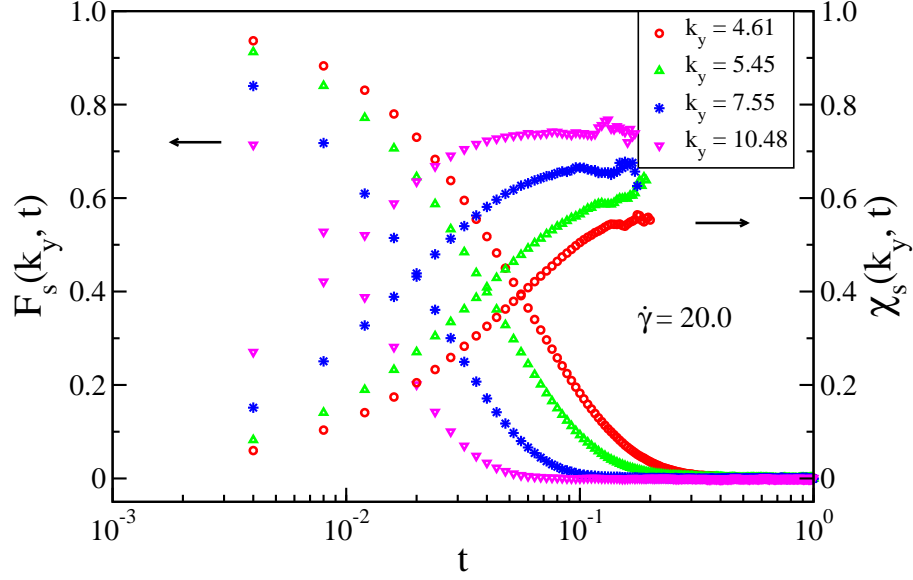


Figure 2.8: The self-intermediate scattering function $F_s(k_y, t)$ and the susceptibility $\chi_s(k_y, t)$ along the velocity gradient direction \hat{e}_y are depicted versus the time. Four different wave vectors are considered and the shear rate is 20.0.

Fortunately, due to the wave vector independence, one can calculate T_{eff} with selecting smaller wave vector to get better results.

Finally, all the effective temperatures for the system driven by the shear flow with different $\dot{\gamma}$ are calculated from the parametric plots and depicted in figure 2.10. From the graph, we can see that the effective temperatures along both the velocity gradient direction and the vorticity direction grow with increasing shear rate. At each fixed $\dot{\gamma}$, the effective temperatures are the same for all the wave vectors we explore here. Moreover, we find that the effective temperatures along the velocity gradient direction are higher than those along the vorticity direction. This is more evident when the shear rate is larger, i.e. $\dot{\gamma} = 20.0$.

So far, we have calculated the effective temperatures with two definitions originating from the fluctuation-dissipation theorem. According to Berthier [13], the effective temperatures generated from the modified FDT do not depend on the observables. In other words, these two effective temperatures should be comparable to each other. To make a comparison, we plot them in figure 2.11. For the second method involving the self-intermediate scattering function, the effective temperatures calculated with the wave vector $k = 5.45$ are exhibited here. As shown in the figure, within the statistical errors, the results measured from the two observables are consistent with each other, especially when the shear rates are not too large ($\dot{\gamma} \leq 10.0$). Moreover, the effective temperatures extracted from the second method have much better statistics.

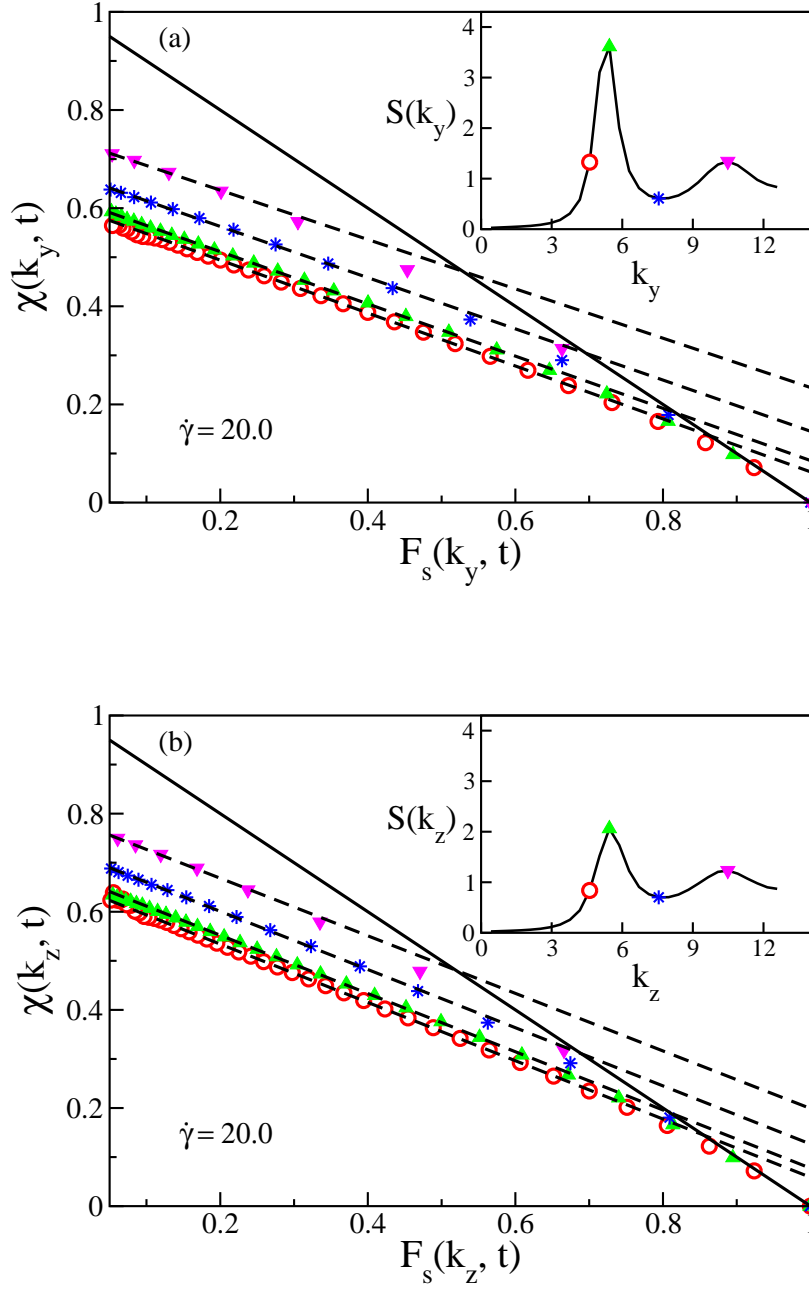


Figure 2.9: Comparison of the parametric plots $\chi_s(k_\alpha, t)$ versus $F_s(k_\alpha, t)$ for four different wave vectors along two directions perpendicular to the flow. From top to bottom the wave vectors are $k_\alpha = 10.48, 7.55, 5.45$ and 4.61 , corresponding to those dots labeled on the static structure factor shown in the insert. The solid lines illustrate the equilibrium FDT with the slope $-1/T$ and T is the bath temperature. The dashed lines give the linear fits to the data in the long time scales (small $F_s(k_\alpha, t)$) and the slopes of these lines are $-1/T_{eff}$. The subscript α can be either y or z , denoting the directions. Figure (a) shows the results along the velocity gradient direction \hat{e}_y and figure (b) is along the vorticity direction \hat{e}_z .

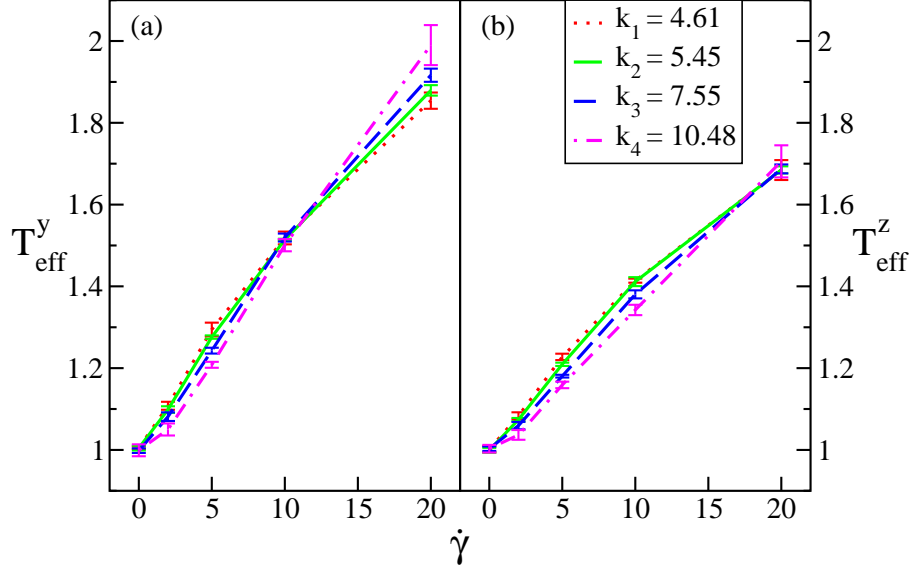


Figure 2.10: The effective temperatures extracted from the parametric plots involving the self-intermediate scattering function are depicted versus the shear rates. The effective temperatures are calculated with four different wave vectors along two directions transverse to the flow. Figure (a) shows T_{eff} along the velocity gradient direction $\hat{\mathbf{e}}_y$, and figure (b) shows that in the vorticity direction $\hat{\mathbf{e}}_z$. Error bars are based on the average over four runs.

2.4.3 Static linear response function

In the previous two subsections, we have calculated the effective temperatures from dynamic quantities. In the present part and the next subsection, we will generate the effective temperatures from static variables. In the equilibrium state, when the system is driven by a small static spatially-varying external potential $V^{\text{ext}}(r)$, the linear response to the perturbation is determined by the static structure factor $S(\mathbf{q})$ [26]. For instance, the variation in the Fourier component of the density $\delta\rho(\mathbf{q})$ can be expressed as [26],

$$\delta\rho(\mathbf{q}) = -\frac{S(\mathbf{q})}{k_B T} \rho \delta V^{\text{ext}}(\mathbf{q}) , \quad (2.34)$$

where T is the environment temperature in the above equation, and $\delta V^{\text{ext}}(\mathbf{q})$ is the Fourier transform of the external potential, $\delta V^{\text{ext}}(\mathbf{q}) = \int \exp(-i\mathbf{q} \cdot \mathbf{r}) V^{\text{ext}}(\mathbf{r}) d\mathbf{r}$.

Suppose that the system is subjected to a weak, static, oscillating external potential of the form,

$$V^{\text{ext}}(r) = V_0 \sin(\mathbf{q} \cdot \mathbf{r}) . \quad (2.35)$$

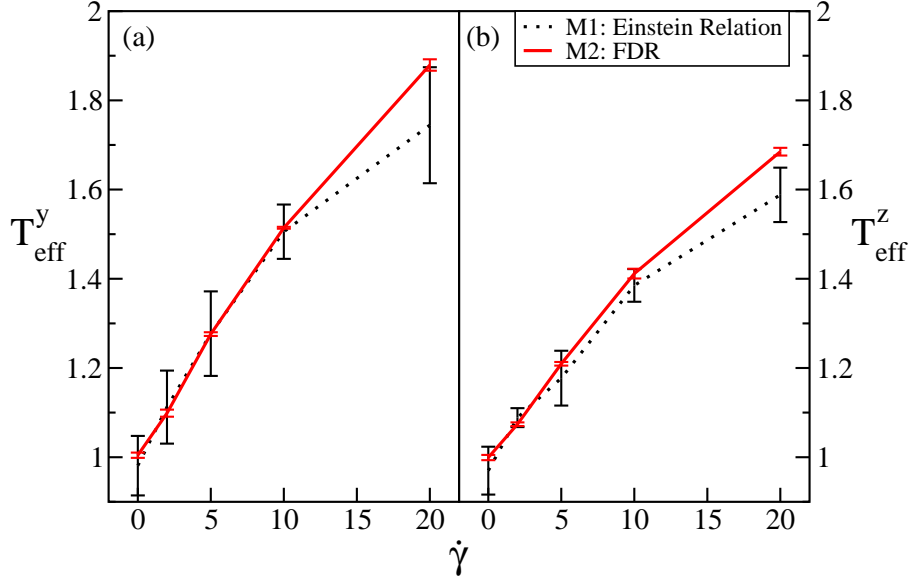


Figure 2.11: The effective temperatures measured from the parametric plots involving the self-intermediate scattering function are depicted versus the shear rate. To calculate $F_s(k_\alpha, t)$ and $\chi_s(k_\alpha, t)$, the wave vector $k_\alpha = 5.45$, at which the structure factor is maximum, is chosen. For comparison, the effective temperatures calculated from the Einstein relation are plotted in this figure again.

The variation of the average density caused by this perturbation can be written as,

$$\delta\rho(\mathbf{r}) = -\frac{\rho S_{\text{eq}}(q)}{k_B T} V_0 \sin(\mathbf{q} \cdot \mathbf{r}) . \quad (2.36)$$

In this equation, $S_{\text{eq}}(q)$ is the static structure factor of the equilibrium system without external potential. To extend this expression into the nonequilibrium cases, we simply use the effective temperature to substitute the bath temperature in the equation, giving,

$$\delta\rho(\mathbf{r}) = -\frac{\rho S(q)}{k_B T_{\text{eff}}} V_0 \sin(\mathbf{q} \cdot \mathbf{r}) . \quad (2.37)$$

In the equation, $S(q)$ is the static structure factor for the nonequilibrium steady state. With a vanishing perturbation, the change in the density is proportional to the amplitude (V_0) of the external potential,

$$\delta\rho(\mathbf{r}) = -\rho a(\mathbf{q}) V_0 \sin(\mathbf{q} \cdot \mathbf{r}) . \quad (2.38)$$

From equation 2.37 and 2.38, we obtained an expression for the effective temperature,

$$T_{\text{eff}}^{\alpha} = \frac{S(q_{\alpha})}{a(q_{\alpha})}. \quad (2.39)$$

Again, $\alpha = y$ or z and we calculate the effective temperature along the two directions transverse to the flow. The calculations of the static structure factor of the sheared system without external perturbation have been discussed before. To generate the linear response coefficient $a(q_{\alpha})$, we perform another two sets of the simulations, applying small external potential (with different V_0) to the system along a specific axis at $t = 0$. The coefficient $a(q_{\alpha})$ is then obtained by comparing the strengths of the responses due to different amplitudes of the external potentials. Furthermore, we choose the wave vector $q = 0.42$, which is the smallest nonzero wavevector allowed by the periodic boundary condition. We select q in this way because O'Hern et al. [3] showed that in the small wavevector limit, the static linear response gave appropriate effective temperatures, while for short wavelengths (larger q), the fluctuation-dissipation theorem yielded better results. We also need to point out that we do not follow exactly the same procedure as theirs. They considered time-dependent variables, created a parametric plot of correlation and susceptibility similar to figure 2.9 in the preceding subsection, and used the intercept value as the static effective temperature. In contrast, we calculate the static response by averaging over a long time after the system is at stationary state. The effective temperature defined in this way is equivalent to their case.

The results are displayed in figure 2.12. As seen in the plots, the structure factors decrease with increasing shear rate, which cannot be observed in figure 2.3 due to the large scale. The response factor $a(q_{\alpha})$ are also decaying when the shear rate is larger, while decrease in $a(q_{\alpha})$ is quicker than that in the structure factor. As a result, the effective temperatures along both directions transverse to the flow are monotonically growing with the shear rates. Moreover, the temperatures along the velocity gradient direction are higher than those along the vorticity direction, especially for $\dot{\gamma} = 20.0$. This difference has also been observed for the effective temperatures obtained from the modified fluctuation-dissipation theorem.

For a clear comparison, effective temperatures obtained from all three definitions we have discussed are plotted in figure 2.13. Although all the effective temperatures have the same trends with increasing shear rates, the values generated from the static linear response are systematically smaller than those obtained from FDT. It is not surprising. Even though sometimes the effective temperatures obtained from the static linear response are consistent with the FDT results, in many case they are different [3]. Actually Berthier et al. [13] have pointed out that due to the two time scales in the parametric plots, it may not be appropriate to define the effective temperature with $\chi(t \rightarrow 0)/C(0)$. In this respect, the effective temperature defined from the static linear response may be questionable.

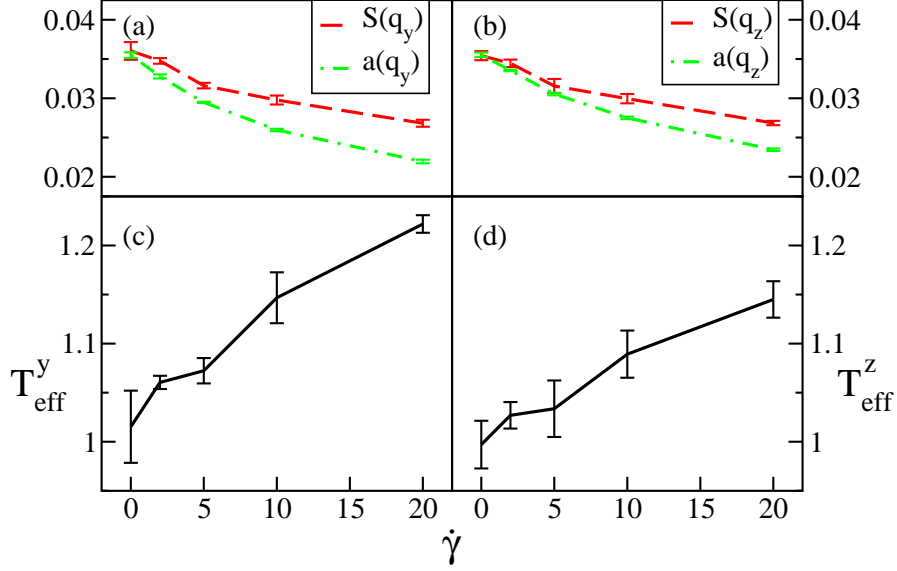


Figure 2.12: The static structure factors $S(q_\alpha)$ and the response coefficients $a(q_\alpha)$ are plotted versus the shear rate in panels (a) and (b). The smallest non-zero wave vector $q_\alpha = 0.42$ is used. The effective temperatures are depicted in panels (c) and (d). The results along the velocity gradient direction \hat{e}_y are shown in (a) and (c). The data along the vorticity direction \hat{e}_z are in panels (b) and (d).

Since the effective temperatures generated from the static linear response with the smallest wavevector due to the periodic boundary condition are different from those calculated by the modified fluctuation-dissipation theorem, we wonder if the calculations with other wavevectors could yield better results. The static structure factors of the unperturbed sheared system and the response coefficient of the system subjected to the external potential involving various wavevectors are depicted in figure 2.14. As seen from the figure, the shear-rate dependence for the $S(k_\alpha)$ are different for each fixed wavevector. The same situation can be observed for $a(k_\alpha)$. For every specific shear rate, the response coefficients seem to have similar wavevector dependence as the structure factors (see figure 2.3).

The effective temperatures for each wavevector and shear rate are then calculated and plotted in figure 2.15. As is clearly visible in the figure, the effective temperatures exhibit a complicated dependence on the wavevector. Roughly speaking, for very small shear rates (panel (a) and (b)), the effective temperatures grow with the wavevector, and the values along the velocity gradient direction are slightly larger than those in the vorticity gradient. For larger q , the effective temperatures along \hat{e}_y (panel (c)) seem to be independent of the wavevector. On the contrary, in \hat{e}_z direction, as seen in panel (d), the effective temperatures are highest around $q = 5.45$, the peak position for $S(k_\alpha)$. For the two wavevectors ($q = 5.45$ and 4.61), the

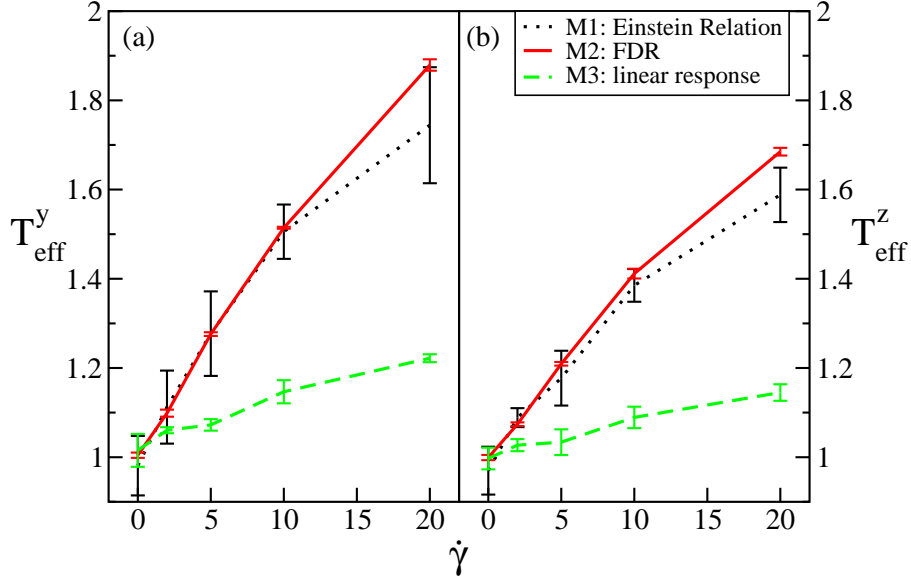


Figure 2.13: The effective temperatures calculated from the linear response relation with the smallest non-zero wave vector $q_\alpha = 0.42$ are compared with T_{eff} measured from the other two methods we discussed previously, specifically, the Einstein relation and the fluctuation-dissipation theorem. With the definition based on the FDT, the effective temperatures are extracted from the parametric plots for the wave vector $k_\alpha = 5.45$. Panel (a): along the flow-gradient direction \hat{e}_y ; panel (b): along the vorticity direction \hat{e}_z .

effective temperatures along the vorticity direction are larger. However, when the wavevector becomes even larger ($q \geq 7.55$), T_{eff} along the \hat{e}_z axis drops and is eventually smaller than that along the velocity gradient direction. So far, we do not have a good explanation for the reasons causing the complicated wavevector dependent behavior of the effective temperatures. A theoretical analysis on this subject is needed in the future.

2.4.4 Density distribution fit

Consider an equilibrium system driven by an external potential V^{ext} , which only acts on one tagged particle, the distribution $n(\mathbf{r}_1)$ of the tagged particle can be written as [2],

$$n(\mathbf{r}_1) \propto \exp[-V^{\text{ext}}(\mathbf{r}_1)/(k_B T)] . \quad (2.40)$$

Equation 2.40 is not valid for nonequilibrium situation. Recently, a nonequilibrium stationary system under steady shear was explored, and an expression was derived to describe the distribution of tagged particle subjected to an external potential which varies only along the directions transverse to the shear flow, namely,

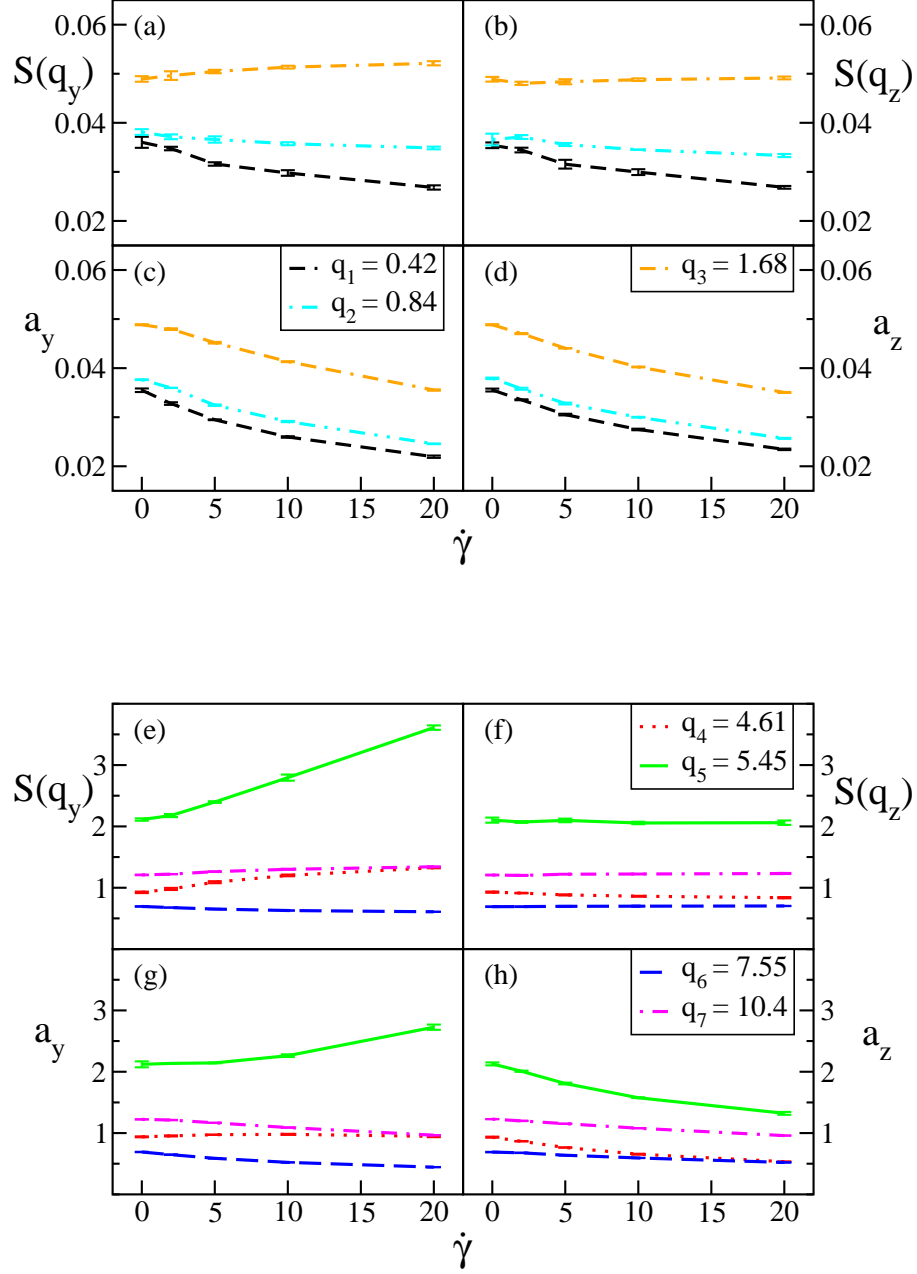


Figure 2.14: In panels (a), (b), (e) and (f), the structure factors at various wavevectors are plotted versus the shear rate. In panels (c), (d), (g) and (h), the response coefficients at various wavevectors are depicted versus the shear rate. Panels (a), (c), (e) and (g) show the data along the velocity gradient direction \hat{e}_y . Panels (b), (d), (f) and (h) illustrate the results in the vorticity direction \hat{e}_z .

the velocity gradient direction and the vorticity direction [2],

$$n_s(\alpha_1) \propto \exp \left[-V^{\text{ext}}(\alpha_1)/(k_B T_{\text{eff}}^\alpha) \right] , \quad (2.41)$$

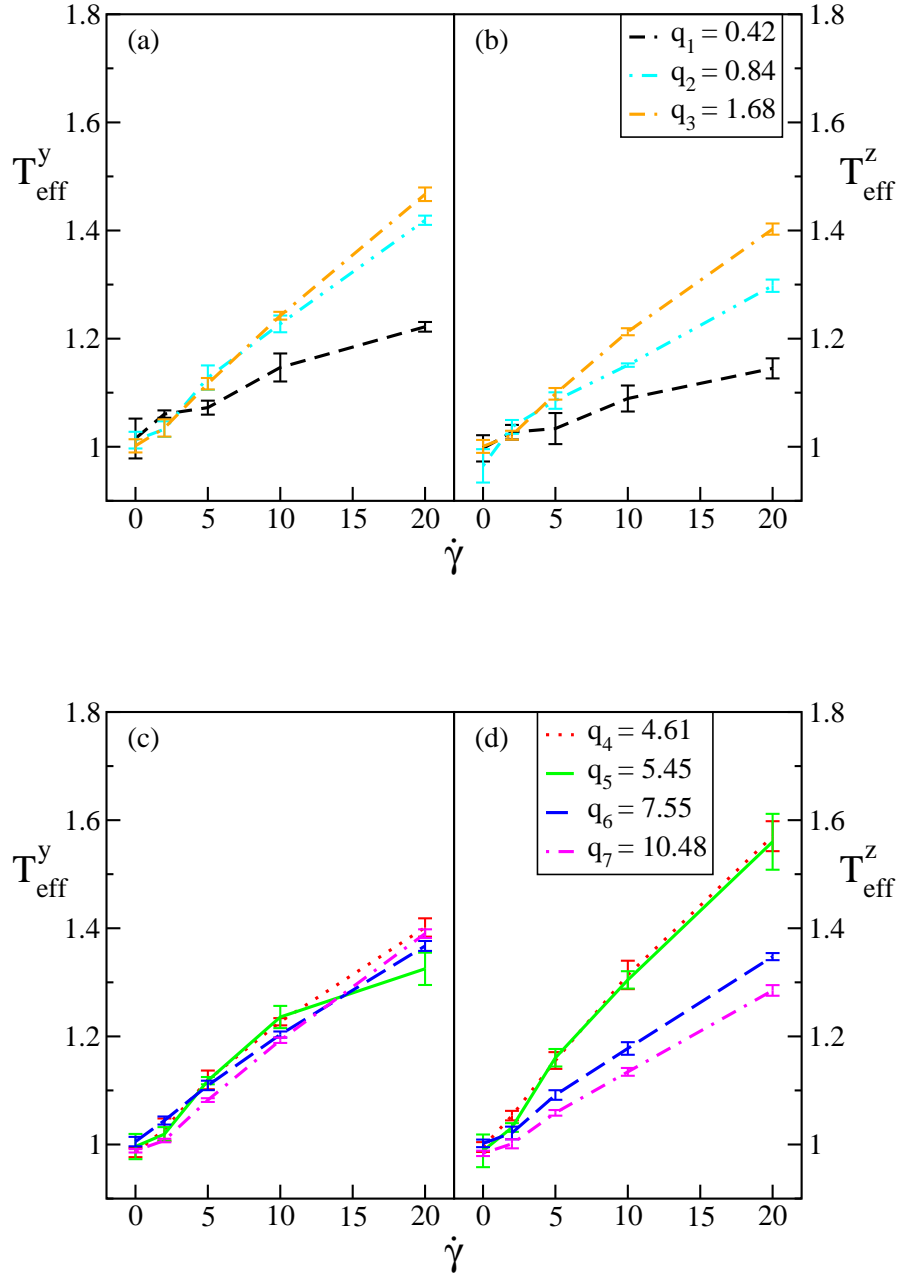


Figure 2.15: The effective temperatures obtained from the linear response function with various wavevectors are plotted versus the shear rate. Panels (a) and (b) show T_{eff} calculated with smaller wavevectors, corresponding to the panels (a)-(d) in figure 2.14. Panels (c) and (d) illustrate T_{eff} evaluated with larger wavevectors, corresponding to the panels (e)-(h) in figure 2.14. T_{eff} along the velocity gradient direction \hat{e}_y are plotted in panels (a) and (c). T_{eff} in the vorticity gradient direction \hat{e}_z are drawn in panels (b) and (d).

where $\alpha = y$ or z . Equation 2.41 has the same form as equation 2.40, but the equilibrium temperature is replaced with the effective temperature.

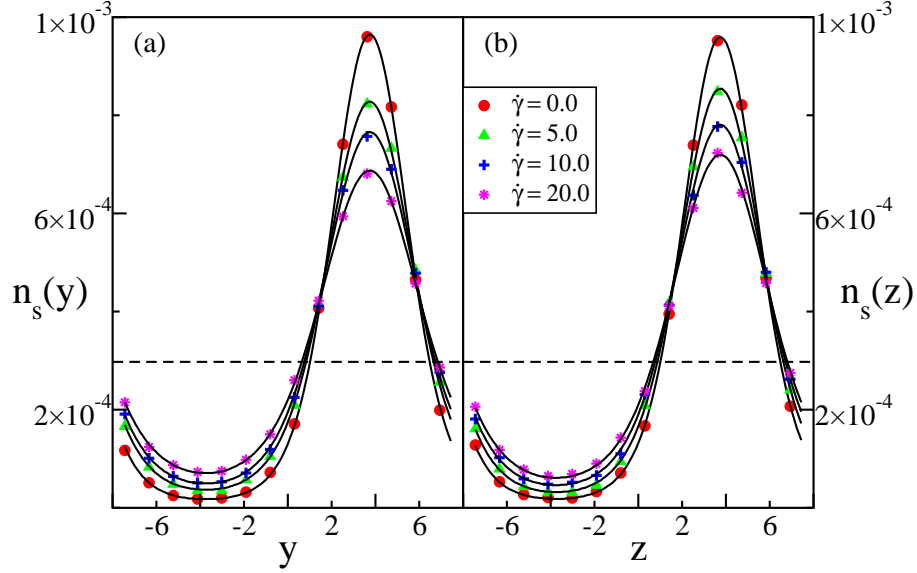


Figure 2.16: The density distributions of the tracer particle in the sheared colloidal suspension driven by external potential are plotted versus α ($\alpha = y$ or z). Panel (a): the external potential is along the velocity gradient direction; panel (b): along the vorticity direction. The solid lines are the fits to a normalized version of equation 2.41. The dashed line gives the average density of the particle without external potential.

To extract the effective temperature, we again employ a periodic-in-space external potential, with the smallest wavevector allowed by the periodic boundary conditions,

$$V^{\text{ext}}(\alpha) = V_0 \sin(2\pi\alpha/L) . \quad (2.42)$$

In this equation α is either y or z . There are two differences between present work and the one we discussed in the previous subsection. First, the amplitude used here $V_0 = 2.0$ is larger than the other one, in this case it is outside the linear response regime. Second, the external force is only exerted on one chosen particle (in practice, we randomly choose 14 particles to get better statistics), while in the previous calculation, the external potential acted on the whole system. After the simulations, the density profiles along the relevant directions are calculated and depicted in figure 2.16. The differences between the velocity gradient direction and the vorticity direction are not obvious. As the shear rate goes larger, the height of peak and the depth of valley in the distribution becomes smaller. This may be explained by the fact that the effective temperature is higher, causing that the influence of the perturbation on the system relatively decreases.

We then fit the density distributions of the tagged particles with equation 2.41 and treat T_{eff}^α as a fitting parameter. The results are displayed in figure 2.17. To make a full comparison, the effective temperatures

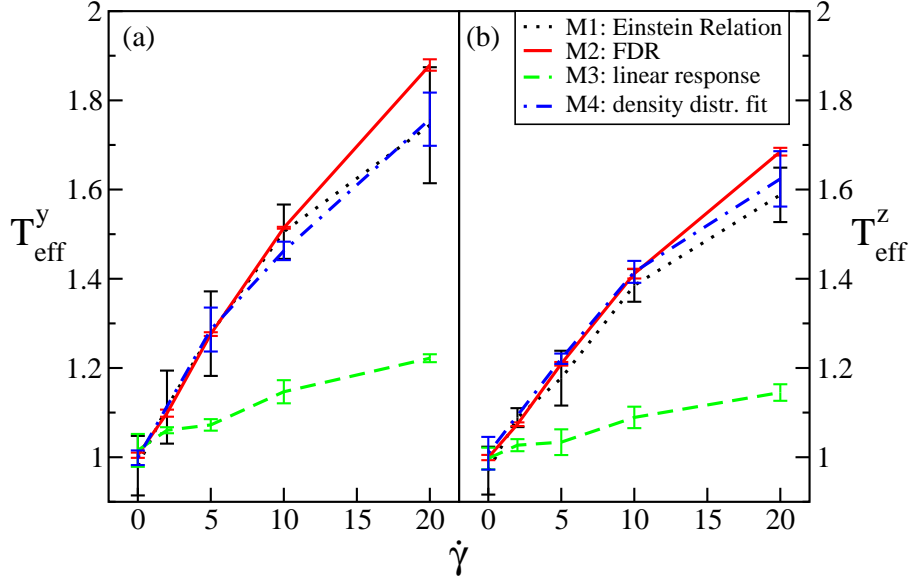


Figure 2.17: The effective temperatures calculated with four different methods are plotted versus the shear rates. For the definition based on the fluctuation-dissipation theorem, T_{eff} is calculated at the wavevector $k_\alpha = 5.45$, at which the static structure factors are maximums. For the calculation with linear response method, T_{eff} is evaluated at the smallest nonzero wavevector $q_\alpha = 0.42$. Refer to the text for the details of the definitions and calculations. Panel (a) shows the effective temperatures along the velocity gradient direction \hat{e}_y and panel (b) gives them in the vorticity gradient \hat{e}_z direction.

defined by the other three methods we discussed before are also summarized in the figure. We can see that the effective temperatures evaluated from the fitting of the density profiles are in good agreement with those calculated from the fluctuation-dissipation theorem. This result can also be regarded as evidence that the effective temperature can determine some static properties of the system, such as the tagged particle distribution under perturbation.

2.5 Discussion

In this chapter, we have investigated the static structure of the nonequilibrium liquid subjected to shear. The strong anisotropy in the highly sheared system has been observed. In addition, we also found that the system exhibited shear thinning in the whole range of the shear rates we explored.

Most of our efforts were devoted to studying the notion of effective temperature in the nonequilibrium stationary colloidal suspension driven by a steady shear characterized by the shear rate. We used four different methods to define and to calculate the effective temperatures. The first two are based on the

fluctuation-dissipation theorem. Specifically, we first used the modified Einstein relation to yield the effective temperature. For the second method, the self-intermediate scattering function and its corresponding susceptibility were employed. Four different wavevectors were chosen to calculate them. The effective temperatures were then evaluated from the parametric plots, and showed no wavevector dependence. This result has also been reported by Berthier et al. [13]. Furthermore, the effective temperature calculated from the self-intermediate scattering function is consistent with that generated from the Einstein relation. Our result supports the viewpoint of Berthier et al. [13], for stationary states the effective temperatures generated from the extended fluctuation-dissipation theorem do not depend on the observables.

The last two sets of effective temperatures were calculated from the static variables. Specifically, for the third approach, we imposed on the system a weak, static, periodic-in-space external potential, involving the smallest wavevector allowed by the periodic boundary condition, and generated the effective temperatures from the variation in the collective density with the linear response approximation. It was found that this method yielded different effective temperatures from the other approaches. We then extended the calculations to other wavevectors and saw that the effective temperatures exhibited very complicated dependence on both the wavevectors and the directions. On the other hand, for the last definition of the effective temperature, a similar external potential with larger amplitude (outside the linear response regime) was introduced on only one tagged particle (in the actual simulation 14 particles were selected to get better statistics). The effective temperature was evaluated by fitting the tracer particle distribution. The results agreed with those calculated from the generalized fluctuation-dissipation relation very well. All the effective temperatures based on various definitions are summarized in figure 2.17.

By considering the fact that our system is strongly anisotropic under high shear, for each method we calculated the effective temperatures along the two directions perpendicular to the shear flow, namely, the velocity gradient direction and the vorticity direction. As seen clearly in figure 2.17, all the effective temperatures along \hat{e}_y axis are somewhat higher than those along \hat{e}_z direction (in the last two definitions, the smallest wavevector was used).

To summarize this chapter, we want to indicate that three points need to be considered regarding the effective temperatures. First of all, the strongly anisotropic systems need to be investigated. Before most emphasis was laid on glassy systems or supercooled liquids. Those systems are still quite isotropic and the direction dependence of the effective temperature cannot be noticed. Moreover, the realistic meaning of the anisotropic temperature needs to be studied theoretically. The second question has been posed by O'Hern et al. [3]: in what situation can the static linear response be used to calculate the effective temperatures? Third, the applications of the effective temperatures are necessary to be studied. Our results about the density profile of the tagged particle subjected to an external potential imply that the effective temperature can

determine the particle distribution even outside the linear response regime. Besides, as we have mentioned at the beginning of this chapter, the effective temperatures have been successfully employed to explain some phenomena in physics, chemistry, and even biology [19, 20, 21]. However, a universal relation between the effective temperature and many other physical quantities is still missing in the nonequilibrium situation.

Bibliography

- [1] M. Zhang and G. Szamel, *Phys. Rev. E* 83, 061407 (2011).
- [2] G. Szamel and M. Zhang, *EPL*, 96, 50007 (2011).
- [3] C. S. O'Hern, A. J. Liu, and S. R. Nagel, *Phys. Rev. Lett.* 93, 165702 (2004).
- [4] L. F. Cugliandolo and J. Kurchan, *Phys. Rev. Lett.* 71, 173 (1993).
- [5] L. F. Cugliandolo, J. Kurchan, and L. Peliti, *Phys. Rev. E* 55, 3898 (1997).
- [6] T. S. Grigera and N. E. Israeloff, *Phys. Rev. Lett.* 83, 5038 (1999).
- [7] A. Puglisi, A. Baldassarri, and V. Loreto, *Phys. Rev. E* 66, 061305 (2002).
- [8] B. Abou and F. Gallet, *Phys. Rev. Lett.* 93, 160603 (2004).
- [9] H. A. Makse and J. Kurchan, *Nature (London)* 415, 614 (2002).
- [10] J. Kurchan, *Nature* 433, 222 (2005).
- [11] J.-L. Barrat and L. Berthier, *Phys. Rev. E*, 63, 012503 (2000).
- [12] L. Berthier, J.-L. Barrat, and J. Kurchan, *Phys. Rev. E* 61, 5464 (2000).
- [13] L. Berthier and J.-L. Barrat, *J. Chem. Phys.* 116, 6228 (2002).
- [14] W. Kob and H. C. Andersen, *Phys. Rev. E* 51, 4626 (1995).
- [15] I. K. Ono, C. S. O'Hern, D. J. Durian, S. A. Langer, A. J. Liu, and S. R. Nagel, *Phys. Rev. Lett.* 89, 095703 (2002).
- [16] K. Hayashi and S. Sasa, *Phys. Rev. E* 69, 066119 (2004).
- [17] K. Hayashi and S. Sasa, *Phys. Rev. E* 71, 046143 (2005).
- [18] K. Hayashi and M. Takano, *Phys. Rev. E* 76, 050104(R) (2007).
- [19] T. K. Haxton and A. J. Liu, *Phys. Rev. Lett.* 99, 195701 (2007).
- [20] P. Ilg and J.-L. Barrat, *EPL*, 79, 26001 (2007).
- [21] T. Lu, J. Hastly, and P. G. Wolynes, *Biophys. J.* 91, 84 (2006).
- [22] L. F. Cugliandolo, *J. Phys. A: Math. Theor.* 44, 483001 (2011).

- [23] S. Hess and H. J. M. Hanley, *Phys. Rev. A* *25*, 1801 (1982).
- [24] S. Hess, *International Journal of Thermophysics*, *23*, 905 (2002).
- [25] G. Szamel, *J. Chem. Phys.* *114*, 8708 (2001).
- [26] J. -P Hansen and I. R. McDonald, *Theory of Simple Liquids (2nd edition)*.
- [27] S. R. Rastogi, N. J. Wagner, and S. R. Lustig, *J. Chem. Phys.* *104*, 9234 (1996).
- [28] M. P. Allen and D. J. Tildesley, *Computer Simulation of Liquids (Oxford University Press, New York, 1987)*.
- [29] A. Iniesta and J. G. de la Torre, *J. Chem. Phys.* *92*, 2015 (1990).
- [30] D. M. Heyes and A. C. Brańka, *Molecular Phys.* *98*, 1949 (2000).
- [31] J. -P Hansen and I. R. McDonald, *Theory of Simple Liquids (2nd edition)*, page 198.
- [32] L. Berthier, *Phys. Rev. Lett.* *98*, 220601 (2007).
- [33] H. Touba, and G. A. Mansoori, *International Journal of Thermophysics*, *18*, 1217 (1997).
- [34] H. J. M. Hanley, J. C. Rainwater, and S. Hess, *Phys. Rev. A* *36*, 1795 (1987).
- [35] S. Hess and W. Loose, *Ber. Bunsenges. Phys. Chem.* *94*, 216 (1990).
- [36] H.-C. Tseng, J.-S. Wu, and R.-Y. Chang, *J. Chem. Phys.* *130*, 164515 (2009).
- [37] J. Delhommelle, *Eur. Phys. J. E.* *15*, 65 (2004).
- [38] W. Xue and G. S. Grest, *Phys. Rev. A* *40*, 1709 (1989).
- [39] T. Weider, U. Stottut, W. Loose and S. Hess, *Phys. A* *174*, 1 (1991).
- [40] N. Pottier and A. Mauger, *Phys. A* *332*, 15 (2004).
- [41] G. Szamel, J. Blawdziewicz, and J. A. Leegwater, *Phys. Rev. A* *45*, R2173 (1992).
- [42] X. Qiu, H. D. Ou-Yang, D. J. Pine, and P. M. Chaikin, *Phys. Rev. Lett.* *61*, 2554 (1988).
- [43] A. Indrani and S. Ramaswamy, *Phys. Rev. E* *52*, 6492 (1995).
- [44] B. Lander, U. Seifert, and T. Speck, *EPL*, *92*, 58001 (2011).
- [45] A. Crisanti and F. Ritort, *J. Phys. A: Math. Gen.* *36*, R181 (2003).

Appendix

In this appendix, we show how to calculate the effective temperature via the method proposed by Berthier [32]. In our system, we employ the pairwise additive, repulsive screened Coulomb potential introduced by Rastogi et al. [27],

$$V(r) = A \frac{\exp[-\kappa(r - \sigma)]}{r}, \quad (2.43)$$

to calculate inter-particle force,

$$\mathbf{F}(\mathbf{r}) = -\nabla V(r) = \left(\frac{A}{r^3} + \frac{A\kappa}{r^2} \right) \exp[-\kappa(r - \sigma)] (x\hat{\mathbf{e}}_x + y\hat{\mathbf{e}}_y + z\hat{\mathbf{e}}_z). \quad (2.44)$$

In the above two equations, the parameters A and κ have been defined in the simulation part.

Without an external force, the motion of any particles in the sheared liquid can be expressed by the Langevin equation,

$$\dot{\mathbf{r}}_i = \frac{1}{\xi_0} \sum_{j \neq i} \mathbf{F}(|\mathbf{r}_i(t) - \mathbf{r}_j(t)|) + \eta_i(t) + \dot{\gamma} y_i(t) \hat{\mathbf{e}}_x. \quad (2.45)$$

Now a small external field is exerted on the system along y direction. The perturbation is coupled to the observable B with an amplitude h ,

$$\delta H = -hB(t) = -2h \sum_i \epsilon_i \cos[k_y y_i(t)] \hat{\mathbf{e}}_y, \quad (2.46)$$

where $\epsilon_i = -1, 0, 1$ (with $\sum_i \epsilon_j = 0$) determines which particle is subjected by the external force and also controls the direction of the drive. The external force is then calculated,

$$\mathbf{F}^{\text{ext}} = -\frac{d(\delta H)}{dy} \hat{\mathbf{e}}_y = -2hk_y \sum_i \epsilon_i \sin[k_y y_i(t)] \hat{\mathbf{e}}_y. \quad (2.47)$$

The motion of particle i subjected to an external force can be expressed by,

$$\dot{\mathbf{r}}_i = \frac{1}{\xi_0} \sum_{j \neq i} \mathbf{F}(|\mathbf{r}_i(t) - \mathbf{r}_j(t)|) + \eta_i(t) + \dot{\gamma} y_i(t) \hat{\mathbf{e}}_x - 2hk_y \epsilon_i \sin[k_y y_i(t)] \hat{\mathbf{e}}_y. \quad (2.48)$$

Our objective is to generate the effective temperature with an unperturbed trajectory, and to calculate the susceptibility and the self-intermediate scattering function at the same time. To achieve this goal, we need to introduce a quantity ϕ which is defined as [32],

$$\phi_i \equiv \partial \mathbf{r}_i / \partial h. \quad (2.49)$$

Then we have,

$$\dot{\phi}_i \equiv \partial \mathbf{r}_i / \partial h . \quad (2.50)$$

Since the random noise $\eta_i(t)$ in equation 2.48 is independent of $\mathbf{r}(t)$, performing the derivative with respect to h of equation 2.48 and letting $\xi_0 = 1$, $\mathbf{F}_i = \sum_{j \neq i}^N \mathbf{F}(|\mathbf{r}_i(t) - \mathbf{r}_j(t)|)$, we get,

$$\dot{\phi}_i = \frac{\partial \mathbf{F}_i}{\partial h} + \dot{\gamma} \phi_{i,y} \hat{\mathbf{e}}_x - 2k_y \epsilon_i \sin[k_y y_i(t)] \hat{\mathbf{e}}_y . \quad (2.51)$$

To solve equation 2.51, a crucial step is to calculate $\partial \mathbf{F}_i / \partial h$. Here we use the relation $\mathbf{F}_i = -\sum_{j \neq i}^N \mathbf{F}_{ji}(|\mathbf{r}_j - \mathbf{r}_i|)$.

$$\begin{aligned} \frac{\partial \mathbf{F}_i}{\partial h} &= \frac{\partial \mathbf{F}_i}{\partial \mathbf{r}_i} \cdot \frac{\partial \mathbf{r}_i}{\partial h} + \sum_{j \neq i}^N \frac{\partial \mathbf{F}_i}{\partial \mathbf{r}_j} \cdot \frac{\partial \mathbf{r}_j}{\partial h} \\ &= \frac{-\partial \sum_{j \neq i}^N \mathbf{F}_{ji}}{\partial \mathbf{r}_i} \phi_i + \sum_{j \neq i}^N \frac{-\partial \sum_{j \neq i}^N \mathbf{F}_{ji}}{\partial \mathbf{r}_j} \phi_j \\ &= -\sum_{j \neq i}^N \frac{\partial \mathbf{F}_{ji}}{\partial \mathbf{r}_i} \phi_i - \sum_{j \neq i}^N \frac{\partial \mathbf{F}_{ji}}{\partial \mathbf{r}_j} \phi_j \\ &= -\sum_{j \neq i}^N \frac{\partial \mathbf{F}_{ji}}{\partial \mathbf{r}_j} (\phi_j - \phi_i) \end{aligned} \quad (2.52)$$

From the third line to the fourth line in the equations above, we used $\partial \mathbf{F}_{ji} / \partial \mathbf{r}_i = -\partial \mathbf{F}_{ji} / \partial \mathbf{r}_j$.

Now let us continue to calculate $\partial \mathbf{F}_{ji} / \partial \mathbf{r}_j$, which is a tensor,

$$\frac{\partial \mathbf{F}_{ji}}{\partial \mathbf{r}_j} = \begin{pmatrix} \frac{\partial F_{ji,x}}{\partial r_{j,x}} & \frac{\partial F_{ji,x}}{\partial r_{j,y}} & \frac{\partial F_{ji,x}}{\partial r_{j,z}} \\ \frac{\partial F_{ji,y}}{\partial r_{j,x}} & \frac{\partial F_{ji,y}}{\partial r_{j,y}} & \frac{\partial F_{ji,y}}{\partial r_{j,z}} \\ \frac{\partial F_{ji,z}}{\partial r_{j,x}} & \frac{\partial F_{ji,z}}{\partial r_{j,y}} & \frac{\partial F_{ji,z}}{\partial r_{j,z}} \end{pmatrix} . \quad (2.53)$$

With this tensor, $\frac{\partial \mathbf{F}_{ji}}{\partial \mathbf{r}_j} \cdot (\phi_j - \phi_i)$ in equation 2.52 can be expressed as,

$$\frac{\partial \mathbf{F}_{ji}}{\partial \mathbf{r}_j} \cdot (\phi_j - \phi_i) = \begin{pmatrix} \frac{\partial F_{ji,x}}{\partial r_{j,x}} & \frac{\partial F_{ji,x}}{\partial r_{j,y}} & \frac{\partial F_{ji,x}}{\partial r_{j,z}} \\ \frac{\partial F_{ji,y}}{\partial r_{j,x}} & \frac{\partial F_{ji,y}}{\partial r_{j,y}} & \frac{\partial F_{ji,y}}{\partial r_{j,z}} \\ \frac{\partial F_{ji,z}}{\partial r_{j,x}} & \frac{\partial F_{ji,z}}{\partial r_{j,y}} & \frac{\partial F_{ji,z}}{\partial r_{j,z}} \end{pmatrix} \begin{pmatrix} \phi_{j,x} - \phi_{i,x} \\ \phi_{j,y} - \phi_{i,y} \\ \phi_{j,z} - \phi_{i,z} \end{pmatrix} . \quad (2.54)$$

Take equation 2.54 into equation 2.52 and expand the tensor.

$$\begin{aligned}
\frac{\partial \mathbf{F}_i}{\partial h} &= - \sum_{j \neq i}^N \frac{\partial \mathbf{F}^{ji}}{\partial \mathbf{r}_j} (\phi_j - \phi_i) \\
&= - \sum_{j \neq i}^N \left[\frac{\partial F^{ji,x}}{\partial r_{j,x}} (\phi_{j,x} - \phi_{i,x}) + \frac{\partial F^{ji,x}}{\partial r_{j,y}} (\phi_{j,y} - \phi_{i,y}) + \frac{\partial F^{ji,x}}{\partial r_{j,z}} (\phi_{j,z} - \phi_{i,z}) \right] \hat{\mathbf{e}}_x \\
&\quad - \sum_{j \neq i}^N \left[\frac{\partial F^{ji,y}}{\partial r_{j,x}} (\phi_{j,x} - \phi_{i,x}) + \frac{\partial F^{ji,y}}{\partial r_{j,y}} (\phi_{j,y} - \phi_{i,y}) + \frac{\partial F^{ji,y}}{\partial r_{j,z}} (\phi_{j,z} - \phi_{i,z}) \right] \hat{\mathbf{e}}_y \\
&\quad - \sum_{j \neq i}^N \left[\frac{\partial F^{ji,z}}{\partial r_{j,x}} (\phi_{j,x} - \phi_{i,x}) + \frac{\partial F^{ji,z}}{\partial r_{j,y}} (\phi_{j,y} - \phi_{i,y}) + \frac{\partial F^{ji,z}}{\partial r_{j,z}} (\phi_{j,z} - \phi_{i,z}) \right] \hat{\mathbf{e}}_z
\end{aligned} \tag{2.55}$$

Now put equation 2.55 back into equation 2.51, $\dot{\phi}$ along each direction can be calculated respectively,

$$\dot{\phi}_{i,x} = - \sum_{j \neq i}^N \left[\frac{\partial F^{ji,x}}{\partial r_{j,x}} (\phi_{j,x} - \phi_{i,x}) + \frac{\partial F^{ji,x}}{\partial r_{j,y}} (\phi_{j,y} - \phi_{i,y}) + \frac{\partial F^{ji,x}}{\partial r_{j,z}} (\phi_{j,z} - \phi_{i,z}) \right] + \dot{\gamma} \phi_{i,y}, \tag{2.56}$$

$$\begin{aligned}
\dot{\phi}_{i,y} &= - \sum_{j \neq i}^N \left[\frac{\partial F^{ji,y}}{\partial r_{j,x}} (\phi_{j,x} - \phi_{i,x}) + \frac{\partial F^{ji,y}}{\partial r_{j,y}} (\phi_{j,y} - \phi_{i,y}) + \frac{\partial F^{ji,y}}{\partial r_{j,z}} (\phi_{j,z} - \phi_{i,z}) \right] \\
&\quad - 2k_y \epsilon_i \sin[k_y r_{i,y}(t)],
\end{aligned} \tag{2.57}$$

$$\dot{\phi}_{i,z} = - \sum_{j \neq i}^N \left[\frac{\partial F^{ji,z}}{\partial r_{j,x}} (\phi_{j,x} - \phi_{i,x}) + \frac{\partial F^{ji,z}}{\partial r_{j,y}} (\phi_{j,y} - \phi_{i,y}) + \frac{\partial F^{ji,z}}{\partial r_{j,z}} (\phi_{j,z} - \phi_{i,z}) \right]. \tag{2.58}$$

To calculate $\dot{\phi}$ along all the directions from equations 2.56 to 2.58, we need to calculate $\partial F_{ji,\alpha} / \partial r_{j,\alpha}$ and $\partial F_{ji,\alpha} / \partial r_{j,\beta}$ ($\alpha, \beta = x, y, z$, $\alpha \neq \beta$). The calculations are straightforward by taking derivative of equation 2.44.

$$\begin{aligned}
\frac{\partial F_{ji,\alpha}}{\partial r_{j,\alpha}} &= \frac{\partial}{\partial r_{j,\alpha}} \left\{ \left(\frac{A}{r_{ji}^3} + \frac{A\kappa}{r_{ji}^2} \right) \exp[-\kappa(r_{ji} - \sigma)] (r_{j,\alpha} - r_{i,\alpha}) \right\} \\
&= \left(\frac{A}{r_{ji}^3} + \frac{A\kappa}{r_{ji}^2} \right) \exp[-\kappa(r_{ji} - \sigma)] \\
&\quad + \left(\frac{A}{r_{ji}^3} + \frac{A\kappa}{r_{ji}^2} \right) (r_{j,\alpha} - r_{i,\alpha}) (-\kappa) \exp[-\kappa(r_{ji} - \sigma)] \frac{r_{j,\alpha} - r_{i,\alpha}}{r_{ji}} \\
&\quad + \exp[-\kappa(r_{ji} - \sigma)] (r_{j,\alpha} - r_{i,\alpha}) \left(-\frac{3A}{r_{ji}^4} - \frac{2A\kappa}{r_{ji}^3} \right) \frac{r_{j,\alpha} - r_{i,\alpha}}{r_{ji}}
\end{aligned} \tag{2.59}$$

$$\begin{aligned}
\frac{\partial F_{ji,\alpha}}{\partial r_{j,\beta}} &= \frac{\partial}{\partial r_{j,\beta}} \left\{ \left(\frac{A}{r_{ji}^3} + \frac{A\kappa}{r_{ji}^2} \right) \exp[-\kappa(r_{ji} - \sigma)](r_{j,\alpha} - r_{i,\alpha}) \right\} \\
&= \left(\frac{A}{r_{ji}^3} + \frac{A\kappa}{r_{ji}^2} \right) (r_{j,\alpha} - r_{i,\alpha})(-\kappa) \exp[-\kappa(r_{ji} - \sigma)] \frac{r_{j,\beta} - r_{i,\beta}}{r_{ji}} \\
&+ \exp[-\kappa(r_{ji} - \sigma)](r_{j,\alpha} - r_{i,\alpha}) \left(-\frac{3A}{r_{ji}^4} - \frac{2A\kappa}{r_{ji}^3} \right) \frac{r_{j,\beta} - r_{i,\beta}}{r_{ji}}
\end{aligned} \tag{2.60}$$

To simplify the calculations, in the simulation we saved and updated these values $ds = r_{ji}$, $r_\alpha = r_{j,\alpha} - r_{i,\alpha}$, $ex = \exp[-\kappa(ds - \sigma)]$, $f_{ji} = A(1/ds^3 + \kappa/ds^2)ex$ and $p_3 = A(-3/ds^5 - 2\kappa/ds^4)ex$, then equation 2.59 and 2.60 can be written in a easier way.

$$\frac{\partial F_{ji,\alpha}}{\partial r_{j,\alpha}} = f_{ji} - f_{ji}\kappa \frac{r_\alpha^2}{ds} - p_3 r_\alpha^2 \tag{2.61}$$

$$\frac{\partial F_{ji,\alpha}}{\partial r_{j,\beta}} = -f_{ji}\kappa \frac{r_\alpha r_\beta}{ds} - p_3 r_\alpha r_\beta \tag{2.62}$$

Finally, in the simulation, ϕ can be evaluated from equations 2.56, 2.57 and 2.58.

Now let us consider the susceptibility $\chi_s(k; t)$. We simply copy equation 2.32 here,

$$\chi_s(k; t) = \frac{\partial}{\partial h} \left\langle \frac{1}{N'} \sum_{j=1}^N \epsilon_j \exp[i\mathbf{k} \cdot \mathbf{r}_j(t)] \right\rangle_{h \rightarrow 0} \cdot \tag{2.63}$$

Take derivative before doing the average [32] and use $\phi_j = \partial \mathbf{r}_j / \partial h$, we get,

$$\chi_s(k; t) = \frac{1}{N'} \left\langle \sum_j^N \frac{\partial \epsilon_j \exp[i\mathbf{k} \cdot \mathbf{r}_j(t)]}{\partial \mathbf{r}_j} \cdot \phi_j \right\rangle_0 \cdot \tag{2.64}$$

Given the external force is along $\hat{\mathbf{e}}_y$ direction, then we can calculate the susceptibility by,

$$\chi_s(k_y; t) = \frac{1}{N'} \left\langle \sum_{j=1}^N \epsilon_j k_y \sin(k_y y_j) \phi_{j,y} \right\rangle_0 \cdot \tag{2.65}$$

A similar procedure can be used for the external force along the vorticity direction.

Chapter 3

Supercooled liquids and glasses under shear

3.1 Introduction

About twenty years ago, Kob and Andersen proposed a model, namely, binary (80:20) Lennard-Jones mixture to investigate supercooled liquids [1, 2]. They modified the parameters in the Lennard-Jones potential, as a result it is similar to the potential devised by Weber and Stillinger [3], describing the Ni₈₀P₂₀ alloy system. Kob and Andersen simulated the system using molecular dynamics and investigated its dynamic properties [1, 2]. They found that both the diffusion coefficient D and the structural relaxation time τ are dependent on the temperature T . They fitted D and τ via the power law equations predicted by the mode coupling theory (MCT),

$$D \propto (T - T_c)^\gamma, \quad (3.1)$$

$$\tau \propto (T - T_c)^{-\gamma}, \quad (3.2)$$

where T_c is so called mode coupling temperature, which is usually accepted as $T_c = 0.435$ for this KA binary LJ system. The exponent γ is a parameter, and does not have any relation with the shear rate. The values of γ in equation 3.1 and 3.2 are different for supercooled liquids, so $D\tau$ is not independent of T , in other words, the Stokes-Einstein relation is violated. The breakdown of Stokes-Einstein relation is considered as a manifestation of dynamic heterogeneity in supercooled liquids [4, 5, 6, 7].

Extensive computer simulations have been performed on the Kob-Andersen binary Lennard-Jones mixture since it was proposed. Szamel and Flenner have studied this system with a large scale Brownian dynamics simulations [8, 9]. Although the mean square displacement and self-intermediate scattering function were not exactly the same as those calculated by the molecular dynamics, a similar power law behavior for D and τ was reported with slightly different γ values. Remarkably, they pointed out that the critical temperature

T_c was actually not necessary to be 0.435, but depended on the range to fit. By extending to even lower temperatures than those discussed by Kob and Andersen [1, 2], they found the deviations from the power law when the temperature is in the vicinity of $T_c = 0.435$. They also studied dynamic heterogeneity of the system as it approached the glass transition.

Varnik and coworkers simulated the supercooled system composed with the Kob-Andersen binary Lennard-Jones particles under various shear rates and temperatures by the molecular dynamics method. With shear the much lower temperatures below T_c can be reached. They investigated the dynamic behavior, such as, the diffusion and structural relaxation [10, 11]. Interestingly, they found that in the supercooled state ($T > T_c$), only when the shear rate $\dot{\gamma}$ was larger than a threshold value, the dynamic properties showed an obvious dependence on the shear rate, otherwise they were controlled by thermal fluctuations and the system was equilibrium. On the other hand, for the glass ($T < T_c$), the dynamics was always dominated by the shear even with the smallest γ they studied.

In this chapter, we use Brownian dynamics simulation to investigate the Kob-Andersen binary Lennard-Jones mixture [1] at various temperatures, ranging from the supercooled region to the glassy state. At each temperature, a small steady shear flow is imposed on the system along x axis, and the velocity gradient is along y direction. The aim of this work is to study the structural and dynamic behavior of the system under shear. By comparison with the systems without shear [1, 2, 8, 9, 12, 13], the influence caused by shear can be checked. To study the combined effects of the bath temperature and the shear on dynamics of the system, we propose three definitions of the so called ‘effective temperature’. The first and second effective temperatures are estimated by the extended MCT. The third definition is built upon the Stokes-Einstein relation.

This chapter is organized as following. The simulation details are described in section 2. In section 3, the static structure is studied by calculating the pair correlation function and the static structure factors $S(\mathbf{k})$. Dynamic behavior of the system is analyzed in chapter 4, where the mean square displacement and the intermediate scattering function are calculated. Moreover, we propose new methods to evaluate the effective temperature of the sheared liquid. Section 5 is devoted to a summary and discussion of the results.

3.2 Simulations

The two types of particles A and B in the binary Lennard-Jones system have the same mass. The total number of particles is $N = 1000$, and the ratio between numbers of particle A and B is 80:20. The interaction

between any two of particles i and j ($i, j \in \{A, B\}$) in the system is given by Lennard-Jones potential,

$$V_{ij} = 4\epsilon_{ij}[(\sigma_{ij}/r)^{12} - (\sigma_{ij}/r)^6] . \quad (3.3)$$

The parameters in the equation are shown in Table 3.1. All the physical quantities will be measured in

Table 3.1: Parameters of the binary Lennard-Jones system

particle pair	A-A	B-B	A-B
σ	1.0	0.88	0.8
ϵ	1.0	0.5	1.5

reduced units, which are listed in Table 3.2. Both the Boltzmann constant k_B and the friction coefficient ξ_0 are set equal to 1.0 in our simulation. The potential is truncated and shifted at $r = 2.5\sigma_{ij}$ for computational

Table 3.2: Reduced units of physical quantities in the binary Lennard-Jones system

physical quantities	length	energy	temperature	time
in units of	σ_{AA}	ϵ_{AA}	ϵ_{AA}/k_B	$\sigma_{AA}^2 \xi_0 / \epsilon_{AA}$

efficiency. The interparticle force between any two particles can be obtained,

$$\mathbf{F}_{ij} = -\nabla V_{ij} . \quad (3.4)$$

For a Brownian particle i which interacts with its neighbors through the pairwise-addictive forces, the equation of motion can be written down as,

$$\dot{\mathbf{r}}_i = -\frac{1}{\xi_0} \sum_{j \neq i} \mathbf{F}_{ij}(|\mathbf{r}_i(t) - \mathbf{r}_j(t)|) + \eta_i(t) + \dot{\gamma} y_i(t) \hat{\mathbf{e}}_x , \quad (3.5)$$

where $\dot{\gamma}$ is the shear rate, $y_i(t)$ is the y-component of position \mathbf{r}_i of particle i , \mathbf{e}_x is the unit vector along x direction. The random noise satisfies the fluctuation-dissipation theorem,

$$\langle \eta_i(t) \eta_j(t') \rangle = 2D_0 \delta(t - t') \delta_{ij} I . \quad (3.6)$$

In the above equation, I is the unit tensor, and D_0 is the diffusion coefficient which can be written in the Einstein's expression [14],

$$D_0 = \frac{k_B T}{\xi_0}, \quad (3.7)$$

where T is the temperature. In this work the systems are investigated under different temperatures, which are $T = 0.6, 0.55, 0.5, 0.47, 0.4, 0.2, 0.1, 0.01, 0.0$, respectively. With each temperature, a small shear ($\dot{\gamma} = 0.01$) is imposed on the systems. In the simulations periodic boundary conditions are applied. At the very beginning $t = 0$ the simulation box is cubic whose length is $9.4\sigma_{AA}$. The time step of the simulation is 5×10^{-5} . First the systems with each temperature and shear need to be equilibrated long enough to make sure that the systems have entered into the steady state. In this case, time translational invariance (TTI) is well satisfied and the time correlation functions can be calculated by averaging over all the possible time origin. After that trajectories of all particles are saved every 100 to 800 steps, then the static and dynamic quantities of the systems are calculated with those trajectories. The simulation time is about 200 times longer than the structural relaxation time to make certain that the statistics of the calculated values is good enough.

3.3 Static structure of the binary Lennard-Jones system under shear

In this section, we focus attention on the static features of the binary Lennard-Jones system under small shear, which can be researched by exploring the isotropic component of the pair distribution function $g(r)$, the xy component of the $g(\mathbf{r})$, and the static structure factor $S(k)$.

3.3.1 Pair distribution function

The pair distribution function is calculated with the formula,

$$g_{\mu\nu}(\mathbf{r}) = \frac{V}{N_\mu N_\nu} \left\langle \sum_i^N \sum_{j \neq i}^N \delta(\mathbf{r} - \mathbf{r}_{i,\mu} + \mathbf{r}_{j,\nu}) \right\rangle. \quad (3.8)$$

μ, ν denote particle component A and B . The pair distribution functions g_{AA} , g_{AB} , and g_{BB} for the KA binary LJ system are drawn in Figure 3.1.

We carefully compare $g_{AA}(r)$, $g_{AB}(r)$ and $g_{BB}(r)$ at temperatures $T = 0.5, 0.55, 0.6$ with those reported by Kob and Andersen [1]. They agree with each other very well, which implies that the effect of shear ($\dot{\gamma} = 0.01$) on the structure of supercooled liquid can be neglected. Figure 3.1 illustrates that the effect of

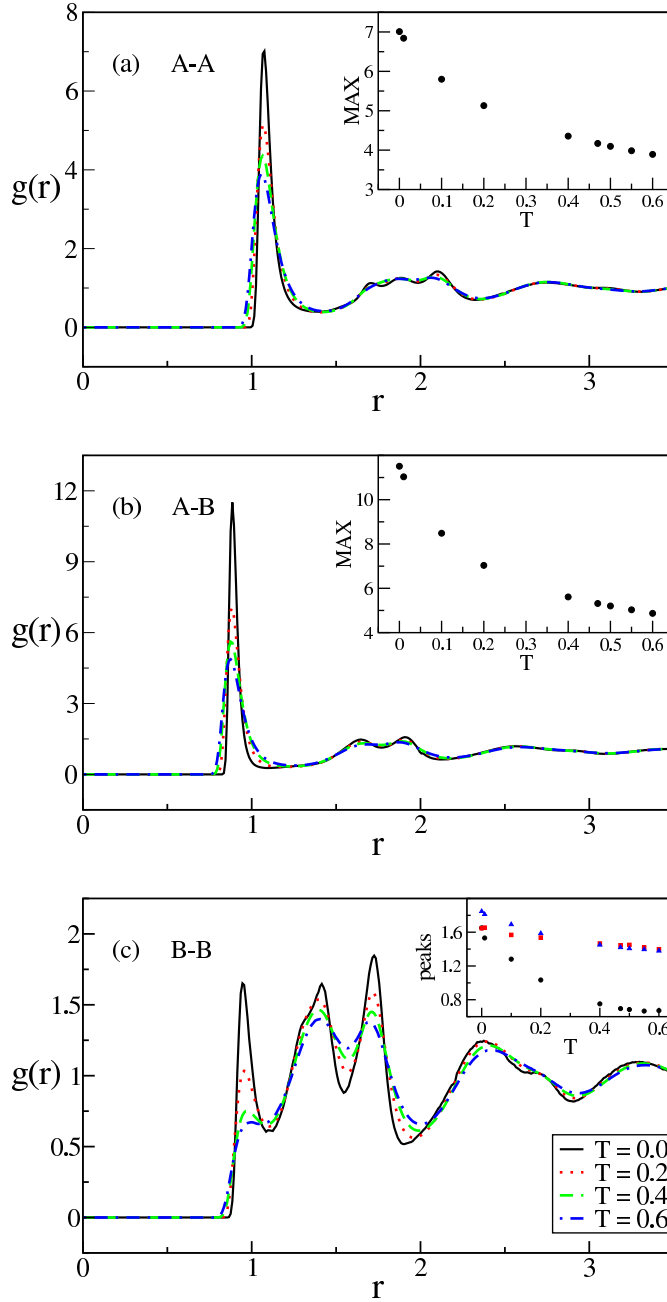


Figure 3.1: The pair distribution function of the binary Lennard-Jones particles with various temperatures, and imposed with shear $\dot{\gamma} = 0.01$. Notice that the ranges of g_{AB} , g_{AA} and g_{BB} are different, so the three panels are scaled in different ways to make the figures clear to see. The insert figure in (a) gives the maximum value of $g_{AA}(r)$ versus the temperature T . The insert figure in (b) shows the maximum value of $g_{AB}(r)$ vs. T . The insert figure in (c) gives the vertex values of the three peaks in $g_{BB}(r)$ versus the temperature T . The circle stands for the first peak from the left side in $g_{BB}(r)$, the square shows the second peak, and the triangle is for the third peak.

temperature on the pair distribution function is remarkable. The first peaks in $g_{AA}(r)$ and $g_{AB}(r)$ become narrower and their heights increase as the temperature goes down from $T = 0.6$ to $T = 0.0$. This trend is the same as both the one-component and binary LJ systems at higher temperatures [12, 15].

In figure 3.1 the second peaks in g_{AA} and g_{AB} split into two peaks when temperature is lowered, which is regarded as an evidence that the liquid is supercooled and has an increase of local packing [1, 12]. It is even more interesting to see that at $T = 0.2$, a shoulder appears on the left side of second peak (the left one of the two split peaks) in $g_{AA}(r)$, and as the temperature goes down, this shoulder becomes gradually higher. At $T = 0.1$, a three-peak shell is formed, which is more obvious at lower temperature $T = 0.01, 0.0$. Yet, the three-peak split is not observed in $g_{AB}(r)$ even at the lowest temperature $T = 0.0$. The two insert graphs in figure 3.1 exhibit the maximum value of $g_{AA}(r)$ and $g_{AB}(r)$ at various temperatures. Obviously, the relation between the peak value of $g(r)$ and the temperature is not linear. It seems that there is an inflection point around $T = 0.4$.

There are several points that need to be stressed here: (1) the shoulder in g_{AA} and g_{AB} may occur at some higher temperature between $T = 0.2$ and $T = 0.4$. Thus it is necessary to continue the study of the system at temperature $0.2 < T < 0.4$ with the same shear $\dot{\gamma} = 0.01$. (2) The reason why the three-peak split happened in g_{AA} is not clear. Is it because of the even lower temperature just like the two-peak split in the supercooled region? Does shear play an important role in this? Varnik has pointed out that for a sheared glass ($T < T_c$) dynamics of the system is totally dominated by the shear, since the mobility of the particles caused by thermal fluctuations can be neglected [10, 11]. Then the question is posed immediately: are the static properties of the system also fully controlled by the imposed shear when the temperature is lower than T_c ? To solve these issues, the same system with many other shear rates needs to be investigated. In that case, the shear dependence for the static behavior can be achieved. The range of shear rate picked by Varnik is about 3×10^{-5} to 10^{-1} , which is also a good choice for our work, because we all use the same model, namely, KA binary LJ mixture. The only difference is that they used the molecular dynamics simulation, while we simulate the system via Brownian dynamic method. (3) As revealed by the two insert figures, there are two regions, in the higher temperature part the line is close to linear, yet it is a curve in the lower temperature region. It would be interesting to check if the inflection point appears at $T_c = 0.435$. This will again help to figure out if the shear is dominant when the temperature is below T_c . With this purpose, the system with many temperatures around T_c needs to be studied.

The shape of $g_{BB}(r)$ looks quite differently from g_{AA} and g_{AB} . Kob and Andersen observed a decrease of the first peak in g_{BB} as the temperature went down from $T = 5.0$. At about $T = 0.8$, the peak changed into a shoulder. Almost at the same temperature, similar to $g_{AA}(r)$ and $g_{AB}(r)$, the second peak split [1].

The same phenomenon was reported by Gallo et al. [12]. Interestingly, they found that the first peak would go up if the temperature continued to be lowered. Finally the first peak was recovered.

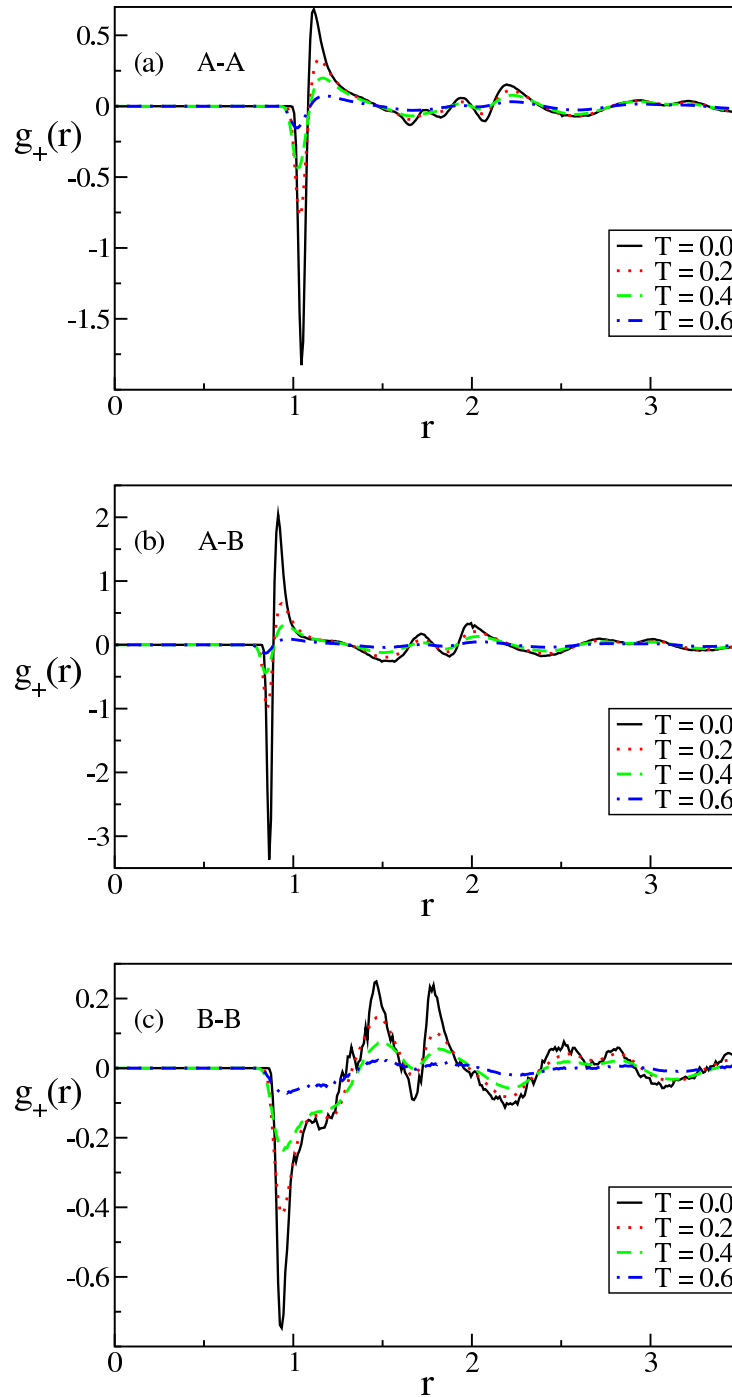


Figure 3.2: The first anisotropic term of the pair distribution function for the binary Lennard-Jones system at various temperatures, $T = 0.0, 0.2, 0.4,$ and 0.6 from top to bottom in each panel. Notice the three panels are in different scales to make sure the temperature dependence of $g_+(r)$ in each figure can be told clearly.

So far, we have carefully studied the isotropic part of the pair distribution functions and compared them with the results reported by Kob [1] and Rovere [12]. Now we will calculate $g_+(r)$ for different particle pairs $A - A$, $A - B$, $B - B$ to check if the system is anisotropic. In this work, the system is not expected to be completely isotropic since a small shear is applied, especially for the very low temperature $T = 0.0$.

As we have introduced in Chapter 2, $g_+(r)$ denotes the projection of the pair correlation on $\hat{x}\hat{y}$ plane [16], and is expressed in the form,

$$g_+(r) = \frac{15}{4\pi} \int d\hat{\mathbf{r}} \hat{x}\hat{y}g(\mathbf{r}) , \quad (3.9)$$

which is the first anisotropic component of the pair distribution function.

Our speculation is verified by figure 3.2. When the mixture is very cold, $T = 0.0$, the peaks of $g_+(r)$ for all particle pairs are quite strong, showing that the system is anisotropic. This is because when temperature is 0, the imposed shear controls the diffusion of the particles and forces the system to be anisotropic. On the other hand, as the temperature goes up, the thermal fluctuations become more important, the system becomes more isotropic. At $T = 0.6$, the effect induced by shear is eliminated by thermal fluctuations, the system is almost isotropic. This can be seen from figure 3.2 that all the peaks are very small, and $g_+(r)$ oscillates around 0 slightly. It is very interesting that for the particle pairs $A - A$, a triplet-peak in $g_+(r)$ is observed, and for $A - B$, the double-peak occurs. These phenomena have also been observed in $g_{AA}(r)$, $g_{AB}(r)$ (see figure 3.1).

3.3.2 Static structure factor

The static structure factor is calculated by this formula [14],

$$S_{\mu\nu}(\mathbf{k}) = \frac{1}{N} \langle \rho_\mu(\mathbf{k})\rho_\nu(-\mathbf{k}) \rangle . \quad (3.10)$$

Following the convention, μ, ν can be species A or B , $\rho(\mathbf{k})$ is the Fourier transform of the local density $\rho(\mathbf{r})$,

$$\rho(\mathbf{k}) = \sum_{i=1}^N \exp(-i\mathbf{k} \cdot \mathbf{r}_i) . \quad (3.11)$$

The partial structure factors S_{AA} , S_{AB} , S_{BB} along y direction and z direction are evaluated via equation 3.10. From the previous section, we got the fact from $g_+(r)$ that the system is anisotropic at lowest temperature $T = 0.0$. This can also be illustrated by shape of $S(k)$, but it is not so obvious.

With $T = 0.0$, the partial structure factors $S(\mathbf{k})$ for different particle pairs $A - A$, $A - B$, $B - B$ along the velocity gradient direction \hat{e}_y and the vorticity direction \hat{e}_z are plotted in figure 3.3. The plots show that

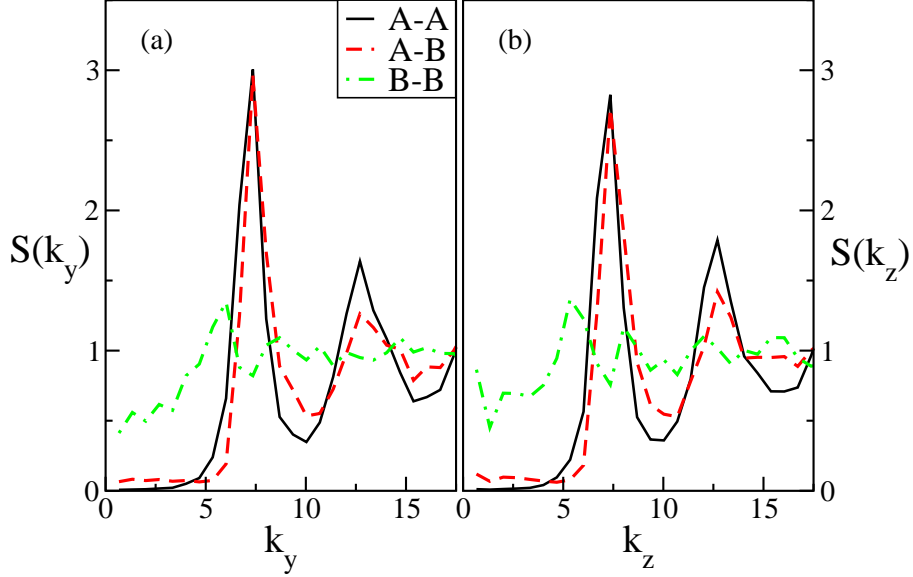


Figure 3.3: The static structure factors of the LJ mixture with imposed shear $\dot{\gamma} = 0.01$ at temperature $T = 0.0$. The left panel shows $S(k_y)$ versus k_y along the velocity gradient direction \hat{e}_y and the right panel is that along the vorticity direction \hat{e}_z . The solid lines show $S_{AA}(k_\alpha)$, the dashed lines are $S_{BB}(k_\alpha)$, and the dashed - dot lines give $S_{AB}(k_\alpha)$, where $\alpha = y$, or z .

the pronounced peaks of S_{AA} and S_{AB} along y direction are slightly higher than that along z axis. This means that the system is indeed anisotropic at $T = 0.0$ with shear $\dot{\gamma} = 0.01$. Another feature in this figure is that the second peaks in all three partial structure factors along z direction are higher than those along y axis. As the temperature increases, the system tends to become more isotropic, the discrepancy between $S(k_y)$ and $S(k_z)$ becomes neglectable. From the $g_+(r)$ it can be seen that at $T = 0.4$ the system is still somewhat anisotropic, while this cannot be found from the static structure factor.

In figure 3.4, $S(k_y)$ versus k_y are plotted for different particle pairs $A - A$, $A - B$, and $B - B$, at various temperatures, from $T = 0.0$ to $T = 0.6$. In this figure, only the structure factor along the velocity gradient direction \hat{e}_y is displayed, because for $T \geq 0.2$, $S(k_z)$ is very close to $S(k_y)$ for all three pairs. For $T = 0.0$, the partial structure factors for both y and z directions have already been plotted in figure 3.3.

There are two important features in figure 3.4. First of all, the locations of the maximum of $S(k)$ are independent of the temperature. For $S_{AA}(k)$, $k_{max,A} = 7.25$, and for $S_{BB}(k)$, $k_{max,B} = 5.75$. In the following section, the intermediate scattering function will be calculated fixed at those k_{max} . In comparison with the results reported by Kob and Andersen [2], the locations of the first peaks for both $S_{AA}(k)$ and $S_{BB}(k)$ are the same as theirs. Notice that our system is driven by shear at all the temperatures. This

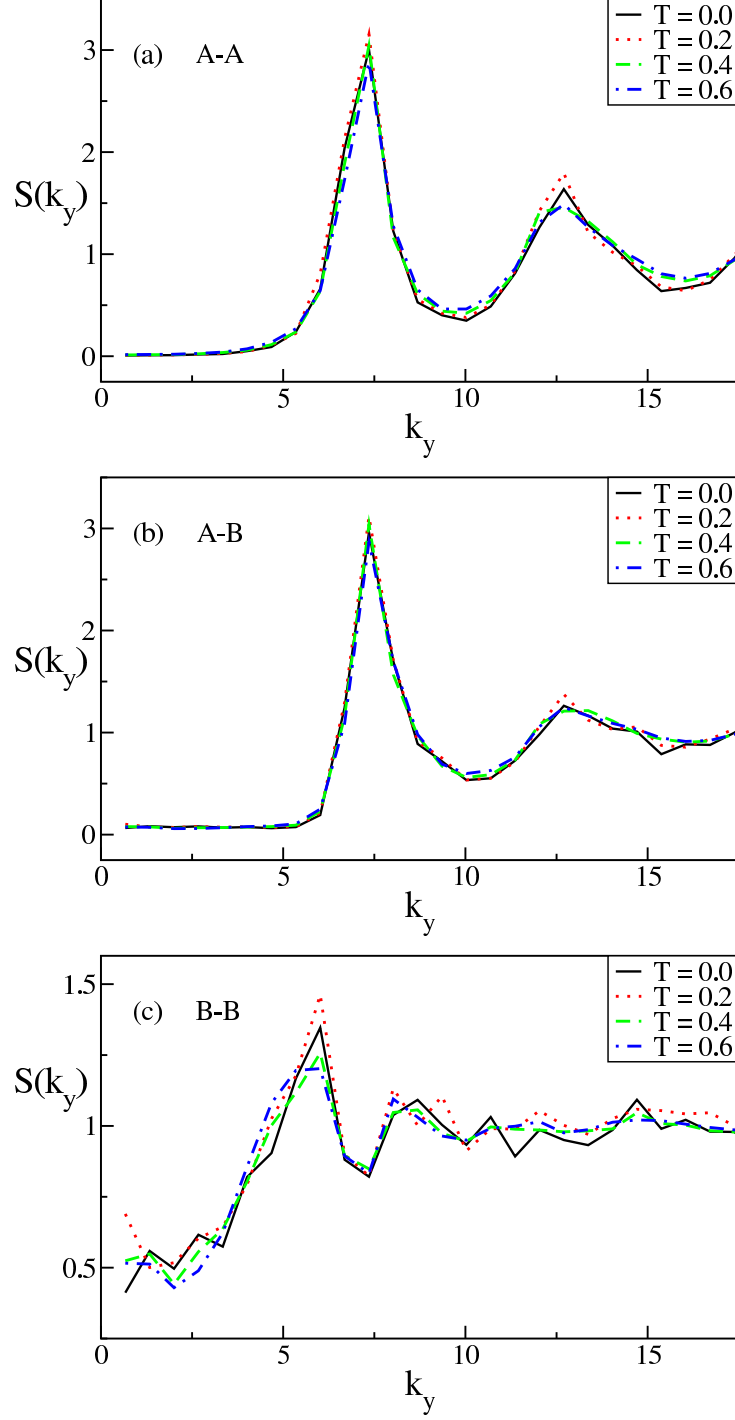


Figure 3.4: The partial structure factor of binary LJ system along y direction for different particle pairs $A - A$, $A - B$, and $B - B$, at various temperature, $T = 0.0, 0.2, 0.4, 0.6$. Notice that the figure on the bottom has different y-scale from the above two, because S_{AA} and S_{AB} are much larger than S_{BB} .

implies that the locations of the maximum in $S_{AA}(k)$ and $S_{BB}(k)$ are either independent of the shear, or the shear rate $\dot{\gamma} = 0.01$ is too small to change them. We prefer the conclusion that the shear has no effect on the

position of the peak for two reasons. Number one, even at the lowest temperature $T = 0.0$, the location is still unchanged, where obviously the shear has overwhelming impact on the system. Number two, according to Varnik [10, 11], $\dot{\gamma} = 0.01$ is a quite large shear rate for the supercooled and glassy system.

The second feature is that, compared with the results reported by W. Kob et al. [2] in the supercooled region ($T = 0.6, 0.55, 0.5$), S_{AA} , S_{AB} , and S_{BB} from our simulations are systematically larger than theirs, especially the shape of S_{AB} is quite different. This discrepancy may be attributed to the imposed shear. To demonstrate this assumption, the system with various shear rates should be investigated.

3.4 Dynamical behavior of a sheared binary Lennard-Jones system

We now focus on the dynamics of the Kob-Andersen binary Lennard-Jones system. The mean square displacement, the diffusion coefficient (D), the self-intermediate scattering function $F(\mathbf{k}, t)$, the alpha-relaxation time and the self-part of the van Hove function $G(\mathbf{r}, t)$ were calculated. To study the dynamical performance of the LJ mixture under shear, the mean square displacement is the first quantity that should be considered to make sure the simulation time is long enough and the diffusive behavior of particles has emerged.

3.4.1 Mean square displacement

The mean square displacements for the particle A along the velocity gradient direction \hat{e}_y and the vorticity direction \hat{e}_z are presented in figure 3.5. All the data are plotted in a double logarithmic scale. For particle B , the mean square displacement has the same shape as that for particle A . Thus it is not shown here.

From figure 3.5, we find the mean square displacements along y and z directions are almost the same for all the temperatures we simulated. Thus the anisotropic behavior cannot be observed from the mean square displacement.

At very short time, the Brownian particles undergo free diffusion, the mean square displacement is linear with the time t , and the diffusion coefficient is D_0 [8], which has been expressed by the equation 3.7. Since this process is very short, and as we will point out later, the shear plays an important role in long time diffusion. This very early diffusion is not important in our research, and thus is not shown in the figure 3.5.

After the free diffusion, a plateau occurs in the mean square displacement. This plateau is considered as a feature that the system is in the supercooled regime, and can be explained by the so called ‘cage effects’ [1, 8, 11, 12]. When system is cooled down or compressed to approach the glass transition, most particles tend to be trapped at their initial position because of the ‘cages’ formed by their neighbors. These

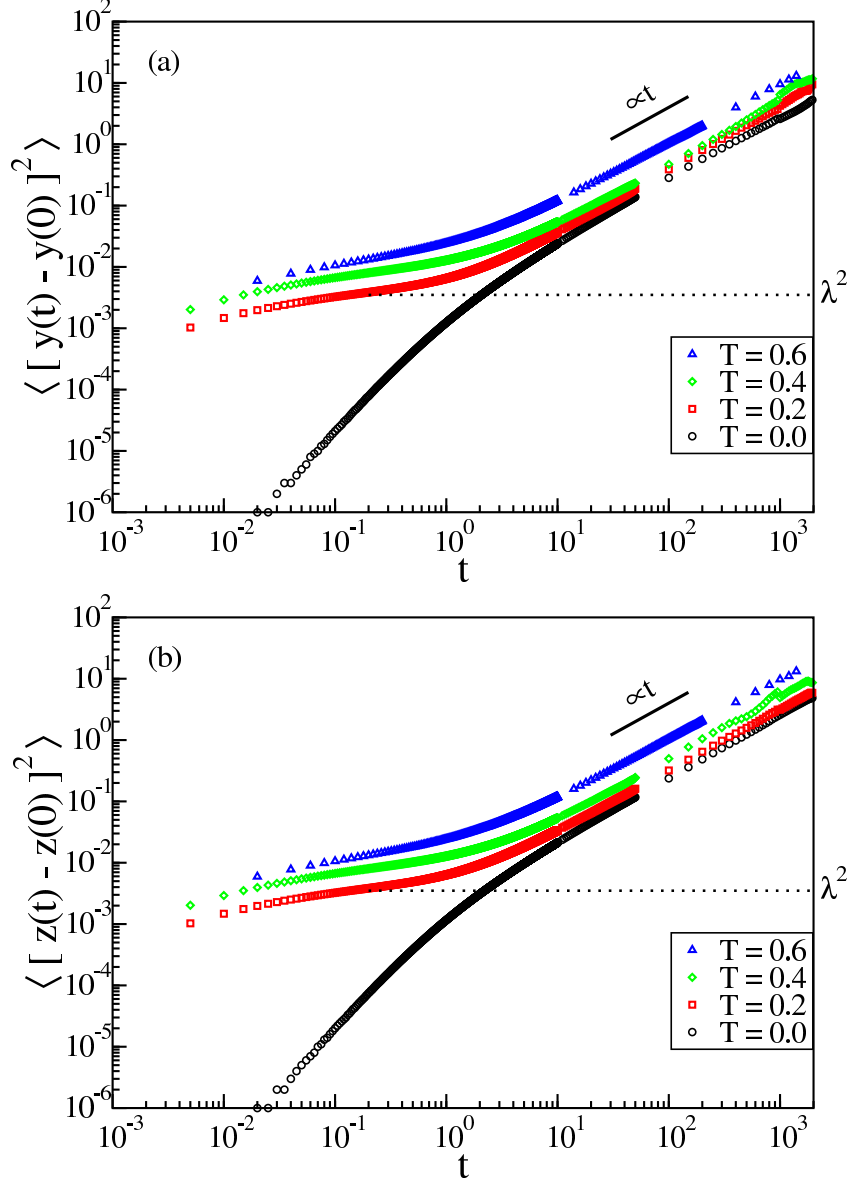


Figure 3.5: The means square displacement versus t for a large particle A in the binary LJ mixture at various temperatures. From top to bottom, the temperatures are $T = 0.6, 0.4, 0.2, 0.0$ (a) along the velocity gradient direction \hat{e}_y , (b) along the vorticity direction \hat{e}_z .

trapped particles are called immobile particles. On the contrary, very few particles can move very fast, which are named mobile particles. The formation of the cage is intrinsically caused by the strong repulsion between the particles [17]. After time t_{ca} , the observed particle escapes from the cage, goes into the diffusive regime. As the temperature goes down close to the critical point, t_{ca} increases very quickly. Once the time interval t_{ca} is too large for human to wait, the glass is formed.

The height of the plateau in the mean square displacement gives the square of the average distance that a particle can move before it escapes from the cage. This distance is denoted as the ‘cage size’ λ [4]. Actually, the plateau is not flat, so we use the height at the inflection point to calculate λ [8]. The cage sizes are plotted in figure 3.6 versus the temperatures.

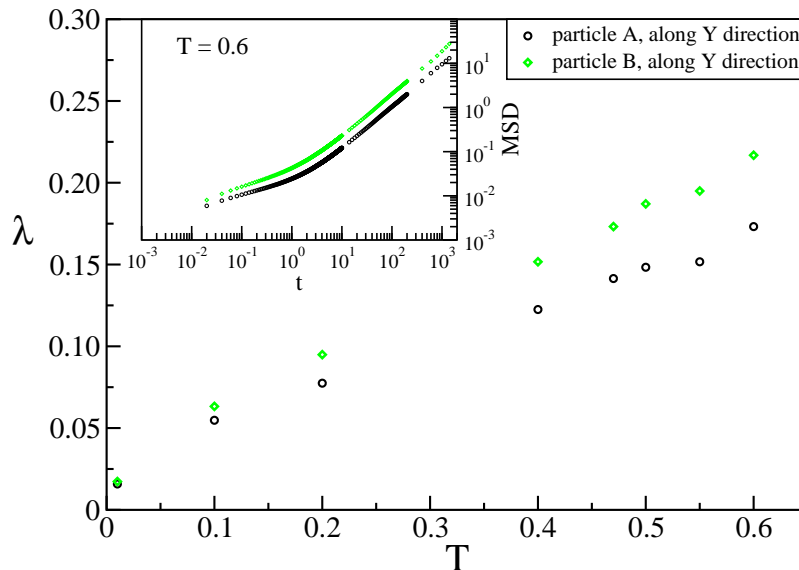


Figure 3.6: The cage size vs. the temperature. The black circle shows particle A along the velocity gradient direction \hat{e}_y , the green diamond stands for particle B along y direction. For both particle A and B the λ along z direction has exactly the same values as that long y axis, thus is not drawn in this figure. The insert figure shows the mean square displacement for both species A and B along y direction at temperature $T = 0.6$. It can be seen that the plateau for particle A is lower than that for B.

Figure 3.6 shows that the cage size decreases with lowering the temperature. This is in agreement with the results reported by Bordat et al. [4]. However they addressed that the cage size of particle A is larger than that of B, which is in conflict with Figure 3.6. The Brownian dynamics simulation performed by Flenner et al. [9] shows that $\lambda_A = 0.17$ and $\lambda_B = 0.21$ at $T = 0.44$. Thus λ for particle A is smaller, in accordance with our results. This may be understood by considering that the species B has more mobile particles [4], caused by two reasons: first, the size of particle B is smaller than A. Thus it is easier to escape from the cage. Second, the force between two B particles is smaller than that between A and B, and also that between A and A particles (refer to table 3.1). Thus more B particles become mobile as temperature goes up and the local packing is reduced. This can also be seen from the pair distribution function (refer to figure 3.1). From $T = 0.47$ to $T = 0.6$, there is only a shoulder in $g_{BB}(r)$ at the location where the first peak is expected. It needs to be stressed here, λ is actually an average distance including both immobile and mobile particles

during the intermedial time. It will be interesting to find the cage size only for immobile particles. To do so, one should pick a criterion to determine which particle is immobile. Several different ways to choose the particles have been discussed [5, 18].

At longer time, the diffusive behavior is restored after the plateau. The diffusion coefficient can be obtained from the slope of the mean square displacement in this long time range,

$$\langle [y(t) - y(0)]^2 \rangle = 2D_y t , \quad (3.12)$$

where $y(t)$ is the y -component of position of the particle, D_y is the diffusion coefficient along y direction. The same form can be written for the z axis. When the system is isotropic, the diffusion coefficients are the same for both directions.

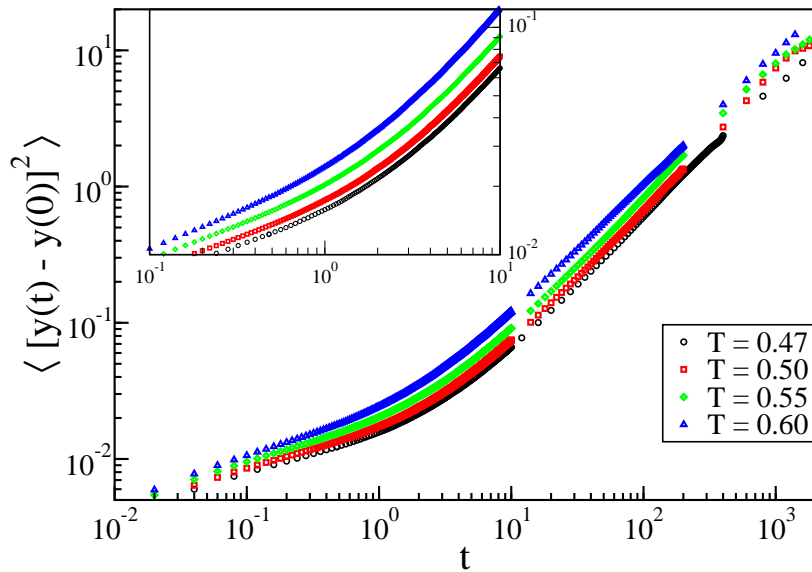


Figure 3.7: The mean square displacement along y direction versus t for a large particle A in the binary LJ mixture within the supercooled region. The temperatures from top to bottom are $T = 0.6, 0.55, 0.5, 0.47$. The insert figure shows the same thing with enlarging the crossover part (from the plateau to the diffusion).

We compare our mean square displacements for the systems in the supercooled region ($T = 0.47, 0.5, 0.55, 0.6$) with those reported by Szamel and Flenner [8, 9]. We find that the shapes for the whole time look similar, both have the plateau and the long-time diffusion. With increasing temperature, the height of plateau increases, and the time t_{ca} that the plateau exists become a little longer (see figure 3.7).

The differences exist too. In our calculation, the time interval t_{ca} that plateau lasts is shorter than theirs. This is more obvious as the temperature goes down from $T = 0.6$ to $T = 0.47$. This is very easy to understand, with lowering the temperature, the effect of shear rises, making the structure relax faster. Thus the cage can exist in a shorter time. However, it is very surprising that the cage size is smaller in our calculation. With shear, the plateau of the mean square displacement is supposed to be higher, since the shear can enhance the diffusion of the particles. One explanation may be made here is that shear does not have effect on the dynamics of the system during the short time [10]. But more reasons should be found to explain why the cage size is smaller than the one without shear. As expected the diffusion coefficient is larger for the system under shear. We will discuss this in the next part.

At low temperatures $T < T_c$, because of the imposed shear, the particle caging is suspended, the diffusive motion is restored, and D is not vanished. Interestingly, as temperature goes down from $T = 0.4$ to $T = 0.0$, the time interval t_{ca} for the plateau decreases (see figure 3.5). This is totally on the opposite way compared with the situation when $T > T_c$, which is shown in figure 3.7. This phenomenon happens because under the mode-coupling temperature T_c , the dynamics of the system is controlled by shear. As the temperature is lowered the shear is even more dominant. Thus the cage is destroyed more quickly. At $T = 0.0$ the plateau disappears, and the dynamics of the system is completely dominated by the imposed shear.

In this section, we studied the mean square displacement of the system at various temperature. We found that MSD was very sensitive to the imposed shear. In the supercooled system ($T > T_c$) under shear, the time interval t_{ca} of the plateau is shortened, and the height is reduced. For the sheared glass ($T < T_c$), the system shows liquid-like behavior, and diffusive motion is recovered [10]. With all the temperatures that we studied, the cage size grows with increasing temperature for both A and B species. When T is larger than T_c , the time t_{ca} for the plateau to exist is somehow increasing as the temperature goes down. On the other hand, as T is lower than T_c , it is obviously that, t_{ca} decreases fast with lowering the temperature. Interestingly, notwithstanding that the imposed shear has important effect on the mean square displacement, the anisotropy is not seen from MSD.

3.4.2 Diffusion coefficient

According to equation 3.12, the diffusion coefficient D can be evaluated by fitting the mean square displacement in the diffusive regime. The diffusion coefficients versus temperature for both particle components A and B along the velocity gradient direction \hat{e}_y and the vorticity direction \hat{e}_z are plotted in figure 3.8. This figure shows that the diffusion coefficients grow with heating up the system. D for the small particle B is larger than that of large particle A . The difference become larger with increasing temperature. This again

gives an evidence that particle B is more mobile. The reason has been explained in the previous subsection. There is no obvious distinction between y and z directions. Thus the anisotropic phenomenon is not observed in the diffusion coefficients.

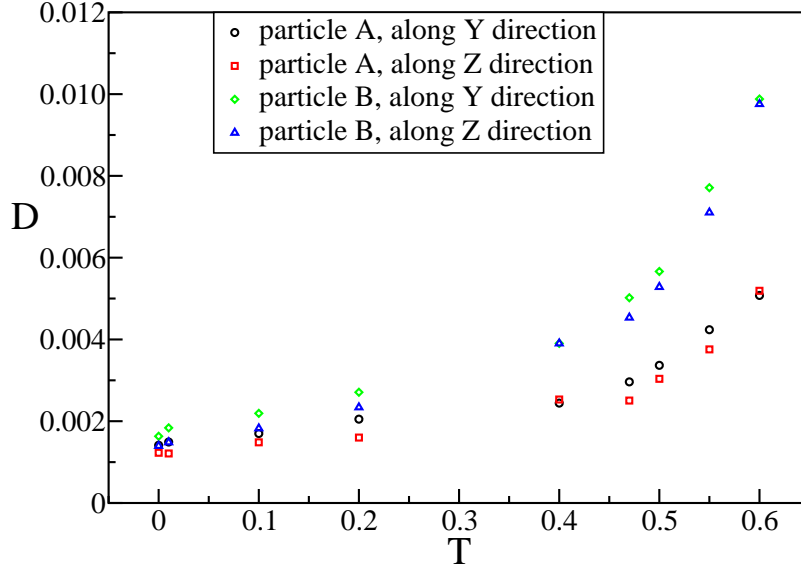


Figure 3.8: The diffusion coefficient versus temperature. Both particle A and B along the velocity gradient direction and the vorticity direction are plotted.

As $T < T_c$, the increase of the diffusion coefficient due the temperature is slow, yet when $T > T_c$, D goes up rapidly with the temperature. In the supercooled region, the dynamics of the liquid is dominated by the temperature. The diffusion is accelerated by increasing temperature. On the other hand, when $T < T_c$, the thermal fluctuation is small, the imposed shear is not only a perturbation, but plays a critical role in the dynamics of the system. Thus the diffusion coefficient shows weak dependence on the temperature.

By comparing the diffusion coefficient of the system under shear with the corresponding equilibrium system (without shear) studied by Szamel et al. [8, 9], we find that D is increased by the impose a shear. When $T < T_c$, according to the mode-coupling theory, the diffusion coefficient vanishes. Due to shear, the diffusion of the particles is recovered, the system goes back into the liquid-like state. When the temperature is above T_c , the enhancement of D caused by the shear reduces as the temperature goes up. This means that the effect of shear on the dynamics is limited with increasing temperature.

Based on the discussion we made above, shear plays an important role in affecting the dynamics of the system, especially at the lower temperatures. Eisenmann et al. point out that ‘shear can be regarded as an effective temperature.’ [19] Inspired by this idea, and also to follow the work we have done for the one

component simple colloid liquid in Chapter 2, we try to investigate the so called ‘effective temperature’ T_{eff} here. However, in this chapter the effective temperatures are defined in a totally different way from what we used in the previous chapter.

As we have alluded to in the introduction part, the mode-coupling theory can predict the relation between the diffusion coefficient and the temperature in supercooled liquids (refer to equation 3.1). The formula $D \propto (T - T_c)^\gamma$ has been used to fit the diffusion coefficients calculated from the MD and BD simulations, and both generated similar results [1, 9]. However, the mode-coupling equation 3.1 cannot be used for a non-equilibrium system (i.e. the driven fluid under shear) directly. One obvious difference is mode-coupling theory predicts that the diffusion coefficient would vanish and the structural relaxation would diverge as the temperature approaches a non-zero T_c [1, 6]. On the contrary, as an inspection of figure 3.8 reveals, the system under shear has non-zero diffusion coefficient even when the temperature is at 0.0.

For a driven system, the dynamics is not determined by the bath temperature alone, but is controlled via a combined effect caused by the temperature and the perturbation together. Suppose that there is a quantity T_{eff} , which can play the similar role as the ‘normal’ temperature does for the equilibrium system, and the mode-coupling equation is still satisfied with this effective temperature. Based on these two assumptions, equation 3.1 can be rewritten with $T_{eff, D}$ instead of T ,

$$D_\mu = a_\mu (T_{eff, D}(T, \dot{\gamma}) - T_c)^{\gamma_\mu} , \quad (3.13)$$

where a_μ is a constant, γ_μ is the exponent, and following the convention, μ can be species A or B . Obviously the effective temperature $T_{eff, D}$ is a function in terms of the bath temperature T and shear rate $\dot{\gamma}$.

To find the effective temperature for the driven system, the corresponding equilibrium system needs to be studied. The diffusion coefficients of these equilibrated systems at various temperatures are fitted via the mode-coupling theory (equation 3.1). The parameters a , γ , and T_c are achieved from the fitting. Then those parameters, as well as the diffusion coefficient of the non-equilibrium system are taken into equation 3.13, the effective temperature can be calculated.

For our system, the parameters a , γ , and T_c have been calculated by Flenner et al. [9]. In their paper, they investigated the Kob-Andersen supercooled Lennard-Jones system with Brownian dynamics simulation. In our work, we extend the study by applying a shear $\dot{\gamma} = 0.01$ on the system. According to the procedure we expressed above, the parameters are used in equation 3.13. As is commonly accepted, $T_c = 0.435$. For particle A , $a_A = 0.17$, $\gamma_A = 2.17$; for species B , $a_B = 0.27$, $\gamma_B = 1.97$ [9]. With the diffusion coefficients of the sheared system, the effective temperatures are calculated and plotted in figure 3.9.

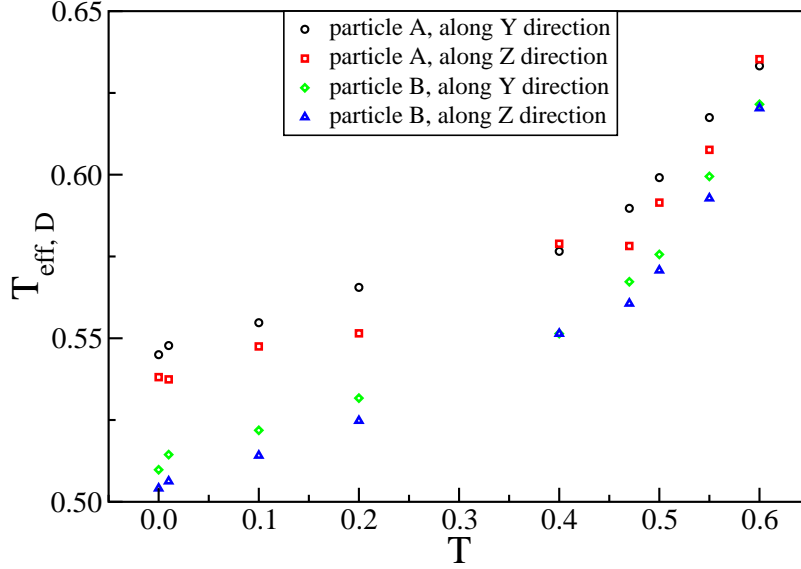


Figure 3.9: The effective temperature versus the bath temperature. The effective temperatures are estimated by fitting the diffusion coefficient with equation 3.13. See text for details. Both particle A and B along the velocity gradient direction and the vorticity direction are plotted.

From the figure of the effective temperature, we find that $T_{eff, D} > T$ for all the bath temperatures we investigated. In the lower temperature range $T < T_c$, the imposed shear plays a primary role in increasing the effective temperature. Specifically, at $T = 0.0$, the effective temperature is larger than 0.5, and as the bath temperature increases, the $T_{eff, D}$ goes up slowly. From $T = 0.0$ to $T = 0.4$, the effective temperature only increases about 8%. In the supercooled range ($T > T_c$), the bath temperature affects the system more forcefully. As the bath temperature goes up, $T_{eff, D}$ increases more quickly than in the lower temperature range. At $T = 0.6$, the effective temperature is only about 5% larger than the bath temperature.

Another interesting feature found in figure 3.9 is that the effective temperature for the particle A is larger than that for particle B, especially when the bath temperature is small. Yet, for the same temperatures ($T \leq 0.2$), the diffusion coefficient for the species A and B are very close (see figure 3.8). Technically, this is caused by the fact that the parameters (a_μ and γ_μ) in the mode-coupling equation 3.13 are different for particle A and B. Thus the similar diffusion coefficients give rise to distinct effective temperatures. However, it is not clear if this is an inevitable phenomenon caused by the shear. The conclusion that the shear has more effects on particle A cannot be made so far. To clarify this issue the investigation should be extended by exploring the system with other shear rates.

Here, we need to voice several words of caution regarding the method we used to find the effective temperatures. First of all, Flenner et al. have pointed out that the parameters in the mode-coupling equation are not unique. With different fitting ranges, the values can be different. As a result, the effective temperatures achieved in this way may not be unique either. Second, the physical meaning of this definition of the effective temperature is arguable. If this $T_{eff, D}$ can play a similar role as the bath temperature does for the equilibrium system needs to be carefully examined. Generally speaking, this method is straightforward, but quite coarse. Later on, we will propose other definition of the effective temperature with considering the Stokes-Einstein relation.

We studied the long-time diffusion coefficients in this part, and found D is mainly determined by the temperature when $T > T_c$, and the small particles have fast diffusive motions than the larger particles. On the other hand, at lower temperature, $T < T_c$, the long-time diffusion is restored by the imposed shear, and has weak dependence on the bath temperature. To quantify the effect of the bath temperature and the shear on the dynamics of the system. The ‘effective temperature’ is defined as a function of bath temperature and shear. We proposed a very simple method to calculate the effective temperature by extending mode-coupling theory. The dependence of the $T_{eff, D}$ on T has been analyzed. To study the effect of the shear on the effective temperature, the systems with various shear rates need to be studied in the future.

3.4.3 Self-intermediate scattering function

In the previous section, we indicated that the static structure factor $S(\mathbf{k})$ is the autocorrelation function of the Fourier component of the local density $\rho(\mathbf{r})$. Now consider a more general situation that density is time dependent $\rho(\mathbf{r}, t)$. Then the time dependent autocorrelation function of $\rho(\mathbf{k}, t)$ is named as the ‘intermediate scattering function’ with the expression [14],

$$F(\mathbf{k}, t) = \frac{1}{N} \langle \rho(\mathbf{k}, t) \rho(-\mathbf{k}, t) \rangle . \quad (3.14)$$

Comparison with equation 3.10 immediately gives,

$$F(\mathbf{k}, t = 0) = S(\mathbf{k}) . \quad (3.15)$$

Similar with $S(\mathbf{k})$, $F(\mathbf{k}, t)$ can also be measured experimentally by neutron scattering which is a good method to study the microscopic dynamics of liquids, since the magnitude order of energy and length related to neutron are comparable to thermal energy and spacing of particles [14]. The dynamic structure factor

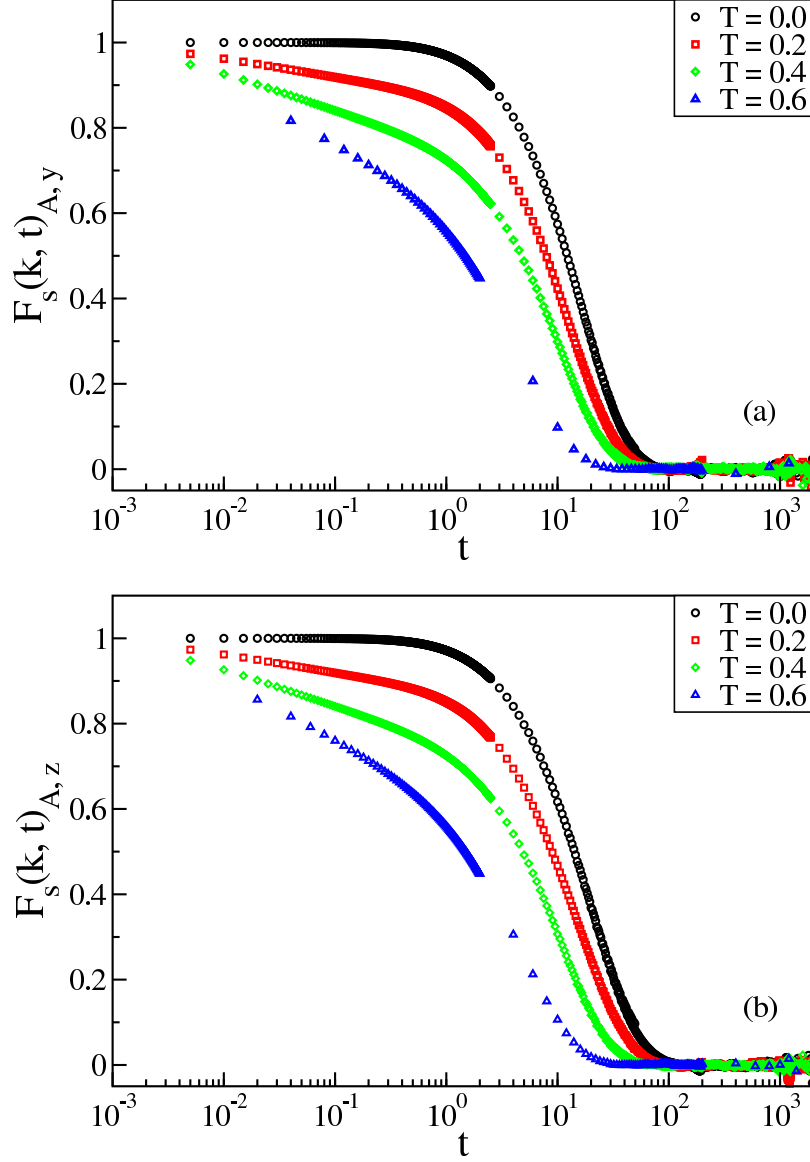


Figure 3.10: The self-intermediate scattering function $F_s(\mathbf{k}, t)$ versus time for the large particle A calculated at the wave vector $k = 7.25$, the location of the first peak in the partial structure factor $S_{AA}(k)$. (a) along the velocity gradient direction \hat{e}_y , (b) along the vorticity direction \hat{e}_z . The temperatures from the top to the bottom in each panel are $T = 0.0, 0.2, 0.4, 0.6$.

$S(\mathbf{k}, \omega)$ needs to be introduced in neutron scattering experiments,

$$S(\mathbf{k}, \omega) = \frac{1}{2\pi} \int_{-\infty}^{\infty} F(\mathbf{k}, t) \exp(i\omega t) dt, \quad (3.16)$$

which is the spectrum of $F(\mathbf{k}, t)$. In the experiment, $S(\mathbf{k}, \omega)$ can be calculated from the cross-section σ ,

$$\frac{d^2\sigma}{d\Omega d\omega} = b^2 \left(\frac{k_2}{k_1} \right) N S(\mathbf{k}, \omega) . \quad (3.17)$$

In the equation, Ω is the solid angle, $\hbar\omega$ is the transferred energy during collision, $\hbar\mathbf{k}_1$ and $\hbar\mathbf{k}_2$ are the momenta of neutron before and after scattering, b is the scattering length. After the dynamic structure factor $S(\mathbf{k}, \omega)$ is obtained via experiment, the intermediate scattering function $F(\mathbf{k}, t)$ can be evaluated, and the dynamic behavior of the liquid can be investigated.

The intermediate scattering function can also be linked to van Hove function by applying the Fourier transform [14],

$$F(\mathbf{k}, t) = \int G(\mathbf{r}, t) \exp(-i\mathbf{k} \cdot \mathbf{r}) d\mathbf{r} . \quad (3.18)$$

In the following section, we will describe the details of van Hove function, and show that $G(\mathbf{r}, t)$ can be separated into two parts, the ‘self’ part $G_s(\mathbf{r}, t)$, and the ‘distinct’ part $G_d(\mathbf{r}, t)$. Accordingly, $F(\mathbf{k}, t)$ can also be written into two part, $F_s(\mathbf{k}, t)$ and $F_d(\mathbf{k}, t)$. The structural relaxation and dynamic behavior can be investigated by considering the self-intermediate scattering function [12],

$$F_s(\mathbf{k}; t) = \frac{1}{N} \left\langle \sum_{i=1}^N \exp \{ i\mathbf{k} \cdot [\mathbf{r}_i(t) - \mathbf{r}_i(0)] \} \right\rangle . \quad (3.19)$$

In the previous section, the k_{max} for all cases have been obtained, where the static structure factors arrive at its maximum. With those k_{max} , the self-intermediate scattering functions for particle A along the velocity gradient direction \hat{e}_y and the vorticity direction \hat{e}_z are drawn in figure 3.10. The self-intermediate scattering function for B particles has the same shape as that for A particles, thus is omitted here.

Figure 3.10 shows that there is a plateau in the self-intermediate scattering function at almost the same time interval, in which the mean square displacement has a plateau. This plateau in $F_s(k, t)$ is also caused by the cage effect [8, 9], which we have discussed in the previous part for the MSD. When the temperature goes up, the time interval of the plateau becomes shorter, and the height of the plateau decreases. This is because the structural relaxation is faster and the particles can escape from the cage sooner with increasing temperature. This can also be observed via the structural relaxation time, which we will discuss in the next section. In comparison with the equilibrium system reported by Szamel and Flenner [8, 9], when $T > T_c$, the plateau is less evident under shear. The underlying reason is that the structural relaxation is accelerated by the impose shear, the enhancement increases as the bath temperature is lowered. As $T < T_c$, the infinite plateau is eliminated by shear. Finally the cage is broken, the structural relaxation is restored after the plateau even at $T = 0.0$. In the sheared glass, the imposed shear plays a similar role as the temperature.

3.4.4 Structural relaxation time

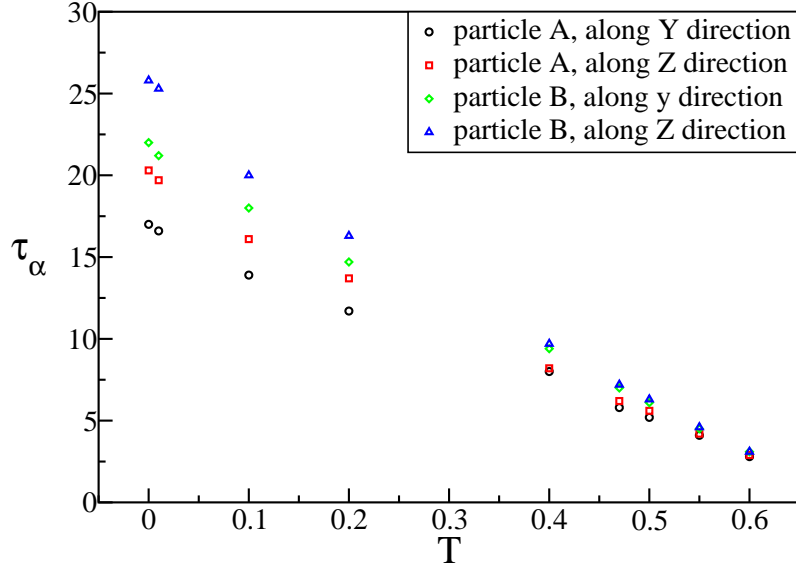


Figure 3.11: The temperature dependence of α -relaxation time extracted from the $1/e$ time of the decay of the self-intermediate scattering function $F_s(k, t)$. Both particle A and B are included along y and z axes.

The α -relaxation times τ_α for all temperatures have been evaluated when $F_s(k) = e^{-1}$, and they are plotted in figure 3.11. There are three striking features found from the figure. First, as was extensively demonstrated by many scientists [2, 8, 12, 20], the α -relaxation time decreases as the temperature goes up. This is because at higher temperature, the diffusion of the particles is larger, then the relaxation of the LJ mixture is faster. For supercooled liquids ($\dot{\gamma} = 0.0$), the relation between τ_α and T follows the prediction made by the mode-coupling theory with the formula 3.2 [2].

Secondly, with shear the structural relaxation time is dramatically lowered. We compare our results with those previously reported by Flenner et al. [9]. They studied the supercooled Kob-Andersen binary Lennard-Jones mixture by Brownian dynamics simulation, the only difference is that their systems are equilibrium. We find that at higher temperature $T = 0.6$ the value of τ_α is reduced about 50% with shear imposed. This reduction grows rapidly as the temperature goes down. At $T = 0.47$, τ_α is smaller by about two orders of magnitude than that without shear. When $T < T_c$, according to the mode-coupling theory, the structural relaxation time is infinite for the undriven system. In contrast, we find with the perturbation by the shear, the τ_α is finite, and is even not large. For example, the relaxation time is about 17.0 for particle A along the y direction at $T = 0.0$, less than 1% of the relaxation time of the equilibrium system at $T = 0.47$.

Third, at lower temperatures $T < 0.4$, the inequality $\tau_{\alpha,B,z} > \tau_{\alpha,B,y} > \tau_{\alpha,A,z} > \tau_{\alpha,A,y}$ exists. The relaxation time along the velocity gradient direction \hat{e}_y is systematically shorter than that along the vorticity direction \hat{e}_z . This inequality holds for both large particles A and small one B . The observation demonstrates that at lower temperature, the system is anisotropic. When $T \geq 0.4$, the relaxation times along y and z directions have almost the same value, showing that the system tends to be isotropic. As $T \geq 0.55$, the discrepancy in τ_α between species A and B disappears.

In the similar spirit to the definition of the effective temperature via the equation 3.13, we can also define an effective temperature by assuming the mode-coupling theory is valid for the relaxation time of the driven system, if $T_{eff, \tau}$ is used in the equation 3.2 instead of the bath temperature T ,

$$\tau_{\alpha,\mu} = a_\mu (T_{eff, \tau}(T, \dot{\gamma}) - T_c)^{-\gamma_\mu} . \quad (3.20)$$

In the equation, a_μ is a constant, γ_μ is the exponent. a_μ and γ_μ may not be exactly the same as those parameters in the equation 3.13. Following the convention, μ can be species A or B . The effective temperature $T_{eff, \tau}$ is a function in terms of the bath temperature T and shear rate $\dot{\gamma}$.

With the same the procedure we expressed for the diffusion coefficients, the parameters reported by Flenner et al. [9] are used in equation 3.20. It is commonly accepted that T_c equals 0.435. For particle A , $a_A = 0.061$, $\gamma_A = 2.45$; for species B , $a_B = 0.065$, $\gamma_B = 2.41$. With the α relaxation times of the sheared system, the effective temperatures are calculated and plotted in figure 3.12.

With the inspection of figure 3.12, we find the temperature dependence of the $T_{eff, \tau}$ is quite similar with that of the $T_{eff, D}$ (see figure 3.9). When the temperature is below T_c , the effective temperature is largely enhanced by the shear, and shows weak dependence on the bath temperature. On the other hand, as the bath temperature is above T_c , the influence of the imposed shear on the effective temperature is gradually eliminated with increasing the bath temperature. At $T = 0.6$, the $T_{eff, \tau}$ is only about 8% higher than the bath temperature.

It is interesting that the deviation between the effective temperatures for the particle A and B is smaller than that calculated from the diffusion coefficients. To figure out if those definitions for the effective temperature have some intrinsic physical meanings and if they can be used to describe the properties of the system, the first step needs to do is to check whether they agree with each other very well. With this purpose, the effective temperature obtained from the structural relaxation time is plotted versus the one gotten from the diffusion coefficients in figure 3.13.

Figure 3.13 shows for particle A , the two effective temperatures are very close, especially at higher temperatures. The difference between the two effective temperatures for particle B is slightly bigger. The

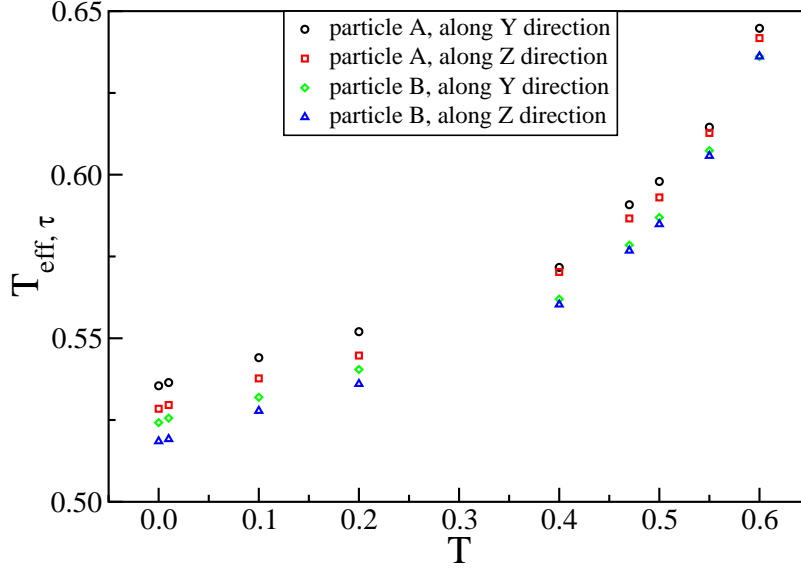


Figure 3.12: The effective temperature versus the temperature. The effective temperatures are estimated by fitting the diffusion coefficient with equation 3.20. See text for details. Both particle A and B along the velocity gradient direction and the vorticity direction are plotted.

largest discrepancy is less than 4%, indicating that the two sets of the effective temperatures match each other very well. It seems that the effective temperature defined via the mode-coupling theory can reveal some kind of intrinsic property related to the dynamic behavior of the system under shear. However, the precise conclusion is still too far to be made. The systems with other shear rates need to be investigated to make sure the equality between the two effective temperatures is not a coincidence. Moreover, the relation between other physical properties and the effective temperature needs to be inspected to guarantee that the effective temperature in the driven liquids is the counterpart of the bath temperature for the equilibrium system.

In this section, the structural relaxation time has been calculated from the self-intermediate scattering function. With the aid of the shear, τ_α is dramatically decreased when the temperature is smaller than T_c . For $T > T_c$ the effects of the shear is eliminated with increasing temperature because the shear rate is very small (unlike in the previous chapter). The anisotropic phenomenon is observed from the α relaxation time when the bath temperature is lower than T_c . The effective temperature is obtained from the τ_α based on the assumption that the mode-coupling theory is still satisfied if the $T_{eff, \tau}$, instead of the bath temperature, is used in the equation of the τ_α . At lower temperature $T < T_c$, the effective temperature is increased intensively by the imposed shear, while it goes up with the bath temperature when $T > T_c$. When the

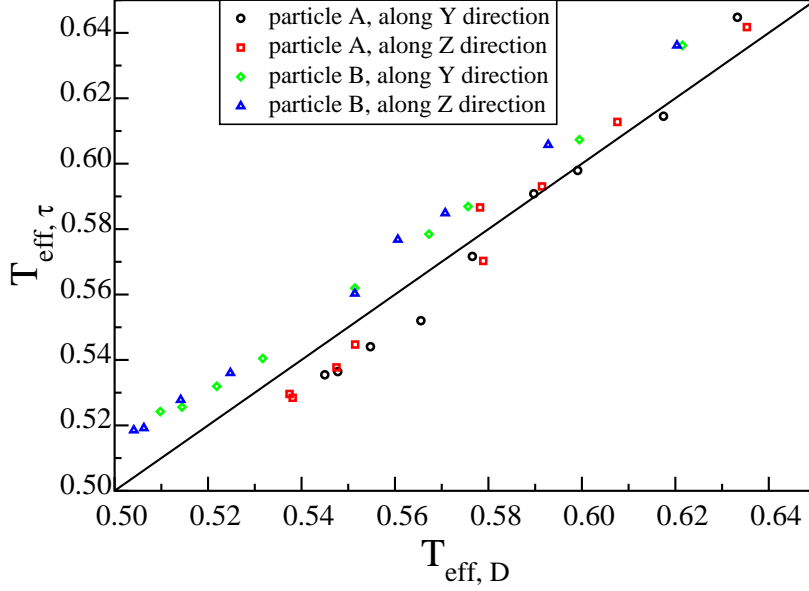


Figure 3.13: Comparison of the two sets of effective temperatures obtained from the diffusion coefficients ($T_{eff,D}$) and from the α relaxation times ($T_{eff,\tau}$). The solid line is $y = x$. Both particle A and B along the velocity gradient direction and the vorticity direction are plotted.

temperature is quite high, i.e. $T = 0.6$, under a very small shear the effective temperature is very close to the bath temperature. By comparing with $T_{eff,D}$, we found that the two definitions give equivalent results.

3.4.5 Breakdown of Stokes-Einstein relation

In this part we will test if the Stokes-Einstein (SE) relation is satisfied for our system. For the normal liquid (far from the glass transition), SE relation has been well established to connect the viscosity to the single-particle diffusion [14],

$$D\eta = \frac{k_B T}{b\pi d}, \quad (3.21)$$

where η is the viscosity, b is a parameter, which is equal to 3 if the ‘stick’ hydrodynamic boundary condition is applied, and is equal to 2 for ‘slip’ boundary condition. d is the hydrodynamic diameter of the particle [4]. The Stokes-Einstein relation can also be expressed with the structural relaxation time [21],

$$D\tau = \text{const.} . \quad (3.22)$$

This equation holds rigorously when the Brownian particles have much larger size than those of solvent molecules [21].

However, when the liquid is cooled down or compressed to approach the glass transition, the violation of the Stokes-Einstein relation has been observed in many experiments, i.e supercooled water [22], metallic glass-forming melts [23], etc. A large number of computer simulations also confirmed the breakdown of SE relation in the binary Lennard-Jones liquid [4, 7], hard-sphere fluid [5], metallic alloy [24, 25], and so on.

The breakdown of Stokes-Einstein relation is commonly accepted as a character of the spatially heterogeneous dynamics of supercooled systems [4, 5, 6, 7]. It is a common sense that the single-component liquid is homogeneous. However, this is true only when the temperature of the liquid is high than the onset temperature of slow dynamics [4]. For the Brownian particles, when the temperature is high, the random force is large (refer to 3.5 and 3.6), all the particles can diffuse rapidly in a ‘normal’ way. The positional fluctuation for all the particles is the same as the hydrodynamic diameter. In this case, Stokes-Einstein relation is valid [4].

On the other hand, in the supercooled regime ($T_g < T < T_s$), the dynamics of the system is usually spatially heterogeneous, which means the liquid can be divided into many small regions, the dynamics in one area can be extremely different from dynamics in the neighboring region. For example, the diffusion of some particles may be orders of magnitude faster than other particles which are only a few nanometers away [26]. Roughly speaking, the particles can be divided into two kinds: ‘mobile’ particles and ‘immobile’ particles. Although they are defined quantitatively in many different ways [5, 18], the general concept is the same, namely, immobile particles are trapped in the cage formed by their neighbors, yet mobile particles have large mobility during the time of observation, just as its name implies. Many people believe that mobile particles can move quickly via the so called ‘hopping’ process, and give rise to the Stokes-Einstein violation [5]. It needs to be stressed that the mobile and immobile behavior is not permanent. Immobile particles may get out of the cage and obtain large mobility later on, and mobile particles may be trapped after some time [11].

To examine the validity of the Stokes-Einstein relation, we plot the product $D\tau_\alpha$ versus the temperature in figure 3.14. With inspection of the figure, we found that $D\tau_\alpha$ is almost a constant as $T \leq 0.2$, which means the Stokes-Einstein relation is valid in this range of the temperature. This is perfectly consistent with the conclusion made by Varnik:”shear tends to restore the Stokes-Einstein relation” [11]. Since the violation of the Stokes-Einstein relation is a hallmark of dynamic heterogeneity [4, 5, 6, 7], this assessment may be extended that the imposed shear tends to recover the dynamic homogeneity of the system. On the other hand, for the higher temperature, the deviation from the Stokes-Einstein relation is observed. This is because the effect of the imposed shear on the dynamics of the system is limited when the temperature is relatively high.

In the discussion we made above, equation 3.22 is adopted to examine the validity of the Stokes-Einstein relation. The advantage of this equation is that there are only two quantities in the formula. Thus it is very

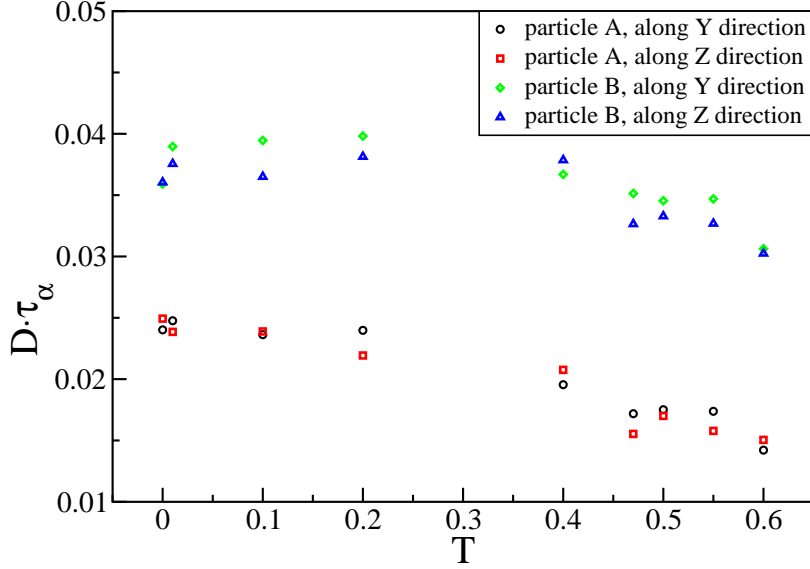


Figure 3.14: The temperature dependence of $D \cdot \tau_\alpha$. The results for both particle A and B along the y and z axes are plotted.

simple and easy to use. By contrast, equation 3.21 is more complicated, but also very useful. It associates the transport properties (η), the dynamic quantities (D), the temperature and the hydrodynamic diameter within one equation. Here we propose another definition of the so called ‘effective temperature’ by employing equation 3.21.

Bordat et al. addressed that the violation of Stokes-Einstein relation in supercooled liquids ($T_c < T < T_s$) is caused by the decrease of the hydrodynamic diameter when the temperature is lowered. For the ‘normal’ liquids ($T > T_s$), d equals the diameter of the particle, i.e. $d = \sigma_A$ for the particle A . In this case, the Stokes-Einstein relation is valid. The underlying reason is that SE relation is sensitive only to the positional fluctuation of immobile particles. For the particles trapped in the cage, the spatial fluctuation can be quantified by the cage size λ . Thus they found d was almost equal to λ for particle A [4]. Based on this idea, the equation 3.21 can be written as,

$$D\eta = \frac{k_B T}{b\pi\lambda} . \quad (3.23)$$

On the other hand, the temperature can be estimated if the mean square displacement and the viscosity for the supercooled system are known. Suppose this statement is still valid for the effective temperature in

the driven system. Then a new definition of the effective temperature can be written as,

$$T_{eff} = \frac{b\pi D\eta\lambda}{k_B} , \quad (3.24)$$

where the diffusion coefficient D , and the cage size λ can be evaluated from the mean square displacement, η is the viscosity. Actually, the λ gotten from the MSD is slightly larger than the hydrodynamic diameter d , especially for the particle B [4]. This may be caused by the fact that the mean square displacement is an average of all A particles or all B particles, including both immobile and mobile particles. As a consequence, the contribution from mobile particles makes λ larger than the really cage size. To correct the value of λ , we can use a criterion to select immobile particles, and calculate the mean square displacement for them, then the ‘true’ cage size can be estimated. Finally, the effective temperature of the driven system can be calculated via equation 3.24.

The Stokes-Einstein relation is discussed in this section. At the lower temperatures ($T < 0.2$), the Stokes-Einstein relation is satisfied with the aid of the shear. In contrast, in the supercooled region ($T_c < T < T_s$), the deviation from the Stokes-Einstein relation is observed, which can be regarded as an evidence that the dynamics of the system is spatially heterogeneous. In the next section, we will use the self-part of the van Hove function to continue the discussion on dynamic heterogeneity. At last, we proposed another definition of the effective temperature based on the Stokes-Einstein relation. The research on this subject is still undergoing.

3.4.6 Van Hove function

We will devote the rest of this chapter to investigating the self-part of the van Hove function. Van Hove function $G(\mathbf{r}, \mathbf{r}', t)$ is a time dependent density-density correlation function [14], which has the formula,

$$G(\mathbf{r}, \mathbf{r}', t) = \frac{1}{N} \langle \rho(\mathbf{r}' + \mathbf{r}, t) \rho(\mathbf{r}', 0) \rangle . \quad (3.25)$$

Integrating over the initial position \mathbf{r}' , equation 3.25 can be simplified as,

$$G(\mathbf{r}, t) = \frac{1}{N} \left\langle \sum_{i=1}^N \sum_{j=1}^N \delta[\mathbf{r} + \mathbf{r}_j(0) - \mathbf{r}_i(t)] \right\rangle . \quad (3.26)$$

$G(r, t)$ can be separated into two parts, the ‘self’ part, and the ‘distinct’ part, which are labeled by the subscript s and d respectively,

$$G(\mathbf{r}, t) = G_s(\mathbf{r}, t) + G_d(\mathbf{r}, t) , \quad (3.27)$$

where $G_s(\mathbf{r}, t)$ and $G_d(\mathbf{r}, t)$ are defined as,

$$G_s(\mathbf{r}, t) = \frac{1}{N} \left\langle \sum_{i=1}^N \delta[\mathbf{r} + \mathbf{r}_i(0) - \mathbf{r}_i(t)] \right\rangle, \quad (3.28)$$

$$G_d(\mathbf{r}, t) = \frac{1}{N} \left\langle \sum_{i=1}^N \sum_{j \neq i}^N \delta[\mathbf{r} + \mathbf{r}_j(0) - \mathbf{r}_i(t)] \right\rangle. \quad (3.29)$$

The self part of the van Hove function measures the probability distribution of a single particle displacement [27] and has been extensively utilized to characterize dynamic heterogeneity in experiments [19, 28, 29, 30], where they took snapshots of the system at fixed time interval by the confocal fluorescence microscopy, extracted the positions of all the particles from the images and calculated $G_s(r, t)$ with those trajectories. The self-part of the van Hove function is also a powerful tool in simulations [27, 31, 32] to study the dynamic behavior of the system. Chaudhuri et al. [31] pointed out that for supercooled liquids, at short and intermediate time, the shape of the self-part of the van Hove function can be separated into two parts. The center part in $G_s(r, t)$ is quasi-Gaussian, which corresponds to the particles trapped in the ‘cage’ formed by their neighbors. Most of the particles in the system belong to this kind, and they vibrate around their initial positions. On the other hand, mobile particles contribute to the broad exponential tails. Each mobile particle may perform several ‘jumps’ in a small time to move to other positions. This ‘jump’ is regarded as a cooperative rearrangement, which involves many particles (both mobile and immobile ones) [33].

According to equation 3.28, the self-part of the van Hove function is calculated at different time, from $0.1\tau_\alpha$ where the plateau is evident in both the mean square displacement and the self-intermediate scattering function, corresponding to the situation that most particles are trapped in the cage formed by their neighbors, to $100\tau_\alpha$ where the long-time diffusion of particles occurs. The self-part of the van Hove function along the velocity gradient direction \hat{e}_y of the system at different time for the temperature $T = 0.6$ are plotted in the linear-logarithmic scale. Figure 3.15 shows the evolution of the $G_s(r, t)$ and the fitting are presented in figure 3.16. Figure 3.17 and 3.18 do the same thing for the lowest temperature $T = 0.0$. The distribution functions of the single particle displacement along the vorticity direction at various times are found almost the same as those along y direction for all the temperatures we studied, hence they are not plotted.

Basically, figure 3.15 and 3.17 show that at very short time $t = 0.1\tau_\alpha$, $G_s(r, t)$ is very narrow and high, exhibiting the fact that most of the particles only have a very small amount of moving during this time. As the time goes on, the height of $G_s(r, t)$ drops, the shape becomes broad, which means many particles have moved with a longer distance, and corresponding to the large mean square displacement at large t .

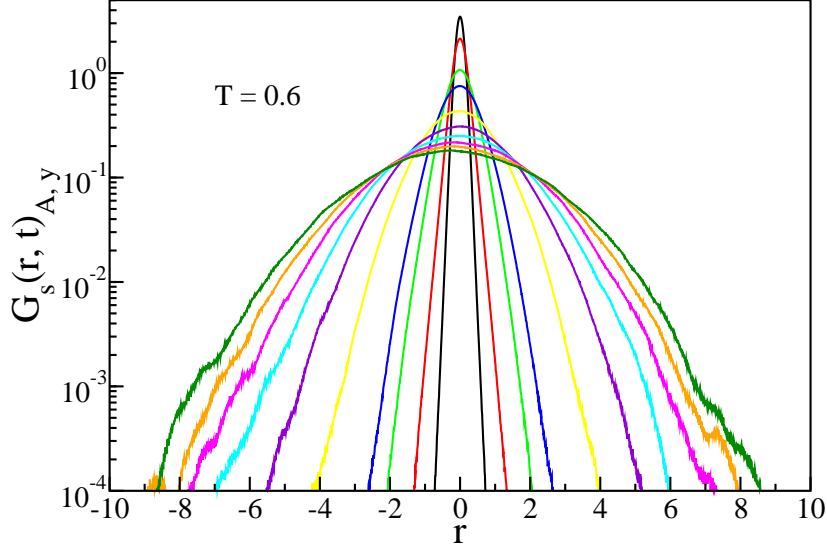


Figure 3.15: The van-Hove function of the large particle A at different times along the velocity gradient direction \hat{e}_y with temperature $T = 0.6$. From top to bottom the times are $t = 0.1\tau_\alpha, \tau_\alpha, 5\tau_\alpha, 10\tau_\alpha, 30\tau_\alpha, 60\tau_\alpha, 90\tau_\alpha, 120\tau_\alpha, 150\tau_\alpha, 180\tau_\alpha$. The α -relaxation time for $T = 0.6$ is $\tau_\alpha = 2.8$.

To find more information about the dynamic behavior, the center of the self-part of the van Hove function is fitted by Gaussian function,

$$G_s(r, t) = A(t) \exp[-B(t)r^2] , \quad (3.30)$$

where A and B are fitting parameters. The tails in $G_s(r, t)$ can be described by the exponential function,

$$G_s(r, t) \propto \exp(-|r|/C(t)) , \quad (3.31)$$

where $C(t)$ is a fitting parameter.

Figure 3.16 shows that at $t = 0.1\tau_\alpha$, only a very small part at the center of $G_s(r)$ can be fitted by the Gaussian function. As we have explained at the beginning of this subsection, the Gaussian distribution part in the $G_s(r, t)$ corresponds to immobile particles vibrating in the cage formed by their neighbors. For about $|r| > 0.1$, the tails of $G_s(r, t)$ are very broad, and can be fitted by the exponential function. The exponential tails show the existence of the mobile particles. As a consequence, dynamic heterogeneity can be observed from the $G_s(r, t)$ in our system. As time gets longer, the Gaussian part at the center grows, and the exponential tails become smaller. At $t = 50\tau_\alpha$, the self-part of the van Hove function follows the

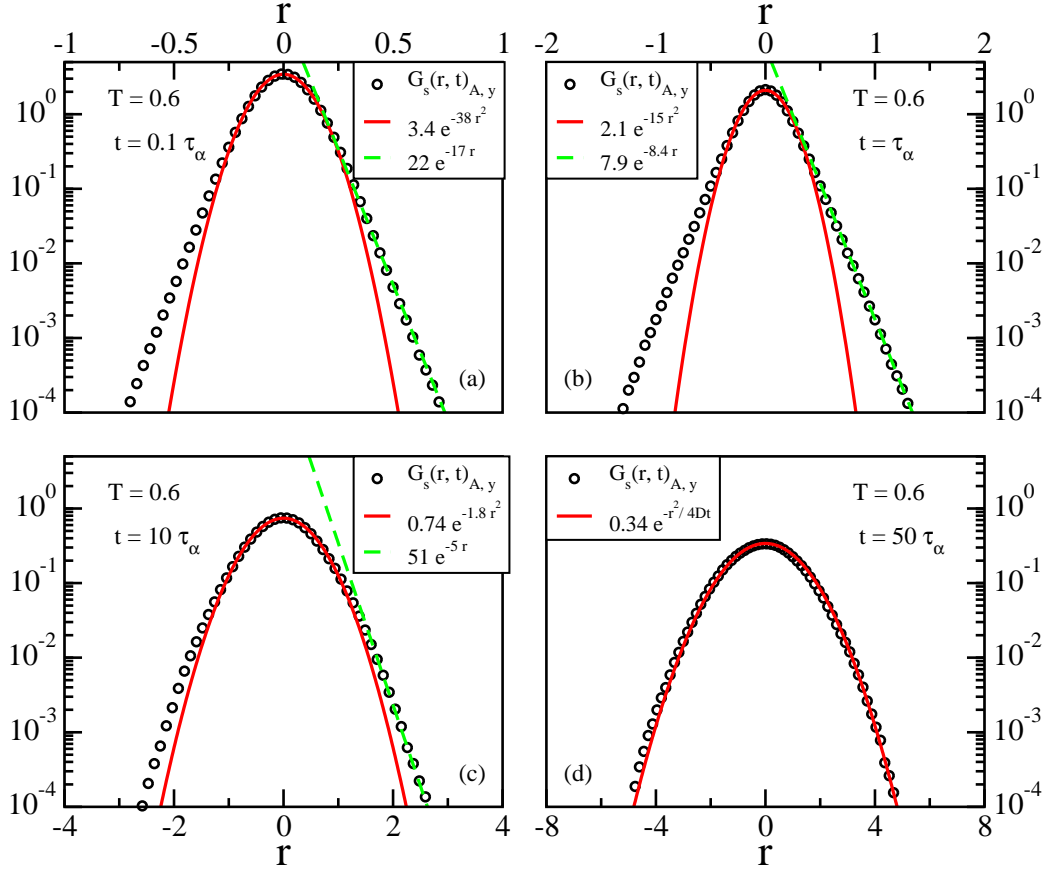


Figure 3.16: The van-Hove function of the particle A along y direction at different times $0.1\tau_\alpha$, τ_α , $10\tau_\alpha$, and $50\tau_\alpha$ are plotted and fitted. The α -relaxation time for $T = 0.6$ is $\tau_\alpha = 2.8$. The central part of $G_s(r, t)$ is fitted by the Gaussian function, and the broad tail is fitted by an exponential function. The fitting parameters are listed in the figure.

Gaussian equation in the entire range of r , the crossover to Fickian behavior is seen clearly [33]. The fitting parameter $B(t)$ in equation 3.30 is found equal to $1/4DT$, where D is the long-time diffusion coefficient obtained from the mean square displacement [33]. Thus when time is longer than $50\tau_\alpha$, the self-part of the van Hove function can be described by the Gaussian function,

$$G_s(r, t) \propto \exp[-r^2/(4Dt)] . \quad (3.32)$$

Our goal here is to figure out the influence of the imposed shear on the dynamic heterogeneous behavior of the system. With this purpose, the self-part of the van Hove function for the system at lower temperature (T is below T_c) needs to be investigated, since from the discussion we made before, the shear rate plays a dominant role in the dynamics and the effect of the bath temperature is weak in this range of temperature. Figure 3.18 shows that at $t = 0.1\tau_\alpha$ the Gaussian part is smaller than that for the temperature $T = 0.6$. The

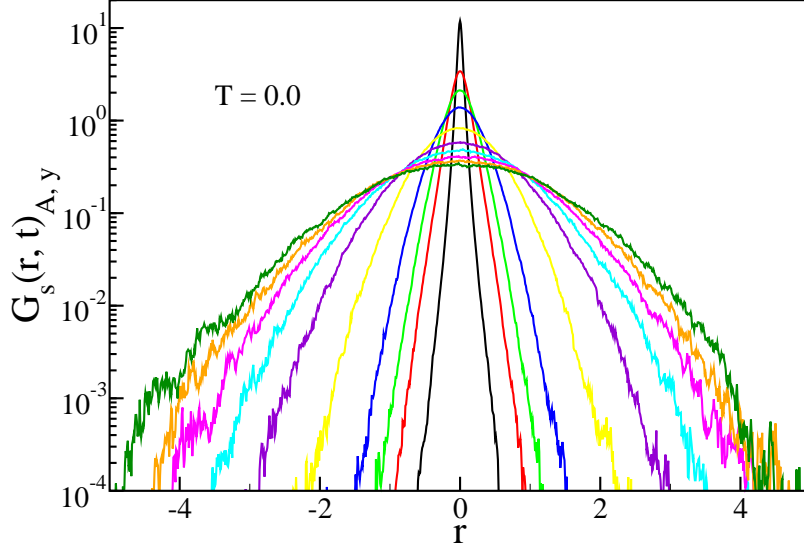


Figure 3.17: The van-Hove function of the large particle A at different times along the velocity gradient direction \hat{e}_y with temperature $T = 0.0$. From top to bottom the times are $t = 0.1\tau_\alpha, 0.5\tau_\alpha, \tau_\alpha, 2\tau_\alpha, 5\tau_\alpha, 10\tau_\alpha, 15\tau_\alpha, 20\tau_\alpha, 25\tau_\alpha, 30\tau_\alpha$. The α -relaxation time for $T = 0.0$ is $\tau_\alpha = 17.0$.

broad tails are exponential, and the dynamics at this time is spatially heterogeneous. As time goes on, the Gaussian part at the center expands, and the exponential tails become smaller. At $t = \tau_\alpha$, $G_s(r)$ is already very close to the Gaussian distribution. Finally at $t = 10\tau_\alpha$, $G_s(r)$ becomes Gaussian in the whole range of r , and it can be fitted by equation 3.32. Remember that for $T = 0.6$, the Fickian diffusion is recovered around $t = 50\tau_\alpha$. Although the actual times are close, ($10\tau_\alpha = 170$ for $T = 0.0$, and $t = 50\tau_\alpha = 140$ for $T = 0.6$), it still can be said that the shear tends to restore the Fickian behavior. To make a rigorous conclusion, the system needs to be investigated under various shear rates.

In this section, we analyzed the self-part of the van Hove function of the system at various times. Dynamic heterogeneity are observed at short and intermedial time for all the temperature we investigated. At longer time, the Fickian diffusion is restored. At lower temperature $T < T_c$, shear has a strong influence on the dynamics and tends to suppress heterogeneous behavior.

3.5 Discussion

In this chapter, we simulated the Kob-Andersen binary Lennard-Jones mixture at various temperature. With the aid of the impose shear, the system at the temperatures below T_c can be studied. Both the static

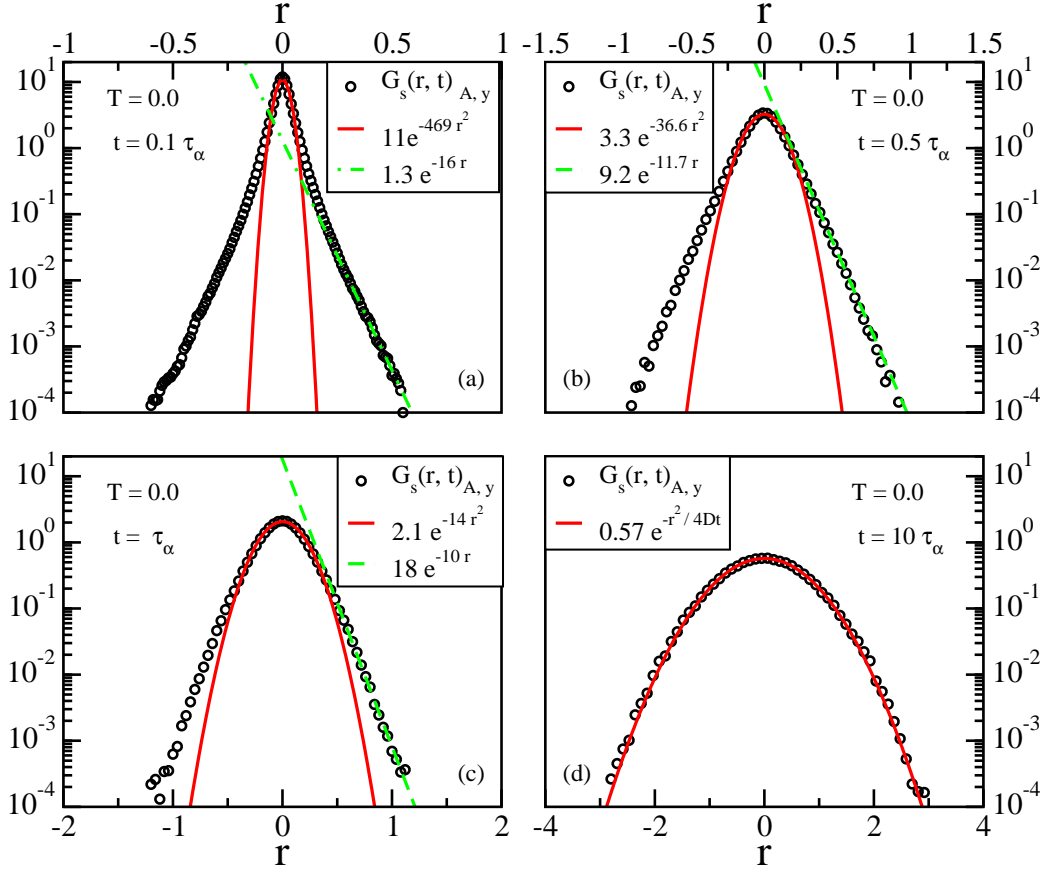


Figure 3.18: The van-Hove function of the particle A along y direction at different times $0.1\tau_\alpha$, $0.5\tau_\alpha$, τ_α , and $10\tau_\alpha$ are plotted and fitted. The α -relaxation time for $T = 0.0$ is $\tau_\alpha = 17.0$. The central part of $G_s(r, t)$ is fitted by the Gaussian function, and the broad tail is fitted by an exponential function. The fitting parameters are listed in the figure.

behavior and dynamic manner of the system have been analyzed. In the supercooled region (temperature is above T_c), the effect of the shear on the static structure of the liquid is limited. For the sheared glass ($T < T_c$), the anisotropic phenomenon does appear in $g_+(r)$ and $S(k)$.

On the other hand shear has a strong influence on dynamic behavior, especially when the temperature is below T_c . In this range, the imposed shear plays the primary role in the dynamics of the system. The cage effect is stopped by the shear at long time, as a result, the diffusive motion of the particles is recovered with a non-zero diffusion coefficient. The structural relaxation time is dramatically reduced, and the anisotropy is observed from the τ_α . What is more, the Stokes-Einstein relation is restored by the imposed shear. From the self-part of the van Hove function, we found that shear also tends to drive the dynamics back into Fickian behavior. When the temperature is higher than T_c , the effects of the shear on the dynamics of the liquid are eliminated by the increasing temperature. The dynamics of system is controlled primarily by temperature, and the shear can be regarded as a perturbation.

Both the bath temperature and the shear affect the static and dynamic behavior of the system. Thus it is naturally to define a new quantity, the so called ‘effective temperature’, which is a function of T and $\dot{\gamma}$, and quantify the combined effects of the bath temperature and the shear on the system. In this chapter, we proposed three definitions of the effective temperature. The first two are based on the mode-coupling theory, and the third one is according to the Stokes-Einstein relation. We calculated the effective temperatures with the first two definitions, and found they give very good agreement.

As we discussed before, the study of binary Lennard-Jones particles under shear by Brownian dynamics simulation is far from completeness. There are several aspects that can be investigated in the future. First of all, to figure out how the imposed shear affects the static and dynamic behavior of the system. Many other shear rates need to be introduced for this KA binary LJ mixture. By varying the shear rate, the dependence of the diffusion coefficient D , relaxation time τ_α , the viscosity η , and the effective temperature T_{eff} on the shear rate $\dot{\gamma}$ can be investigated. Second, more temperatures between $T = 0.2$ and $T = 0.4$ will be studied, since some evidences show that T_c may not be necessarily equal to 0.435 [9]. In our work, for instance, the Stokes-Einstein relation is valid in the range $0.0 \leq T \leq 0.2$, a deviation is observed at $T = 0.4$. Third, the definition of the effective temperature based on the Stokes-Einstein relation needs to be examined. Some other physical properties may be employed to test the validity of the effective temperatures. Finally, the crossover from the non-Gaussian distribution to the Gaussian behavior in the self-part of the van Hove function will be studied. Chaudhuri et al. have used the continuous time random walk (CTRW) model to build a uniform equation which can fit the self-part of the van Hove function in the whole range of the time [33, 34]. It may be interesting to use this equation in our system, and to figure out the microscopic dynamics under shear.

Bibliography

- [1] W. Kob and H. C. Andersen, *Phys. Rev. E* 51, 4626 (1995).
- [2] W. Kob and H. C. Andersen, *Phys. Rev. E* 52, 4134 (1995).
- [3] T. A. Weber and F. H. Stillinger, *Phys. Rev. B* 31, 1954 (1985).
- [4] P. Bordat, F. Affouard, M. Descamps, and F. M^uller-Plathe, *J. Phys.: Condens. Matter* 15, 5397 (2003).
- [5] S. K. Kumar, G. Szamel, and J. F. Douglas, *J. Chem. Phys.* 124, 214501 (2006).
- [6] Y. Jung, J. P. Garrahan, and D. Chandler, *Phys. Rev. E* 69, 061205 (2004).
- [7] J. D. Eaves and D. R. Reichman, *PNAS*, 106, 15171 (2009).
- [8] G. Szamel and E. Flenner, *Europhys. Lett.* 67, 779 (2004).
- [9] E. Flenner and G. Szamel, *Phys. Rev. E* 72, 011205 (2005).
- [10] F. Varnik, *J. Chem. Phys.* 125, 164514 (2006).
- [11] F. Varnik, *AIP Conf. Proc.* 982, 160 (2008).
- [12] P. Gallo, A. Attili and M. Rovere, *Phys. Rev. E* 80, 061502 (2009).
- [13] P. Gallo, A. Attili and M. Rovere, *J. Phys.: Condens. Matter* 23, 234118 (2011).
- [14] J. -P. Hansen and I. R. McDonald, *Theory of simple liquids (2nd edition)*.
- [15] H. Touba and G. A. Mansoori, *International Journal of Thermophysics*, 18, 1217 (1997).
- [16] S. Hess and H.J.M Hanley, *Phys. Rev. A* 25, 1801 (1982).
- [17] A. Latz, *J. Phys. Condens. Matter* 12, 6353 (2000).
- [18] W. Kob, and H. Andersen, *Phys. Rev. Lett.* 73, 1376 (1994).
- [19] C. Eisenmann, C. Kim, J. Mattsson, and D. A. Weitz, *Phys. Rev. Lett.* 104, 035502 (2010).
- [20] L. Berthier and G. Tarjus, *Phys. Rev. E* 82, 031502 (2010).
- [21] G. Tarjus and D. Kivelson, *J. Chem. Phys.* 103, 3071 (1995).

- [22] F. Mallamace, C. Branca, C. Corsaro, N. Leone, J. Spooren, H. E. Stanley, and S-H. Chen, *J. Phys. Chem. B* *114*, 1870 (2010).
- [23] S. M. Chathoth and K. Samwer, *Appl. Phys. Lett.* *97*, 221910 (2010).
- [24] N. P. Lazarev, A. S. Bakai, C. Abromeit, *J. Non-Crystalline Solid.* *353*, 3332 (2007).
- [25] X. J. Han and H. R. Schober, *Phys. Rev. B* *83*, 224201 (2011).
- [26] M. D. Ediger, *Annu. Rev. Phys. Chem.* *51*, 99 (2000).
- [27] D. E. Masri, L. Berthier, and L. Cipelletti, *Phys. Rev. E* *82*, 031503 (2010).
- [28] Y. Gao and M. L. Kilfoil, *Phys. Rev. Lett.* *99*, 078301 (2007).
- [29] P. Chaudhuri, Y. Gao, L. Berthier, M. Kilfoil, and W. Kob, *J. Phys.: Condens. Matter* *20*, 244126 (2008).
- [30] , B. Wang, S. M. Anthony, S. C. Bae, and S. Granick, *PNAS*, *106*, 15160 (2009).
- [31] P. Chaudhuri, S. Sastry, and W. Kob, *Phys. Rev. Lett.* *101*, 190601 (2008).
- [32] R. K. Darst, D. R. Reichman, and G. Biroli, *J. Chem. Phys.* *132*, 044510 (2010).
- [33] P. Chaudhuri, L. Berthier, and W. Kob, *Phys. Rev. Lett.* *99*, 060604 (2007).
- [34] E. W. Montroll and G. H. Weiss, *J. Math Phys.* *6*, 167 (1965).

Chapter 4

Dynamic heterogeneity and dynamic correlation length in a hard-sphere glass former

4.1 Introduction

Some results discussed in this chapter can also be found in the article [1].

In the previous chapter, we have mentioned that in the supercooled regime the dynamics change remarkably as the liquids approach the glass transition. For instance, the relaxation time and viscosity typically increase by about 14 orders of magnitude from the freezing temperature to the glass transition point [2]. Despite the obvious evolution in dynamic behavior, the static structure hardly changes when the system is cooled or compressed to approach the glass transition point [3, 4, 5]. It is even more interesting that dynamic heterogeneity has been observed in supercooled liquids, via experiments [6, 7, 8, 9], computer simulations [10, 11, 12] and also been studied theoretically [4, 13]. It is commonly accepted that dynamic heterogeneity is a characteristic feature of glass formers and can help to explain many anomalous phenomena, such as the Stokes-Einstein breakdown and the non-exponential structural relaxation [4, 5, 14].

We showed in the preceding chapter that the heterogeneous dynamics can be revealed from the self-part of the van Hove function. In the supercooled regime the exponential tails in $G_s(r, t)$ emerge and become broad, which implies that dynamic heterogeneity grows when the system approaches the glass transition [15]. Although the self-part of the van Hove function indeed indicates a growth of dynamic heterogeneity, it is somehow indirectly. In the recent decade, the multi-point dynamic susceptibility is intensively employed to quantify the strength of dynamic heterogeneity in the supercooled system [5, 16, 17, 18].

In glass-forming liquids, the motion of the particles in the local region (the size is about 5 to 20 molecular diameters [3]) are cooperative. This correlated dynamics is supposed to be the underlying reason

that causes dynamic heterogeneity [17]. As mentioned above dynamic heterogeneity increases when the system approaches the glass transition. Consequently, the length scale of this ‘cooperatively-rearranging regions’ [17, 19] is also speculated to grow. However it has been demonstrated many times that the spatial correlation lengths are almost unchanged [5, 17]. The traditional two-point dynamic correlations, such as the intermediate scattering function, can give the structural relaxation time which may be regarded as the time scale of dynamic heterogeneity (we will discuss this latter), but fails to reveal the length scale. Fortunately, scientists found that the fluctuations of the dynamic correlators, namely the four-point correlation functions, are able to be related to the dynamic correlation length and measure the strength of dynamic heterogeneity [5, 17].

Berthier et al. [5] further pointed out that the four-point dynamic correlations depend on the statistical ensembles, because with different ensembles some of the global fluctuations are forbidden [1, 5]. For instance, they found the four-point susceptibility χ_4 for the NPT ensemble could be related to that for the NPH ensemble by,

$$\chi_4^{NPT}(\mathbf{r}, t) = \chi_4^{NPH}(\mathbf{r}, t) + \frac{1}{c_p} \left(\frac{\partial C_0(\mathbf{r}, t; T)}{\partial \ln T} \right)_P^2, \quad (4.1)$$

where c_p is the constant pressure specific heat and where $C_0(\mathbf{r}, t; T)$ is the dynamic two-point correlator. The physical meaning of this equation is that the fluctuation of the enthalpy is suppressed in the NPH ensemble [5]. Equation 4.1 can be generated in the following form [1, 18],

$$\chi_4(t) = \chi_4(t)|_x + \mathcal{X}(t). \quad (4.2)$$

In this equation, $\chi_4(t)|_x$ is the four-point susceptibility in the ensemble where the variable x cannot fluctuate. The contribution due to the fluctuation in x is included in the correction term $\mathcal{X}(t)$ [1, 18]. More importantly, $\chi_4(t)|_x$ cannot be measured by experiments, while $\mathcal{X}(t)$ can. Since $\chi_4(t)|_x$ is positive, $\mathcal{X}(t)$ gives the lower bound for $\chi_4(t)$ [3]. What is more, it has been found that $\mathcal{X}(t)$ grows faster than $\chi_4(t)|_x$ and becomes dominant as the system is approaching the glass transition [20].

Flenner et al. investigated the binary hard-sphere mixture with Monte Carlo dynamical simulation [1, 18]. They started from the average overlap function $F_o(a, t) = \langle \sum_{i=1}^N w_i(a, t) \rangle / N$, where N was the total number of particles, the microscopic overlap function $w_i(a, t) = 1$ if the displacement of the particle i was smaller than a distance a after time t , otherwise it was zero. With taking the parameter $a = 0.3$, they found that the four-point susceptibilities, counting the contribution from the fluctuations of the volume fraction in, were consistent with those obtained by the extrapolation of the four-point structure factor to the wave vector

$q = 0$. They also confirmed that dynamic heterogeneity increased accompanying the growth of dynamic length scales when the system approaches the glass transition.

In this work, our interest is focused on the effects of the probed length scale ($\sim a$) on the quantities which can characterize the heterogeneous dynamic behavior of the system. This is not trivial. The wavevector dependence of the four-point susceptibility has been studied [16, 21], where the self-intermediate scattering function was used, and the wave vector played a role as the probed length scale ($\sim k^{-1}$). They found that the peak value of χ_4 increased with smaller k (longer probed length). On the other hand, Lačević et al. used a similar overlap function as the one we employed. They found a decrease in χ_4 with larger probed length scale ($\sim a$) when a was larger than 0.3 [17]. In this work we investigate the a -dependence of the two-point correlator F_o and the four-point dynamic correlations, i.e. χ_4 , $S_4(q)$, and so on. With these results we want to argue that to extract universal information about dynamic heterogeneity, such as dynamic length scales and time scales, a ‘measuring stick’ needs to be found.

This chapter is organized in this way. The simulation details will be introduced in the next section. After that we will analyze the results calculated from this simulation. The average overlap function $F_o(a, t)$, instead of the self-intermediate scattering function, will be measured first of all. Then the α -relaxation will be extracted from $F_o(a, t)$. The four-point susceptibility will be calculated at $\tau_\alpha(\phi, a)$ with allowing the fluctuations of all the conserved variables. After that, the four-point structure factor $S_4(q, \tau_\alpha(\phi, a))$ will be explored. The dynamic correlation length ξ is then evaluated from $S_4(q, \tau_\alpha(\phi, a))$ by the Ornstein-Zernicke fits. At last the four-point pair correlation function $G_4(r, \tau_\alpha(\phi, a))$ will be examined. This chapter will be ended with the section for discussion.

4.2 Simulation

Computer simulations are performed on a binary hard-sphere mixture introduced by Brambilla et al. [20]. The ratio of the numbers of particles between species A and B is 50 : 50; thus the concentration for each type of particle is $c = 0.5$. The diameter of the larger particles d_A is 1.4σ , for the smaller particles $d_B = 1.0\sigma$. This system has two advantages. First crystallization is avoided when the liquid is compressed [20]. Secondly, with this system the dynamical quantities generated via numerical simulations, such as the self-intermediate scattering function, are comparable with those obtained from the experiment [20].

The volume fractions ϕ of the system can be calculated by [1],

$$\phi = \pi(N_A d_A^3 + N_B d_B^3)/6V, \quad (4.3)$$

where V is the volume of the system, N_A and where N_B are the number of particles for species A and B , respectively. The total number of particles N in our system is 80 000. The quite large system is used to extract the more precise dynamic correlation length [22]. The finite-size effect emerging in the four-point susceptibility has been observed [23]. To explore the behavior of liquids approaching the glass transition, the systems were simulated with $\phi = 0.4, 0.45, 0.5, 0.52, 0.55, 0.56, 0.57, 0.58, 0.59$. To study the effects of the fluctuation of the volume fraction on the four-point susceptibility χ_4 , the systems with volume fractions $\phi \pm \delta\phi$ were also explored. For $\phi \leq 0.58$, $\delta\phi = 0.001$, and for $\phi \geq 0.585$, $\delta\phi = 0.0005$. Similarly, to consider the fluctuation of the concentrations, the systems with $c = 0.5 \pm 0.05$ were also simulated for $\phi \leq 0.58$. This was not be done for larger volume fraction, because we will show later that the contribution to χ_4 from the term containing the derivative respect to c can be neglected.

The systems were simulated via a standard Monte Carlo (MC) algorithm proposed by Berthier et al. [24] where they argued the MC simulation was the most efficient method compared with the Brownian dynamics and stochastic dynamics approaches. Most importantly, the dynamic properties obtained via the MC methods agree very well with those extracted from the stochastic dynamics simulation [24]. The simulation details are as follows. In every Monte Carlo step, there are N attempts. With each attempt, a particle is chosen randomly, and shifted to a random distance within a cubic box centered at its original position. The length of the box is 0.1σ [20].

For every volume fraction the simulation was performed on 4 to 8 independent samples. After the aging stopped, the production runs lasted at least $100\tau_\alpha$. (This τ_α is the α -relaxation time with $a = 0.3$, where a is the probed length scale, see equation 4.4.) With the trajectories produced from the simulations, the physical quantities such as the overlap function, the four-point susceptibility etc. are measured for each sample, then the averages and errors are calculated over all these runs. All the quantities are expressed with the reduced units, specifically, the unit of length is σ , the time is given in the unit of the Monte Carlo step. The trajectories were generated by Szamel and Flenner, the author did part of the analysis [1].

4.3 Results

4.3.1 Overlap function

The intermediate scattering function $F_s(k, t)$ is often utilized to characterize the dynamics of liquids [21, 25, 26]. The wave vector k is usually set to be the k_{max} , at which the static structure factor reach its maximum value. With the studies of the k dependence of $F_s(k, t)$ for various models, the common trend has been found that for supercooled liquids, the height of the plateau, which can be explained by the ‘cage’ effect,

increases and τ_α becomes longer [21, 25, 26]. The four-point susceptibility related to the self-intermediate scattering function has been explored largely to investigate the correlated dynamic behavior [5, 21, 27]. The influence of the probed length scale ($\sim k^{-1}$) on $\chi_4(k, t)$ has been discussed by Chandler et al. [21].

In this work we use a different quantity first proposed by Lačević et al. [17] to study the dynamic behavior of the system. First, let us define the microscopic overlap function $w_i(a, t)$ by the formula,

$$w_i(a, t) = \Theta[a - |\mathbf{r}_i(t) - \mathbf{r}_i(0)|] . \quad (4.4)$$

In this equation, $r_i(t)$ is the position of the particle i at time t . $\Theta(x)$ is the Heaviside step function [18]. If the particle does not move further than a distance a from its original position after time t , $w_i(a, t) = 1$, otherwise it equals 0. Here we pick the self-part of the overlap function w_{ij} in [17]. With $w_i(t)$ the number of particles that stay within a distance a from their original positions during the time interval t can be expressed by,

$$N_s(a, t) = \sum_{i=1}^N w_i(a, t) . \quad (4.5)$$

Then the average overlap function can be written down [1],

$$F_o(a, t) = \frac{1}{N} \left\langle \sum_{i=1}^N w_i(a, t) \right\rangle = \frac{1}{N} \langle N_s(a, t) \rangle . \quad (4.6)$$

In this average overlap function the parameter a plays a role as the probed length scale, and $F_o(a, t)$ can be expressed as the Fourier transform of the self-intermediate scattering function [21],

$$F_o(a, t) = (2\pi)^{-d} \int_{|\mathbf{r}| < a} d^d \mathbf{r} \int d^d \mathbf{k} e^{-i\mathbf{k} \cdot \mathbf{r}} F_s(k, t) , \quad (4.7)$$

where d is the dimensionality.

To illustrate that the average overlap function is a good alternative of the self intermediate scattering function to explore the dynamics of the system, figure 4.1 is quoted [1] to show that $F_o(t)$ exhibits similar shape as $F_s(k, t)$ with increasing volume fraction. As the system approaches glass transition (higher ϕ), the two step relaxation predicted by the mode-coupling theory appears [25]. At early time, it is the β -relaxation regime, followed by a plateau, then $F_o(a, t)$ decays to zero in the α -relaxation regime. The α -relaxation can be fitted by a stretched exponential function [1],

$$f(t) = \exp[-(t/\tau_\alpha)^\beta] , \quad (4.8)$$

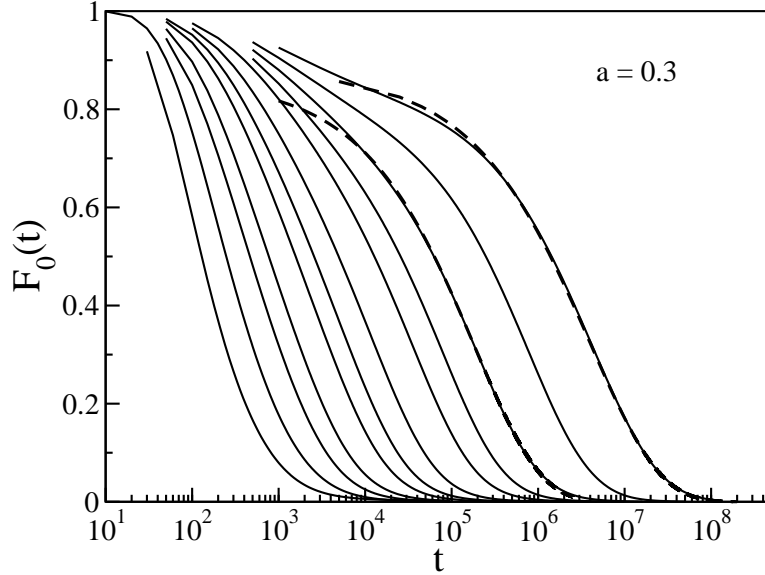


Figure 4.1: The average overlap function versus time. The volume fractions are $\phi = 0.4, 0.45, 0.5, 0.52, 0.54, 0.55, 0.56, 0.57, 0.575, 0.58, 0.585, 0.59$ from the left to the right side. The parameter a in the microscopic overlap function is set to be 0.3. The dashed lines are stretched exponentials which are expressed by equation 4.8. For $\phi = 0.58$, $\beta = 0.56$, and for $\phi = 0.59$, $\beta = 0.54$. The figure is taken from reference [1].

where τ_α is the α -relaxation time, at which $F_o(a, t) = e^{-1}$. The fitting parameter β is positive and close to 1 for small volume fraction, and decreases with increasing ϕ , which is accepted as an appearance of growth of dynamic heterogeneity [1]. On careful inspection of figure 4.1 $F_o(a = 0.3, t)$ indeed contains similar information as the self-intermediate scattering function with $k = k_{max}$ and can be employed to investigate the heterogeneous dynamics of supercooled system.

Next we will show that the parameter a plays a very similar role as the probed length scale ($\sim k^{-1}$) does for $F_s(k, t)$. The overlap functions for a representative volume fraction $\phi = 0.57$ with various a are plotted in figure 4.2. When the parameter a grows, it needs more time for the particles to move further than a distance a from their original position. This can be seen from the figure that $F_o(a, t)$ deviates from unity after longer time. It is also observed that the β -relaxation regime shrinks and vanishes finally, meanwhile, the α -relaxation becomes more exponential (β in equation 4.8 grows to 1), which implies the crossover from dynamic heterogeneity to homogeneity with increasing a . It is not surprising because the hydrodynamic regime would be reached for large a , where the local correlated motions are gradually averaged out, which cause the decrease of dynamic heterogeneity [16]. Similar phenomenon for $F_s(k, t)$ with reducing wave vector has been observed and discussed [16, 21].

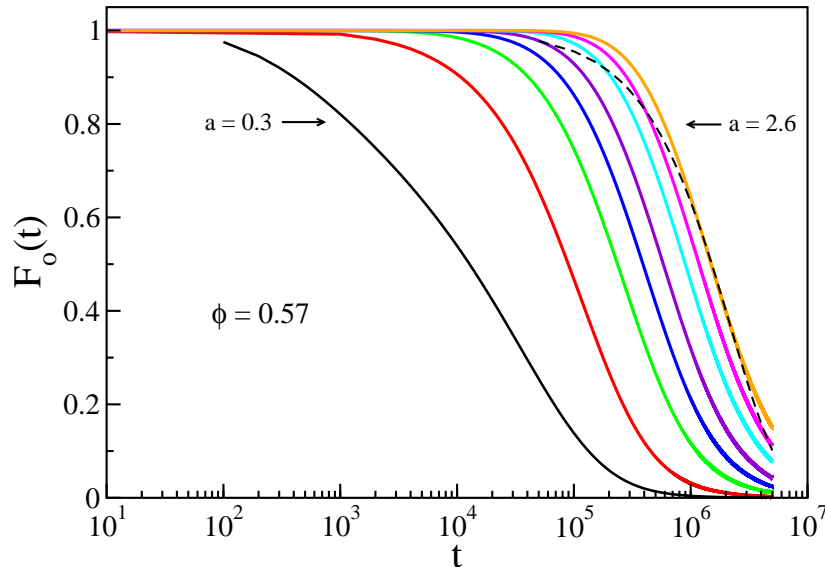


Figure 4.2: The average overlap function at the volume fraction $\phi = 0.57$ with various a , which are $a = 0.3, 0.6, 1.0, 1.3, 1.6, 2.0, 2.3, 2.6$ from the left to the right side. The dashed line is the exponential fit $\exp[-(t/\tau_\alpha(\phi, a))]$ for $a = 2.6$.

In this part, the average overlap function was calculated and studied at different volume fractions and various parameters a . At $a = 0.3$ the dynamic heterogeneous behavior is observed when the system is highly compressed. With larger probed length scale ($\sim a$), a crossover to homogeneous dynamics merges in $F_o(a, t)$.

4.3.2 Structural relaxation time

In supercooled liquids, the dynamics in one region may exhibit large difference from the dynamics in other regions. This phenomenon is called dynamic heterogeneity which we have introduced before. It should be stressed that the dynamics will change after some time. A cluster with larger mobility will slow down and the ‘caged’ particles will move faster later on. The underlying reason is that the supercooled system is still ergodic [28, 29]. Then it is natural to ask how long the ‘mobility’ or ‘immobility’ of the particles would last. This quantity is referred as the lifetime of the heterogeneity τ_{dh} and has been measured experimentally [28]. Here the question is which quantity is larger, τ_{dh} or τ_α (the α relaxation time). Actually, this is still controversial [30]. Many investigations indicated that τ_{dh} is close to τ_α [28, 31]. Experiment done by Wang and Ediger [32] suggested that near T_g t_{dh} is much longer than t_α . It has been reported via simulations that the τ_{dh} is roughly equal to the τ_α for strong glass formers and increases more rapidly than τ_α for the fragile model approaching the glass transition [17, 31, 33]. It has to be emphasized that the τ_α here is the

typical α -relaxation time which evaluated from the intermediate scattering function with the wave vector k_{max} where the static structure factor is maximum. To the best of my knowledge, the general conclusion $\tau_{dh} \gg \tau_\alpha$ is still missing. Thus in many investigations, the α relaxation time is commonly used to investigate the dynamic heterogeneous behavior.

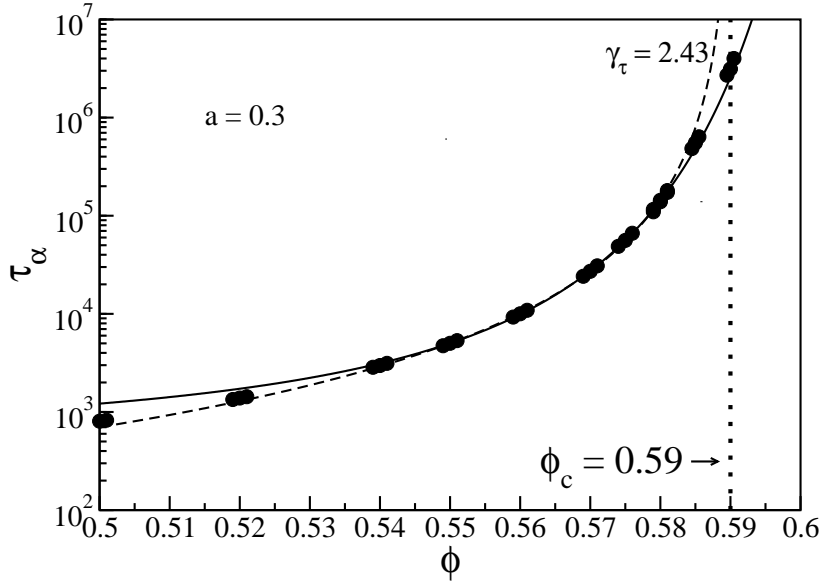


Figure 4.3: The α relaxation time τ_α extracted from the average overlap function is drawn versus the volume fraction ϕ . The dashed line shows the power law fit $a(\phi_c - \phi)^{-\gamma}$ which is predicted by the mode-coupling theory. The solid line is a fit with equation $\tau_\alpha \propto \exp[A/(\phi_0 - \phi)^2]$ which is proposed by Berthier and Witten [34]. The figure composed by Flenner [1] is revised and adopted.

Following the standard definition, the α relaxation time $\tau_\alpha(\phi, a)$ is extracted from the $1/e$ time of the decay of $F_o(\alpha, t)$. Before studying the a dependence of $\tau_\alpha(\phi, a)$, figure 4.3 is adopted from [1] to give a whole picture about the variation of the structural relaxation time for a system approaching the glass transition. From the figure, the α -relaxation time grows rapidly when the volume fraction is higher. Mode-coupling theory (MCT) predicts a power law formula for τ_α [1, 34],

$$\tau_\alpha(\phi) = C(\phi_c - \phi)^{-\gamma} , \quad (4.9)$$

In the equation, C and γ are fitting parameters, and ϕ_c , according to MCT, is the critical volume fraction at which the α -relaxation time diverges and the true glass transition happens. By fitting τ_α within the range $0.55 \leq \phi \leq 0.58$, γ and ϕ_c were found and are listed in the figure 4.3. It is necessary to point out that many numerical simulations have indicated that γ and ϕ_c are not unique, their values can be changed with

different fitting ranges. What is more, the divergence of $\tau_\alpha(\phi)$ is avoided at ϕ_c . Another mechanism beyond MCT may exist and can describe the evolution of τ_α in a better way, especially, when the system is really close to the glass transition [1, 10, 20].

Another formula usually used to fit the α -relaxation time is the generalized Vogel-Fulcher-Tamman (VFT) equation [1, 34],

$$\tau_\alpha(\phi) = \tau_0 \exp \left[\frac{A}{(\phi_0 - \phi)^\delta} \right]. \quad (4.10)$$

In the equation τ_0 and A are fitting parameters, δ is usually set to 1, and ϕ_0 is the critical volume fraction. Berthier et al. found that if δ is changed to be 2.2, the fit is better, more importantly, the corresponding ϕ_0 has larger value 0.635 which has higher possibility to be the critical volume fraction where the glass transition occurs [34]. Flenner et al. also got $\phi_0 = 0.635$ with choosing δ to be 2.0.

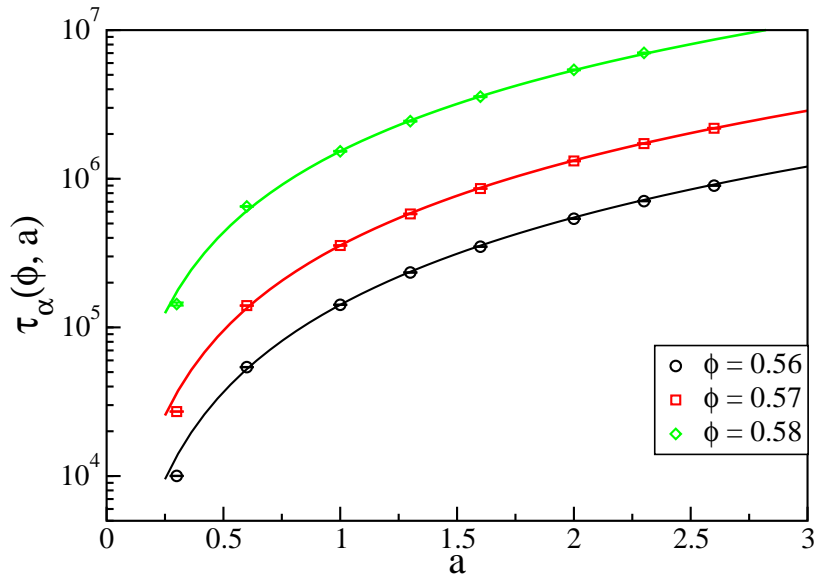


Figure 4.4: The α relaxation times τ_α extracted from the average overlap function are drawn versus the parameter a . At each volume fraction, the a -dependent of $\tau_\alpha(\phi, a)$ is fitted by the equation 4.11. The fitting parameter b is 1.95 for $\phi = 0.56$, 1.9 for $\phi = 0.57$, and 1.81 for $\phi = 0.58$, respectively.

The volume fraction dependence of the α -relaxation time has been reviewed in the above text, where the probed length scale a is taken to be 0.3. Now let us consider how the choice of alternative parameter a affects the structural relaxation time. To emphasize the a dependence, $\tau_\alpha(\phi)$ is promoted to $\tau_\alpha(\phi, a)$. Those relaxation times are evaluated from the overlap function with various ϕ and a , and plotted versus the parameter a in figure 4.4. It can be seen from the figure that the α -relaxation time increases monotonically

when larger a is selected. It is easy to understand, when the parameter a is bigger, it will take longer time for about 63% particles to move further than the distance a from their original positions. We found that for each volume fraction, $\tau_\alpha(\phi, a)$ can be fitted with a function of a ,

$$\tau_\alpha(\phi, a) = C(\phi)a^b, \quad (4.11)$$

where $C(\phi) = \tau_\alpha(\phi, a = 1.0)$ is a function of the volume fraction. The exponent $b \simeq 1.9$ is weakly dependent on ϕ . The values of b at each volume fraction are listed in the caption of figure 4.4. For $a \geq 0.6$ the fitting with equation 4.11 is perfect for every volume fraction. At $a = 0.3$ the fit seems to overestimate τ_α for all the three volume fraction we investigated. It is not clear if this implies that the fitting can only be performed for larger a . To solve this issue, the calculations will be done for a with various values around 0.3, and the a dependence of $\tau(\phi, a)$ at other volume fractions also needs to be studied in the future.

At the beginning of this part, we showed that at $a = 0.3$ the α -relaxation time can be fitted by the functions of ϕ (see, i.e. equation 4.9 4.10 and figure 4.3). It is natural to ask if τ_α has similar relations with the volume fraction for other choice of the parameter a . To answer this question, equation 4.11 is rewritten as,

$$\tau_\alpha(\phi, a) = \tau_\alpha(\phi, a = 0.3)(a/0.3)^b. \quad (4.12)$$

Since $\tau_\alpha(\phi, a = 0.3)$ can be fitted via equation 4.9 and 4.10, we speculate $\tau_\alpha(\phi, a)$ for other a values have the same volume fraction dependence if b is independent of ϕ . Unfortunately, so far we do not have enough data to examine this point. We will save this for the future investigation.

The a -dependence of the α -relaxation time has been investigated for $\phi = 0.56, 0.57,$ and 0.58 . For all of these volume fractions, the relation between $\tau_\alpha(\phi, a)$ and a has the form expressed as equation 4.11. Remember that the final aim is to find the time scale of dynamic heterogeneity which is obviously independent of the choice of parameter a . Thus only the α -relaxation time calculated at ‘certain’ a value may be regarded as the time scale that we are looking for. Besides, for various volume fraction, these ‘right’ a values are not necessary to be the same. To explain the reason, let us consider how to select the appropriate parameter a . First, all the particles, even those are trapped in the cage, vibrate around their positions [15], those vibrations are weakly cooperative. Thus a cannot be too small, otherwise those uncorrelated vibrations will be counted as the cooperative motions [17]. Secondly, if a is too large, the dynamic heterogeneous feature in the two-point correlators will be lost, as we have discussed for $F_o(a, t)$. The extracted α -relaxation time certainly cannot be regarded as the time scale for dynamic heterogeneity. Lačević et al. took $a = 0.3$ which is slightly larger than the square root of the height of the plateau in the mean square displacement, since

the distances that the particles can vibrate is smaller than the cage size [17]. The intensive simulations have shown that the height of the plateau decrease as the system approaches glass transition [1, 35, 36]. It is very possible that the specific parameter a we are looking for has the same situation.

Although many efforts have been devoted to researching the time scale of dynamic heterogeneity [31, 37, 38], how to define and calculate a common lifetime of dynamic heterogeneity is still an open question. Unlike the α relaxation time, the strength and the length scale of the heterogeneity seems to become independent of the choice of a , especially when a is quite large. The details will be discussed in the rests of this chapter.

4.3.3 Four-point susceptibility

When the volume fraction and density of the system are fixed, the fluctuation in the number of slow particles can be written as the variance of N_s ,

$$\chi_4(a, t)|_{\phi, c} = N^{-1}(\langle N_s^2(a, t) \rangle - \langle N_s(a, t) \rangle^2), \quad (4.13)$$

where the subscripts ϕ and c are used to underscore the fact that the volume fraction and concentration in this term are constant. This is because the simulational ensemble keeps numbers of both particles constant. [1]. The unit of $\chi_4(a, t)|_{\phi, c}$ is the number of particles. With considering the fluctuations in the volume fraction and concentration, the four-point susceptibility can be written as,

$$\begin{aligned} \chi_4(a, t) = & \chi_4(a, t)|_{\phi, c} + \chi_\phi^2(a, t)H_1 + \chi_\phi(a, t)\chi_c(a, t)H_2 + \chi_c^2(a, t)H_3 \\ & + F_o^2(a, t)H_4 + F_o(a, t)\chi_\phi(a, t)H_5 + F_o(a, t)\chi_c(a, t)H_6, \end{aligned} \quad (4.14)$$

where χ_ϕ and χ_c are the derivatives respect to the volume fraction and the concentration separately,

$$\chi_\phi = \partial F_o(a, t)/\partial \phi, \quad (4.15)$$

$$\chi_c = \partial F_o(a, t)/\partial c. \quad (4.16)$$

The expressions for the parameters H_1 to H_6 have been derived by Flenner and Szamel [1],

$$H_1 = \left(\frac{\pi\rho}{6}\right)^2 [d_A^6 c_A S_{AA} + 2d_A^3 d_B^3 \sqrt{c_A c_B} S_{AB} + d_B^6 c_B S_{BB}] , \quad (4.17)$$

$$H_2 = \frac{\pi\rho}{3} [d_A^3 c_A c_2 S_{AA} - d_A^3 c_A \sqrt{c_A c_B} S_{AB} + d_B^3 c_B \sqrt{c_A c_B} S_{AB} - d_A^3 c_A c_B S_{BB}] , \quad (4.18)$$

$$H_3 = c_B^2 c_A S_{AA} + 2c_A c_B \sqrt{c_A c_B} S_{AB} + c_A^2 c_B S_{BB} , \quad (4.19)$$

$$H_4 = d_A S_{AA} + 2\sqrt{c_A c_B} S_{AB} + c_B S_{BB} , \quad (4.20)$$

$$H_5 = \frac{\pi\rho}{3} [d_A^3 c_A S_{AA} + (d_A^3 + d_B^3) \sqrt{c_A c_B} S_{AB} + d_B^3 c_B S_{BB}] , \quad (4.21)$$

$$H_6 = 2[c_A c_B S_{AA} + (c_B - c_A) \sqrt{c_A c_B} S_{AB} - c_A c_B S_{BB}] . \quad (4.22)$$

In these equations, $S_{\alpha\beta}$ are the partial structure factors which have been extrapolated to $q = 0$, $c_\alpha = N_\alpha/N$ is the concentration of particle species α (α can be A or B).

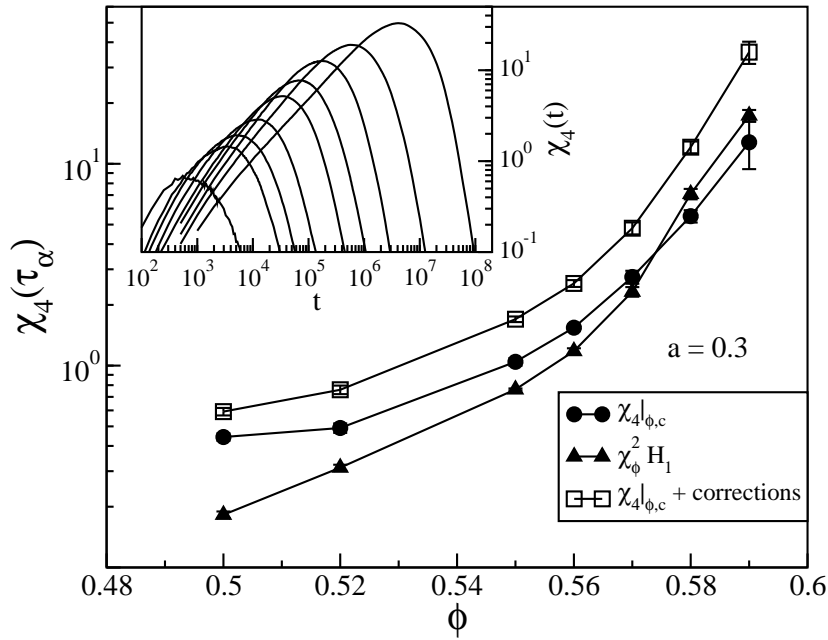


Figure 4.5: The dynamic susceptibility calculated via equation 4.14 versus the volume fraction at the structural relaxation time $\tau_\alpha(\phi, a)$. The first term $\chi_4(\tau_\alpha(\phi, a))|_{\phi,c}$ and second term $\chi_\phi^2(\tau_\alpha(\phi, a))H_1$ in equation 4.14 are also plotted. The insert figure shows the time evolution of χ_4 . The volume fraction increases from the left to the right side. The figure is adopted from reference [1].

For $a = 0.3$, the time evolution of all the terms in equation 4.14 has been carefully examined by Flenner et al. and the figure of the dynamic susceptibility is adopt from the article [1]. They found that in the α relaxation range, the contribution of the last five terms is so small that can be neglected. The first two terms grow from zero at the initial time and reach maximum around τ_α then decay to zero after that. Thus

the total value $\chi_4(t)$ calculated via equation 4.14 has the same trend (see the insert in figure 4.5). This kind of non-monotonic dependence of time have also been observed in other systems [5, 17, 21]. As the system approaches the glass transition, the peak value of χ_4^* becomes larger, which suggests the growth of correlation length [1, 22]. They further showed that the first term $\chi_4(t)|_{\phi,c}$ is larger when the volume fraction is smaller than 0.56, while for $\phi \geq 0.58$, the second one is bigger. However, in the whole range of ϕ that they researched, to calculate the maximum value χ_4^* , neither $\chi_4(t)|_{\phi,c}$ nor $\chi_\phi^2(t)H_1$ can be omitted.

The aim in this work is to check the influence of a on all the terms in equation 4.14 and also the total quantity χ_4 . The four-point susceptibilities at the structural relaxation time $\tau_\alpha(\phi, a)$ with various choice of a are calculated and plotted in figure 4.6. The first two terms $\chi_4(\tau_\alpha(\phi, a))|_{\phi,c}$ and $\chi_\phi^2(\tau_\alpha(\phi, a))H_1$ in equation 4.14 are also drawn in the same figure. The rest five correction terms are close to zero for all the combinations of ϕ and a we studied, thus are not shown in the figure.

As is shown in figure 4.6, for all the volume fractions, the first term $\chi_4(\tau_\alpha(\phi, a))|_{\phi,c}$ keeps decaying when the parameter a is larger. It is easy to understand, with increasing a , the α -relaxation time grows (see figure 4.4). At the large $\tau_\alpha(\phi, a)$, the system becomes homogeneous as we have discussed in the previous subsection. As a consequence, the fluctuation of the time correlation functions (i. e. $N_s(a, \tau_\alpha(\phi, a))$ in our case) will diminish. On the other hand, the second term $\chi_\phi^2(\tau_\alpha(\phi, a))H_1$ grows slightly with increasing of a and saturates around $a = 1.0$. For $\phi = 0.56$, $\chi_4(\tau_\alpha(\phi, c)) > \chi_\phi^2(\tau_\alpha(\phi, a))H_1$ at $a = 0.3$, while $\chi_\phi^2(\tau_\alpha(\phi, a))H_1$ becomes larger than $\chi_4(\tau_\alpha(\phi, c))$ at $a = 0.6$, and the difference increases with a . For bigger volume fraction $\phi = 0.57$ and 0.58 , $\chi_\phi^2(\tau_\alpha(\phi, a))H_1$ already contribute more to the total χ_4 than $\chi_4(\tau_\alpha(\phi, a))$ does at $a = 0.3$, and with larger a , $\chi_\phi^2(\tau_\alpha(\phi, a))H_1$ becomes even more dominant. Eventually, the total value $\chi_4(\tau_\alpha(\phi, a))$ is dominated by $\chi_\phi^2(\tau_\alpha(\phi, a))H_1$, and consequently the plateau emerges for $\chi_4(\tau_\alpha(\phi, a))$ in figure 4.6.

At first sight, our result for the probed length scale ($\sim a$) dependence of the four-point susceptibility is in contradiction with that reported by Lačević et al. [17]. They found that the peak value of $\chi_4(a, t)$ is largest around $a = 0.3$, while for $a < 0.3$, the maximum value of the $\chi_4(a, t)$ reduces with decreasing a , and for $a > 0.3$, this value goes down with increasing a (refer to Figure 22 in [17]). Carefully comparing the procedures to calculate χ_4 in both cases, we found the difference between our results and theirs may originate from the fact that they did not include the contribution of the fluctuations of the conserved variables (e.g. $\chi_T(t) = \partial Q(t)/\partial T$ in their case). Figure 4.6 shows that $\chi_4(\tau_\alpha(\phi, a))|_{\phi,c}$ does reduce as a increases, which is consistent with the tendency of the four-point susceptibility calculated by Lačević et al. [17].

A comparison is also drawn between our results and that reported by Berthier et al. [16]. They claimed that the peak of $\chi_\phi(k, t)$ grows when the wave vector k is decreased. In our case, a increase in $\chi_\phi^2(\tau_\alpha(\phi, a))H_1$ is indeed observed for $a \leq 1.0$, while it remains constant for larger a . To explain the difference, the first reason one may have in mind is that $\chi_\phi(\tau_\alpha(\phi, a))$ is actually not the maximum of $\chi_\phi(a, t)$, in other words,

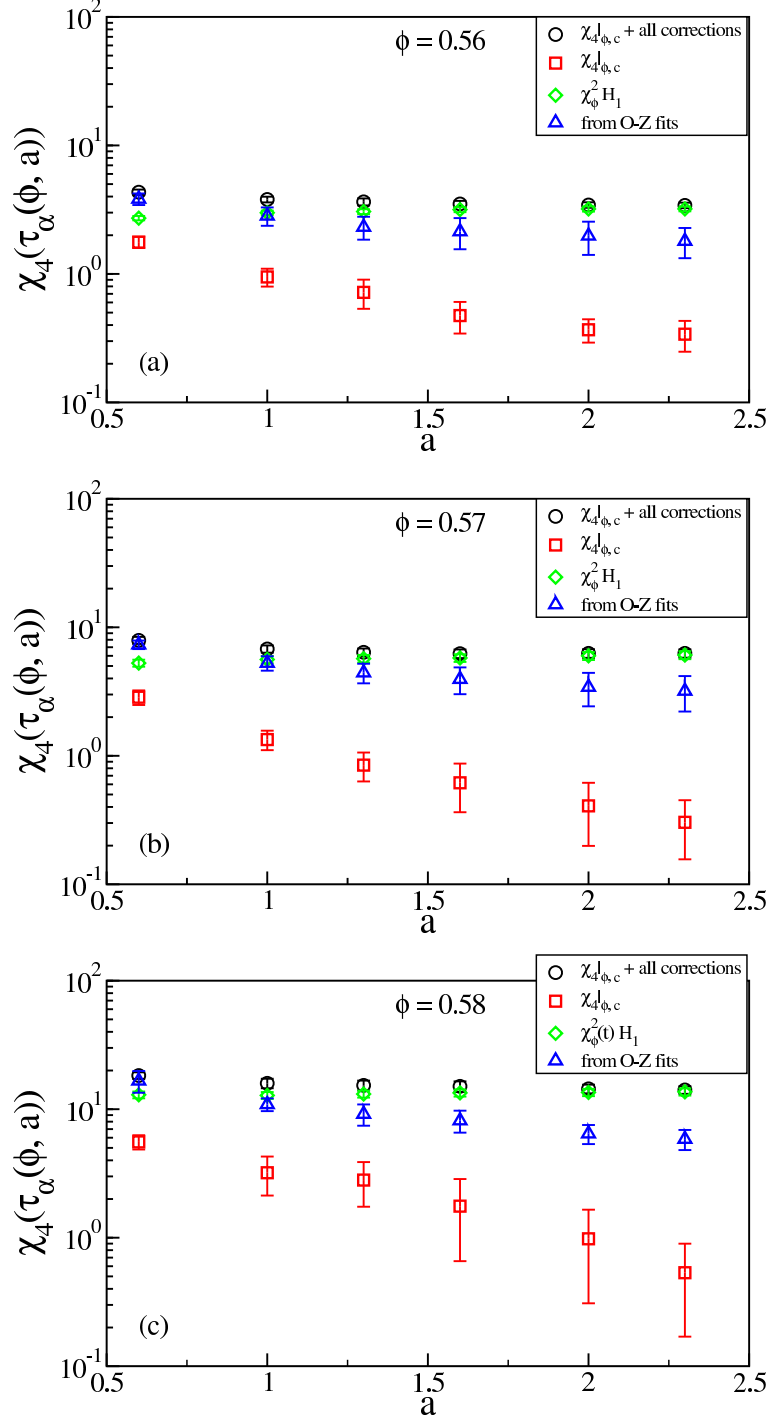


Figure 4.6: The dynamic susceptibility calculated via equation 4.14 at the time $\tau_\alpha(\phi, a)$ versus the parameters a . The first term $\phi_{4\phi,c}^1(\tau_\alpha(\phi, a))|_{\phi,c}$ and second term $\chi_\phi^2(\tau_\alpha(\phi, a))H_1$ in equation 4.14 are also plotted. The χ_4 evaluated from equation 4.14 are compared with those extracted from the Ornstein-Zernicke fits.

$\chi_\phi(a, t)$ reaches its peak at the time other than the α -relaxation time. However, with $a = 0.3$, it has been found that $\chi_\phi(t)$ had the peak at $\tau_\alpha(\phi, a)$ for our system. For a different system Chandler et al. [21] showed

that the peaks of $\chi_M(t)$ merge at $\tau_\alpha(\phi, a)$ with a between 0.2 and 0.5. Although their results cannot be compared with ours directly due to different definition of the four-point susceptibility, they still imply the high possibility that the peak of $\chi_4(a, t)$ happens at the α -relaxation time regardless of a . Beside, within the MCT scheme, Berthier et al. found that $\chi_\phi(k, t)$ become maximum at $\tau_\alpha(\phi, k)$ [16]. This inference can be very possibly extended to our system, since both k^{-1} and a play roles as the probed length scale. Based on the discussion made above, we believe that our observations about the a -dependence of the four-point susceptibility is reliable. However, to achieve a more convincing conclusion, the time evolution of the $\chi_4(\phi, a, t)$ definitely needs to be explored in the future.

We want to point out that the discrepancy appears only for larger a (> 1.0), while for smaller a (≤ 1.0) the trends of $\chi_\phi(\tau_\alpha(\phi, a))$ follows the prediction made in [16]. Thus we argue that within the small and moderate probe length scale, $\chi_\phi(\tau_\alpha(\phi, a))$ grows with increasing of a (or k^{-1}), and beyond this range $\chi_\phi(\tau_\alpha(\phi, a))$ will stay constant. With careful inspection of Figure 6 in [16], we found that the growth of peak in $\chi_\phi(k, t)$ seems to become slow when k is small. However, this assumption is quite naive. First we do not know the exact values of k they used. Second, the wave vector in their case cannot be related to a in our work directly. The conversion between k and a is complex. To relate them, one can calculate the self-intermediate scattering function $F_s(k, t)$ with various wavevectors k , and the average overlap function $F_o(a, t)$ with different parameters a . If with some k and a , $F_s(k, t)$ and $F_o(a, t)$ have the same α -relaxation, then one can say that k and a correspond with each other.

Finally, there are two points that need to be emphasized here. First of all, our results again support the idea proposed by Berthier et al. [3] that the experimentally accessible dynamic susceptibility χ_x (in our case, it is χ_ϕ) can give a rigorous lower bound for χ_4 . The fact that $\chi_4(\tau_\alpha(\phi, a))$ is determined primarily by $\chi_\phi^2(\tau_\alpha(\phi, a))H_1$ at larger a shows that a more precise estimation of $\chi_4(\tau_\alpha(\phi, a))$ can be achieved. Secondly, from the plateau in the four-point susceptibility, it is reasonable to believe that the strength of dynamic heterogeneity at the relaxation time $\tau_{\phi, a}$ is unique, independent of the choice of a . Correspondingly, we expect that for large a , the dynamic correlation length is not dependent on a either.

4.3.4 Four-point structure factor

Analogous to the work done by Lačević et al. [17] we define a radial-averaged four-point correlation function $g_4(r)$ which is related to $\chi_4(t)$ by,

$$\chi_4(t) = \int g_4(\mathbf{r}, t) d\mathbf{r} . \quad (4.23)$$

Following the same procedure as in [17], $g_4(\mathbf{r}, t)$ can be written as,

$$g_4(\mathbf{r}, t) = \frac{1}{N} \left\langle \sum_{i=1}^N \sum_{j=1}^N \delta(\mathbf{r} - \mathbf{r}_{ij}(0)) w_i(t) w_j(t) \right\rangle - \frac{\langle N_s(t) \rangle^2}{NV} \quad (4.24)$$

The four-point structure factor $S_4(\mathbf{q}, t)$ is defined as the Fourier transform of $g_4(\mathbf{r}, t)$,

$$S_4(\mathbf{q}, t) = \int g_4(\mathbf{r}, t) \exp[-i\mathbf{q} \cdot \mathbf{r}] d\mathbf{r} \quad (4.25)$$

$$= N^{-1} \left(\langle W(\mathbf{q}, t) W(-\mathbf{q}, t) \rangle - |\langle W(\mathbf{q}, t) \rangle|^2 \right), \quad (4.26)$$

where $W(\mathbf{q}, t)$ is the Fourier transform of microscopic overlap function [1],

$$W(\mathbf{q}, t) = \sum_i^N w_i(t) \exp[-i\mathbf{q} \cdot \mathbf{r}_i(0)]. \quad (4.27)$$

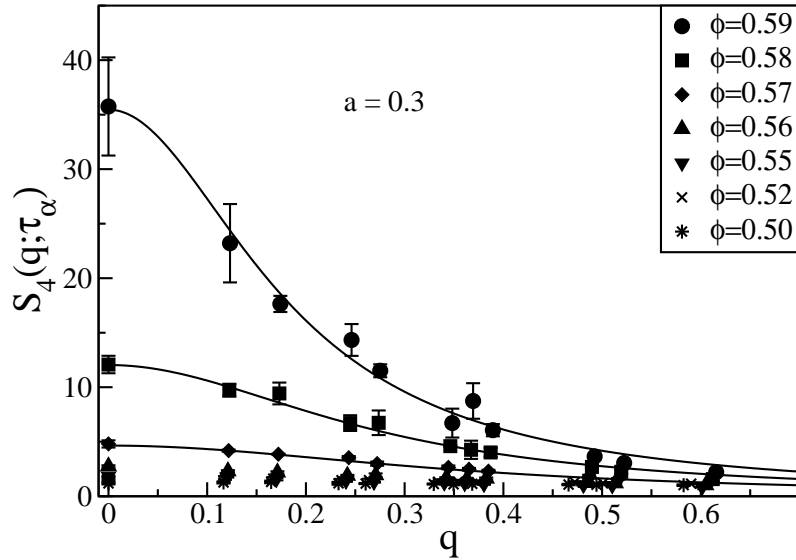


Figure 4.7: The four-point structure factors are evaluated at the α relaxation time. The dynamic susceptibilities $\chi_4(\tau_\alpha)$ calculated via equation 4.14 are used as the values of $S(q = 0, t)$. The volume fractions from top to bottom are $\phi = 0.59, 0.58, 0.57, 0.56, 0.55, 0.52, 0.50$. The solid lines are the Ornstein-Zernicke fits (see equation 4.29). The figure is adopted from reference [1].

The four-point structure factors for $a = 0.3$ with various volume fractions have been calculated at the α -relaxation time by Flenner et al. [1]. The figure of $S_4(q, \tau_\alpha(\phi, a = 0.3))$ is adopted as figure 4.7 to show the volume fraction dependence of $S_4(q, \tau_\alpha(\phi, a = 0.3))$ and to make a clear comparison with figure 4.8.

In figure 4.7 $\chi_4(a, t)$ calculated via equation 4.14 at the τ_α are included as $S_4(q = 0, \tau_\alpha)$, because with connecting equation 4.26 to equation 4.23, the relation between $\chi_4(t)$ and $S_4(q, t)$ can be obtained immediately,

$$\lim_{q \rightarrow 0} S_4(q, t) = \chi_4(t). \quad (4.28)$$

It has to be emphasized that equation 4.28 is valid only when the fluctuations of all conserved variables are included in $\chi_4(t)$ [5]. In our case $\chi_4(t)$ needs to be calculated by equation 4.14, because $\chi_4(t)$ depends on the statistical ensembles chosen to do the calculation. On the other hand, $S_4(q \neq 0)$ is not changeable with different ensembles, since it measures the local spatial correlations [1, 5].

It is shown in figure 4.7 that $S_4(q, \tau_\alpha)$ with small wave vectors increases quickly as the volume fractions goes larger, especially for $q \rightarrow 0$. Within the small wave vectors the dynamic correlation length $\xi(t)$ can be obtain by fitting the four-point structure factor with the Ornstein-Zernike form (i.e. equation 4.29) [1, 5, 17],

$$S_4(q, t) = \frac{A}{1 + (\xi(t)q)^2}. \quad (4.29)$$

It was previous established that to get reliable results, one should use the wavevector in the range to $q \leq 1.5/\xi$. There are usually two ways to use equation 4.29. First the parameter A in the equation can be substituted by $\chi_4(t)$, then $\xi(t)$ is the only fitting parameter. Second without the point at $q = 0$, both A and $\xi(t)$ can be regarded as parameters, and be fitted at the same time. For $a = 0.3$, the results from these two ways agree with each other very well [1]. Thus the four-point susceptibility can either be calculated directly via equation 4.14, or evaluated from the fitting of the four-point structure factor. Both methods give consistent measurements at $a = 0.3$.

The four-point structure factor at α -relaxation time for various volume fractions have been analyzed with $a = 0.3$. Next we will focus on the effects of the parameter a on $S_4(q, \tau_\alpha(\phi, a))$. With different a values, $S_4(q, \tau_\alpha(\phi, a))$ are calculated for the volume fraction 0.56, 0.57, 0.58 and plotted in figure 4.8. For each volume fraction, $S_4(q\tau_\alpha(\phi, a))$ decreases with increasing a . With the same parameter a , $S_4(q\tau_\alpha(\phi, a))$ goes up with larger volume fraction, the same as that shown in the previous figure. For every $S_4(q\tau_\alpha(\phi, a))$ in figure 4.8, the O-Z fit is performed. Different from the situation at $a = 0.3$, $\chi_4(\tau_\alpha(\phi, a))$ are not used as the values of the four-point structure facton at $q = 0$. The reason is that one cannot get reasonable dynamic correlation length via fitting in this way. Thus we choose the second fitting procedure, both A and ξ are treated as parameters. The dynamic correlation obtained in this way lengths are listed in figure 4.9, and will be discussed in the following section. The four-point susceptibilities are plotted in figure 4.6. When the parameter a is small (i.e. $a = 0.3$ and 0.6), $\chi_4(\tau_\alpha(\phi, a))$ obtained from the extrapolation of $S_4(q\tau_\alpha(\phi, a))$

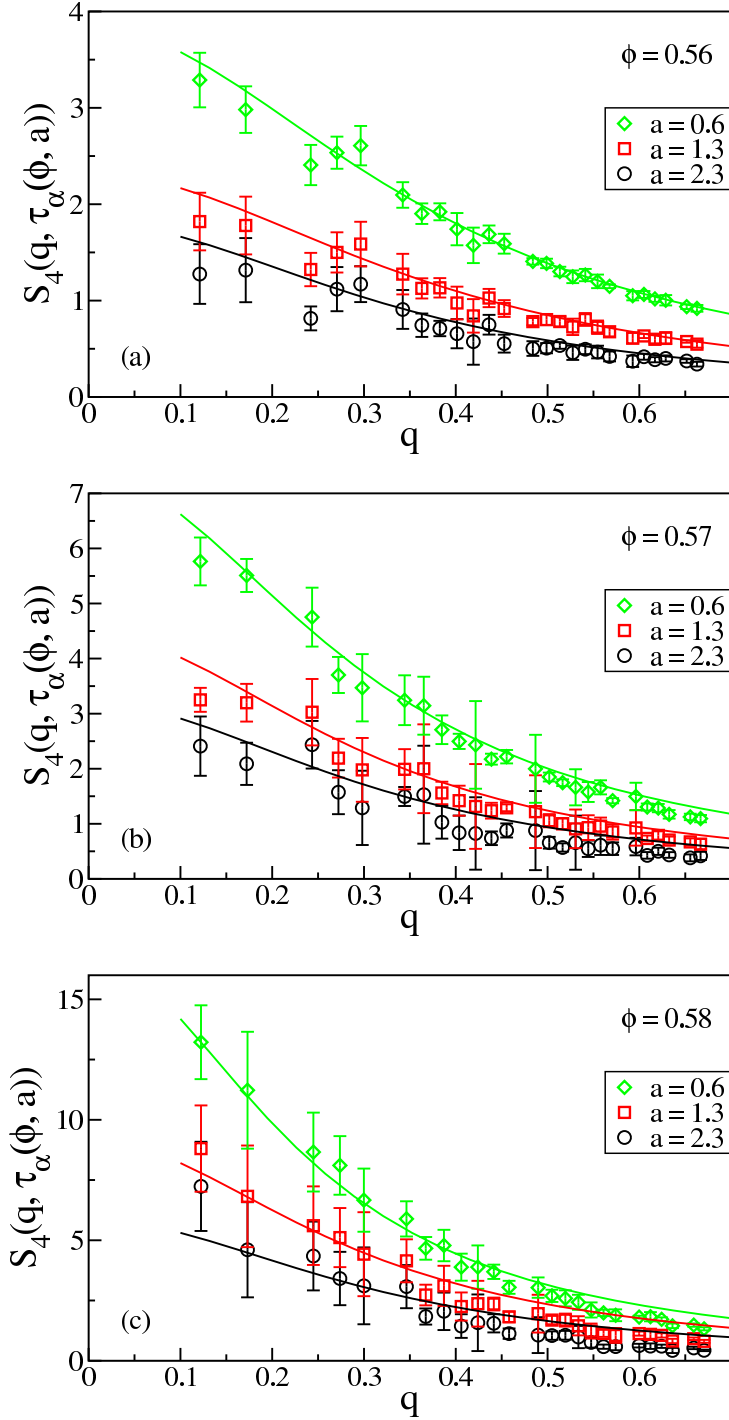


Figure 4.8: The four-point structure factors are evaluated at the α relaxation time $\tau_\alpha(\phi, a)$. To illustrate the a dependence, three a values are picked for each volume fraction. The solid lines are the Ornstein-Zernicke fits (see equation 4.29).

agree with those calculated by equation 4.14. Around $a = 1.0$ the discrepancies between the results from the two methods merger for all three volume fractions we considered here. This deviation increases as a become

even larger. Equation 4.14 predicts that $\chi_4(\tau_\alpha(\phi, a))$ tends to be independent of the choice of the parameter a when it is large enough. In contrast, $\chi_4(\tau_\alpha(\phi, a))$ evaluated from the four-point structure factor tends to decrease when the bigger parameter a is chosen.

To figure out the reasons for the discrepancy, the first one needs to be examined is the size effect because it relates with the smallest q value that we can probe. For a three dimensional system, q can have the values calculated below,

$$q = \frac{2\pi}{L}(n_x^2 + n_y^2 + n_z^2), \quad (4.30)$$

where n_x , n_y and n_z are non-negative integers, but cannot be zero at the same time. L is the length of the simulating box. Thus the smallest wave vector $q_{min} = 2\pi/L$. With fixed volume fraction, to increase the size of the box, larger system with more particles needs to be explored. However it is very expensive for computer simulations. If q is reduced to be 10% of the its old value, one has to use a system which contains 1000 times of particles as before. The simulation will be extremely time-consuming. For the liquid we investigate here, bigger systems have been explored by Szamel et al. and no evidence has been observed so far to show the deviation between the two χ_4 mentioned above is due to the size effect [39].

To find other possible reasons, let us analyze the effect of a on the calculation of the four-point structure factor. When a is small, close to the cage size, at the α -relaxation time, the displacements of the slow particles are very small (< 0.3), these particles can be regarded moving slowly during all the time $\tau_\alpha(\phi, a)$. The position of the slow particles at $\tau_\alpha(\phi, a)$ are highly correlated with their original positions. On the other hand, when a is really larger, the α relaxation time grows very quickly. Around $\tau_\alpha(\phi, a)$ the diffusive motion and ergodicity have been restored. The so-called ‘slow’ particle defined by equation 4.4 may have gone through several ‘slow motion’ and ‘quick motion’ periods and lost the memories about their original positions. In this case, $W(q, \tau_\alpha(\phi, a))$ calculated by equation 4.27 is actually reduced to $e^{-1}\rho(q)$ (since $F_o(\tau_\alpha(\phi, a)) = e^{-1}$), where $\rho(q) = \sum_1^N \exp(-i\mathbf{q} \cdot \mathbf{r})$ is the Fourier transform of the density. Thus $S_4(\mathbf{q}, \tau_\alpha(\phi, a))$ measured via equation 4.26 becomes proportional to the static structure factor $S(q) = \frac{1}{N} \langle \rho(q)\rho(-q) \rangle$ for the homogeneous system. Remember that for very small q values, $S(q)$ reduces to a small value close to zero [17]. As the parameter a grows, at $\tau_\alpha(\phi, a)$, the crossover from dynamic heterogeneity to homogeneity mergers, the four-point structure factor gradually lost information about the heterogeneous dynamics and falls into the static structure factor finally. As a consequence, $\chi_4(\tau_\alpha(\phi, a))$ is underestimated in this way.

In this subsection, the four-point structure factor is explored. We show that the four-point susceptibility can be gotten by the extrapolation of $S_4(q, t)$ to $q = 0$ via the Ornstein-Zernicke fit. At $a = 0.3$ values generated by this method agree with those calculated by equation 4.14. However, as the parameter a is larger than 1.0, $\chi_4(\tau_\alpha(\phi, a))$ evaluated from $S(q, \tau_\alpha(\phi, a))$ tends to decrease with increasing a . In contrast,

the four-point susceptibility measured via equation 4.14 tends to be independent of a . We tried to find the reason that causes this discrepancy and propose a possible explanation. When a becomes larger, the α -relaxation time increases very quickly. At $\tau_\alpha(\phi, a)$ the homogeneity of the system grows. Most particles will experience many ‘slow motion’ and ‘quick motion’ periods and forget their histories. The procedure for selecting the ‘slow’ particles becomes actually picking the particles randomly. Thus $W(q, \tau_\alpha(\phi, a))$ is reduced to $e^{-1}\rho(q)$. As a consequence, $S_4(\mathbf{q}, \tau_\alpha(\phi, a))$ becomes proportional to the static structure factor and lost the dynamic informations, so $\chi_4(\tau_\alpha(\phi, a))$ is underestimated.

4.3.5 Dynamical correlation length

The four-point structure factors at the α -relaxation time were studied in the last section, where the dynamic correlation length has been extracted via the Ornstein-Zernicke fit and plotted in figure 4.9 versus the parameter a at the volume fraction $\phi = 0.56, 0.57, 0.58$, respectively.

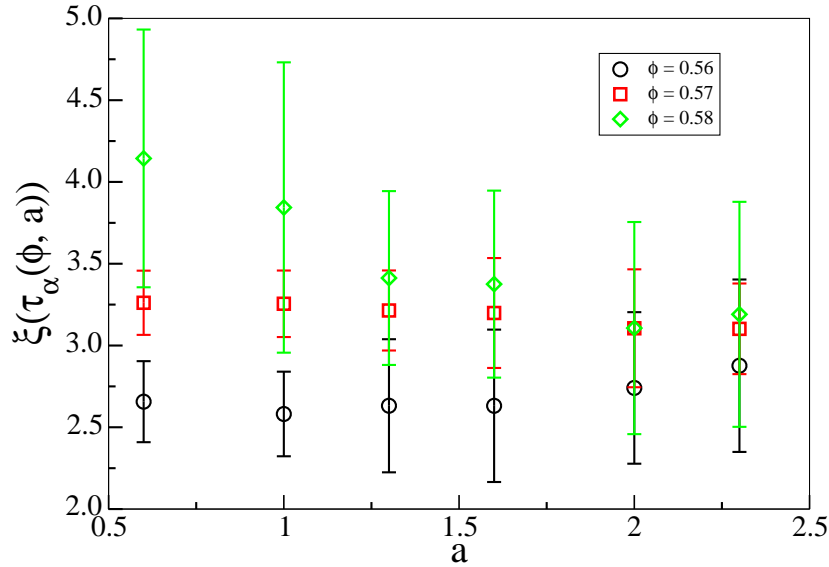


Figure 4.9: The correlation length $\xi(\tau)$ are fitted via Ornstein-Zernicke function, refer to the text for details, and plotted versus the parameter a .

From the figure, one can see that the statistics are poor. The reason is twofold. When the volume fraction grows or the large parameter a is picked, $\tau_\alpha(\phi, a)$ becomes very large. The four-point structure factors calculated at this time do not have very good statistics themselves (see figure 4.8), since with longer time intervals, the averages are calculated over less numbers of intervals. The second reason may be more

critical, namely, the influence of the finite size. As we have discussed before, the smallest q value is inversely proportional to the box length, and q is not continuous, only those satisfied with equation 4.30 can be used. The third reason is that to get the correlation length, the fit can only be performed with small q (long wave length), specifically, we restrict $q \leq 1.5/\xi(\tau_\alpha)$ during the fitting procedure [1]. When the volume fraction is large, $\xi(\tau_\alpha)$ is quite large, for instance $\xi(\tau_\alpha)$ is around 4.5 for $\phi = 0.58$, resulting that q must be smaller than 0.33. With these three reasons, only several q values can be used and the statistics is of course not good. Based on the analysis we make here, to improve the statistics of the correlation length, the simulations need to be run with longer time and bigger systems. However it is not easy to do because of extremely long computational time.

Although the statistics is not so good, with the inspection of figure 4.9, we still can see that the correlation lengths at the α relaxation times are roughly independent of the parameter a . To confirm this speculation, we comparing $\xi(\tau_\alpha(\phi, a))$ with the former study at $a = 0.3$ [1]. We found that the correlation lengths at $\tau_\alpha(\phi, a)$ with $a \geq 0.6$ are larger than the one calculated with $a = 0.3$. This phenomenon is observed for all the volume fractions. However, it does not mean that the dynamic correlation length increases with a . It is because with $a = 0.3$, $\xi(t)$ does not reach its maximum at $\tau_\alpha(\phi, a)$, but continues growing beyond the relaxation time. Finally $\xi(t)$ saturates at $\tau_{\max} (> \tau_\alpha(\phi, a))$ and keeps constant in the rest of the time window for observation [1]. For each fixed volume fraction, $\xi(\tau_\alpha(\phi, a \geq 0.6))$ is approximately equal to the plateau value ξ_{\max} evaluated at $a = 0.3$. This result implies that the dynamic correlation length ξ_{\max} is unique, unaffected by the choice of a . We also suspect that $\tau_{\max}(\phi, a)$ grows slowly than $> \tau_\alpha(\phi, a)$ does when the parameter a increases. In this case, at $a = 0.3$, $\tau_{\max}(\phi, a) > \tau_\alpha(\phi, a)$, while at larger a , $\xi(t)$ reaches the plateau before the α -relaxation time. As a consequence $\xi(\tau_\alpha(\phi, a))$ remains constant with increasing a . To examine this speculation the time dependence of $\xi(t)$ at various a will be investigated in the future. If our speculation is true, then the certain parameter a at which $\tau_{\max}(\phi, a) = \tau_\alpha(\phi, a)$ may be a proper probed length scale to measure dynamic heterogeneity of this system.

In [1], Flenner et al. found that at $a = 0.3$, ξ_{\max} is proportional to $\xi(\tau_\alpha(\phi, a))$, and τ_α has the relationship with $\xi(\tau_\alpha)$ expressed as,

$$\tau_\alpha = A \exp(k_\tau \xi) . \quad (4.31)$$

A and k_τ in this equation are parameters. Combining with the fact that ξ_{\max} is independent of the parameter a , while $\tau_\alpha(\phi, a)$ is related to a via equation 4.11, we expect that for larger a , the α -relaxation time has a relationship with the dynamic correlation length via the following form,

$$\tau_\alpha = B \xi(\tau_\alpha) a^b \exp(k \xi_{\max}) , \quad (4.32)$$

where B and k are fitting parameters, and where b is the exponent in equation 4.11

We have to emphasize that all the analysis made above base on a foundation that $\xi(t)$ will stay unchanged after it arrives at the plateau. Although it has been demonstrated for our system with $a = 0.3$ [1], and for some other systems [22]. The other types of the time dependency for $\xi(t)$ have also been reported. For instance some research showed that the correlation lengths decrease after the arrive at its maximum, which have the similar shapes as the four-point susceptibility [17, 40]. On the other hand, Toninelli [41] et al. argued that $\xi(t)$ would grows with time forever. So far the unambiguous conclusion about the time dependence of the correlation length remains elusive. Continuing the research on the time dependency of ξ with various volume fraction and parameter a may help to untangle the mystery.

4.3.6 Four-point pair correlation function

The static pair correlation function is usually used to define the spatial structure of the system at the initial time [1]. For a two-component system it can be written as,

$$g_{\alpha\beta}(r) = \frac{V}{N_\alpha(N_\beta - \delta_{\alpha\beta})} \left\langle \sum_i^{N_\alpha} \sum_{j \neq i}^{N_\beta} \delta(\mathbf{r} - \mathbf{r}_{ij}) \right\rangle. \quad (4.33)$$

In the equation V is the volume of the system, α and β can be either larger particles A or small particles B . N_α and N_β are the numbers of particles for the particle species α and β , respectively. Similarly, the so called four-point pair correlation function $G_4(r, t)$ has been defined by Flenner etc [1] in the form,

$$G_4(r, t) = \frac{V}{\langle N_s(t) \rangle (\langle N_s(t) \rangle - 1)} \times \left\langle \sum_{i=1}^N \sum_{j \neq i}^N \delta(\mathbf{r} - \mathbf{r}_{ij}(0)) w_i(t) w_j(t) \right\rangle, \quad (4.34)$$

which is a generalized form of the pair correlation function with considering only the ‘slow’ particles (including both large and small species). $G_4(r, t)$ can be related to $g_4(\mathbf{r}, t)$ that is used to give the expression of $S_4(q, t)$,

$$g_4(\mathbf{r}, t) = \frac{\langle N_s(t) \rangle (\langle N_s(t) \rangle - 1)}{NV} [G_4(r, t) - 1] + \frac{\langle N_s(t) \rangle}{N} \delta(\mathbf{r}) - \frac{\langle N_s(t) \rangle}{NV}. \quad (4.35)$$

Performing the Fourier transform of $g_4(\mathbf{r}, t)$ the four-point structure factor can also be written as [1],

$$S_4(\mathbf{q}, t) = \frac{\langle N_s(t) \rangle (\langle N_s(t) \rangle - 1)}{NV} \tilde{G}_4(q, t) + \frac{\langle N_s(t) \rangle}{N} - \frac{\langle N_s(t) \rangle}{NV} \delta(q), \quad (4.36)$$

where $\tilde{G}_4(q, t)$ is the Fourier transform of $G_4(r, t) - 1$.

Lačević et al. [42] suggested that the correlation length can also be obtained by fitting the four-point pair correlation function via the exponential envelope function,

$$f(r) = c \exp[-r/\xi(t)] , \quad (4.37)$$

where c is a fitting parameter. There are some issues with this method. First it is hard to fit $G_4(r, t)$ precisely, because it oscillates all the time. Second $\xi(t)$ evaluated in this way is underestimated [17]. However, the ‘envelope fit’ of $G_4(r, t)$ can still be explore to make a qualitative examination for $\xi(t)$ obtained from $S_4(q, t)$. Flenner et al. proposed a similar function,

$$f(r) = c \exp[-r/\xi(t)]/r . \quad (4.38)$$

They found that with using the correlation length evaluated from $S_4(q, t)$, this function can fit $G_4(r, t) - 1$ quite well [1]

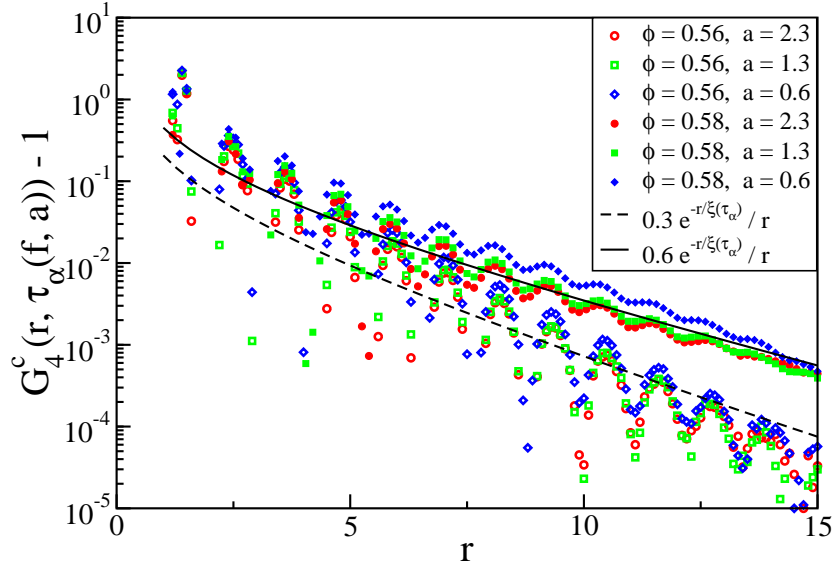


Figure 4.10: The corrected four-point pair correlation functions for the volume fractions $\phi = 0.56$ and 0.58 with various parameters a are plotted. The solid line and the dashed line are the fits with equation 4.38 for $\phi = 0.56$ and 0.58 respectively. The correlation lengths are $\xi(\tau_\alpha) = 2.69$ for $\phi = 0.56$ and $\xi(\tau_\alpha) = 3.51$ for $\phi = 0.58$, which are fitted via Ornstein-Zernicke function.

The four-point pair correlation functions for $\phi = 0.56, 0.58$ and $a = 0.6, 1.3, 2.3$ at the α -relaxation time are plotted in figure 4.10. Notice here, we use the notion $G_4^c(r, \tau_\alpha(\phi, a)) - 1$ for the y -axis. The reason

is that due to the finite size $G_4(r, \tau_\alpha(\phi, a)) - 1$ actually does not decay to 0, but to a small value which is inversely proportional to the volume [1]. This is related to the ensemble dependence of χ_4 , and this small value is another manifestation of the correction terms in equation 4.14. To exclude the effect of the finite size, the average value for $G_4^c(r, \tau_\alpha(\phi, a))$ is calculated at $r = L/2$ (L is the length of the simulation box) and subtracted from $G_4(r, \tau_\alpha(\phi, a))$. This corrected quantity is denoted as $G_4^c(r, \tau_\alpha(\phi, a))$ [1].

Figure 4.10 shows that with each parameter a the four-point pair correlation function decays slower with larger volume fraction which indicates bigger dynamic correlation length. This trend agrees with the results for $a = 0.3$ reported by Flenner et al. [1]. When larger parameter a is used, $G_4^c(r, \tau_\alpha(\phi, a))$ is found slightly moving downwards. This is more evident for $\phi = 0.58$. It is not clear why this happens. It might be recognized as one of the reasons that cause the decreases in $S_4(q, \tau_\alpha(\phi, a))$ with increasing a . Since according to equation 4.36, $\langle N_s(\tau_\alpha(\phi, a)) \rangle = e^{-1}$ is a constant at the α -relaxation time, $S_4(q, \tau_\alpha(\phi, a))$ is determined only by the Fourier transform of $G_4(r, \tau_\alpha(\phi, a)) - 1$. The decrease of $G_4(r, \tau_\alpha(\phi, a))$ will directly result in the smaller value of $S_4(q, \tau_\alpha(\phi, a))$, especially for longer wave length.

Regardless of the small change in $G_4^c(r, \tau_\alpha(\phi, a)) - 1$ with different a , equation 4.38 generates qualitatively good fits for $G_4^c(r, \tau_\alpha(\phi, a)) - 1$. The correlation lengths in this equation are obtained by fitting the four-point structure factor as we discussed previously. These fits again show that the dynamic correlation length is weakly dependent on the choice of the parameter a .

4.4 Discussion

In this chapter, we used some alternative values for the parameter a in equation 4.4. The effect of the choice of a on the dynamic heterogeneous behavior of supercooled liquid, such as the four-point dynamic correlators and the related length scales, time scales, is examined.

As a substitution of the self-intermediate scattering function, the average overlap function $F_o(a, t)$ was calculated and studied at different volume fraction and various parameters a . When the probed length scale ($\sim a$) becomes larger, a crossover from heterogeneous dynamic to homogeneous behavior is observed in $F_o(a, t)$ due to the hydrodynamic effect. This crossover will cause the decrease of the fluctuation in $F_o(a, t)$.

The structural relaxation times extracted from the average overlap function are found following a simple equation of the parameter a (equation 4.11). Assume that the exponent b is a constant (or very weakly dependent on ϕ) and equation 4.11 is valid for all the volume fractions close to the glass transition. In that case, for each a the relation between τ_α and ϕ can be expressed by equation 4.9 or 4.10. Although τ_α varies with different a , most of these relaxation time are not so meaningful. I suspect that only one τ_α obtained at

some ‘proper’ a can be regarded as the time scale of dynamic heterogeneity and gives universal properties. To search this time, the system needs to be studied with other values of a at various volume fractions.

For every combination of a and ϕ , the four-point susceptibility, four-point pair correlation function and the four-point structure factor were calculated at the structural relaxation time $\tau_\alpha(\phi, a)$. It is found that with increasing a , the first term $(\chi_4(\tau_\alpha(\phi, a))|_{\phi, c})$ in equation 4.14 decays, while the second term $(\chi_\phi^2(\tau_\alpha(\phi, a))H_1)$ grows when a increases from 0.3 to 1.0 and saturates after that. Overall, the four-point susceptibility expressed in equation 4.14 remains constant at least for larger parameter a , which implies that the strength of dynamic heterogeneity is almost independent of the ‘measuring stick’. This result also suggest that the correction term $\mathcal{X}(t)$ can give an even better estimation for χ_4 if larger probed length scale is used.

On the other hand, we observed that the four-point susceptibility obtained by the extrapolation of $S_4(q, \tau_\alpha(\phi, a))$ to $q = 0$ via the Ornstein-Zernicke fit inclines to decrease with increasing a , when the parameter a is larger than 1.0. We showed that this discrepancy is presumably caused by the fact that with large α -relaxation time, the system is more homogeneous. It is less meaningful to choose the ‘slow’ particles, due to the ergodicity most particles can go through the ‘slow motion’ and ‘quick motion’ repeatedly and forget their histories. As a consequence $S_4(\mathbf{q}, \tau_\alpha(\phi, a))$ calculated via equation 4.26 becomes proportional to the static structure factor and lost the dynamic informations, thus underestimate $\chi_4(\tau_\alpha(\phi, a))$.

From the Ornstein-Zernicke fit for $S_4(q, \tau_\alpha(\phi, a))$, the dynamic correlation lengths $(\xi(\tau_\alpha(\phi, a)))$ are also estimated for various ϕ and a . With the poor statistics, the $\xi(\tau_\alpha(\phi, a))$ are found roughly independent of the parameter $a \geq 0.6$, and also consistent with ξ_{\max} obtained at $a = 0.3$ [1]. We suspect that ξ_{\max} is the universal dynamic correlation length and unaffected by the choice of a . We also speculate that for each a (not only $a = 0.3$ [1]), the $\xi(a, t)$ grows with t to the maximum at the time τ_{\max} , and remains constant after that. For smaller a , τ_{\max} is larger than $\tau_\alpha(\phi, a)$, while the α -relaxation time increases faster than τ_{\max} does. Eventually, $\tau_\alpha(\phi, a)$ becomes larger, and $\xi(a, t)$ arrives the plateau before the α -relaxation time. Thus $\xi(\tau_\alpha(\phi, a))$ measured for large a is constant and is equal to ξ_{\max} . The parameter a independence for the dynamic correlation length is also supported by the fits of the four-point pair correlation functions.

Before closing this chapter, we want to stress that the discussion made above entails the continuous work on the time dependence of the four-point susceptibility and dynamic correlation length of the system with various volume fractions and parameter a . The future work will help to examine these important speculations. 1. Does the four-point susceptibility reach its peak value at the α -relaxation time for all parameters a ? 2. Is the maximum of the dynamic correlation length independent of a ? 3. Does the time τ_{\max} at which ξ grows to maximum increase faster than the α -relaxation time?

Bibliography

- [1] E. Flenner, M. Zhang, and G. Szamel, *Phys. Rev. E* **83**, 051501 (2011).
- [2] H. C. Andersen, *PNAS* **102**, 6686 (2005).
- [3] L. Berthier, G. Biroli, J. -P. Bouchaud, L. Cipelletti, D. El Masri, D. L'Hôte, F. Ladieu, and M. Pierno, *Science* **310**, 1797 (2005).
- [4] J. P. Garrahan and D. Chandler, *Phys. Rev. Lett.* **89**, 035704 (2002).
- [5] L. Berthier, G. Biroli, J. -P. Bouchaud, W. Kob, K. Miyazaki, and D. R. Reichman, *J. Chem. Phys.* **126**, 184503 (2007).
- [6] Y. Gao and M. L. Kilfoil, *Phys. Rev. Lett.* **99**, 078301 (2007).
- [7] , B. Wang, S. M. Anthony, S. C. Bae, and S. Granick, *PNAS*, **106**, 15160 (2009).
- [8] C. Eisenmann, C. Kim, J. Mattsson, and D. A. Weitz, *Phys. Rev. Lett.* **104**, 035502 (2010).
- [9] K. N. Nordstorm, J. P. Gollub, and D. J. Durian, *Phys. Rev. E* **84**, 021403 (2011).
- [10] E. Flenner and G. Szamel, *Phys. Rev. E* **72**, 011205 (2005).
- [11] P. I Hurtado, L. Berthier, and W. Kob, *Phys. Rev. Lett.* **98**, 135503 (2007).
- [12] P. Chaudhuri, S. Sastry, and W. Kob, *Phys. Rev. Lett.* **101**, 190601 (2008).
- [13] S. Whitelam, L. Berthier, J. P. Garrahan, *Phys. Rev. Lett.* **92**, 185705 (2004).
- [14] A. Furukawa and H. Tanaka, *Phys. Rev. E* **84**, 061503 (2011).
- [15] P. Chaudhuri, L. Berthier, and W. Kob, *Phys. Rev. Lett.* **99**, 060604 (2007).
- [16] L. Berthier, G. Biroli, J. -P. Bouchaud, W. Kob, K. Miyazaki, and D. R. Reichman, *J. Chem. Phys.* **126**, 184504 (2007).
- [17] N. Lačević, F. W. Starr, T. B. Schröder, and S. C. Glotzer, *J. Chem. Phys.* **119**, 7372 (2003).
- [18] E. Flenner and G. Szamel, *Phys. Rev. Lett.* **105**, 217801 (2010).
- [19] G. Adam and J. H. Gibbs, *J. Chem. Phys.* **43**, 139 (1965).
- [20] G. Brambilla, D. El Masri, M. Pierno, L. Berthier, L. Gipelletti, G. Petekidis, and A. B. Schofield, *Phys. Rev. Lett.* **102**, 085703 (2009).

- [21] D. Chandler, J. P. Garrahan, R. L. Jack, L. Maibaum, and A. C. Pan, *Phys. Rev. E* **74**, 051501 (2006).
- [22] Z Rotman and E. Eisenberg, *Phys. Rev. Lett.* **105**, 225503 (2010).
- [23] Z Rotman and E. Eisenberg, *Phys. Rev. E* **80**, 060104(R) (2009).
- [24] L. Berthier and W. Kob, *J. Phys.: Condens. Matter* **19**, 205130 (2007).
- [25] W. Kob and H. C. Andersen, *Phys. Rev. E* **52**, 4134 (1995).
- [26] P. Gallo, A. Attili, and M. Rovere, *Phys. Rev. E* **80**, 061502 (2009).
- [27] A. de Candia, A. Fierro, A Coniglio, *J. Stat. Phys.* **145**, 652 (2011).
- [28] M. D. Ediger, *Annu. Rev. Phys. Chem.* **51**, 99 (2000).
- [29] L. Berthier and G. Biroli, *Rev. Mod. Phys.* **83**, 587 (2011).
- [30] S. Léonard and L. Berthier, *J. Phys.: Condens. Matter* **17**, 3571 (2005).
- [31] E. Flenner and G. Szamel, *Phys. Rev. E* **70**, 052501 (2004).
- [32] C-Y Wang and M. D. Ediger, *J. Phys. Chem. B* **103**, 4177 (1999).
- [33] S. Léonard and L Berthier, *J. Phys.: Condens. Matter* **17**, S3517 (2005).
- [34] L. Berthier and T. A. Witten, *Phys. Rev. E* **80**, 021502 (2009).
- [35] W. Kob and H. C. Andersen, *Phys. Rev. E* **51**, 4626 (1995).
- [36] E. Flenner and G. Szamel, *Phys. Rev. E* **72**, 031508 (2005).
- [37] L. Berthier, *Phys. Rev. E* **69**, 020201(R) (2004).
- [38] K. Kim and S. Saito, *J. Chem. Phys.* **133**, 044511 (2010).
- [39] G. Szamel (*private communication*).
- [40] R. Pastore, M. P. Ciamarra, A. de Candia, and A. Coniglio, *Phys. Rev. Lett.* **107**, 065703 (2011).
- [41] C. Toninelli, M. Wyart, L. Berthier, G. Biroli, and J-P. Bouchaud, *Phys. Rev. E* **71**, 041505 (2005).
- [42] N. Lačević, F. W. Starr, T. B. Schröder, V. N. Novikov and S. C. Glotzer, *Phys. Rev. E* **66**, 030101 (R) (2002).

Chapter 5

Summary

There are two main goals of the investigations described in this dissertation. One of the objective is to find a proper method to define and to calculate the so-called ‘effective temperature’ of nonequilibrium systems. The second one is to investigate the dynamic properties of glass-forming liquids.

5.1 Effective temperatures of nonequilibrium systems

In chapter 2, we have studied a simple colloidal suspension under shear, four definitions of the effective temperature was investigated. Two of them are based on the extended fluctuation-dissipation theorem, and they generate the same results. The other two were calculated from the static quantities. The one evaluated by fitting the density distribution profiles agrees very well with those calculated from FDT, while the one based on the linear response relation involving the static structure factor deviates from the other three. With high shear rate, the system is strongly anisotropic. In this case, all the effective temperatures were calculated along two different directions, namely, the velocity gradient direction and the vorticity direction. The one in the velocity gradient direction is somewhat higher than that along the vorticity direction. All the effective temperatures are higher than the bath temperature due to the imposed shear. Moreover, they grow as the shear rate increases.

In chapter 3, a binary Lennard-Jones system was investigated. Due to a very small shear imposed on the model, the system with temperatures below the glass transition can be studied. Two methods based on the extended mode coupling theory were proposed to calculate the effective temperature, and they give the same results. As expected, the effective temperatures are higher than the bath temperatures. Since the shear rate is very small, the anisotropy is not obvious, and the effective temperatures along both the velocity gradient direction and the vorticity direction are the same.

Although our studies of different definitions have provided important insights into the ‘effective temperatures’ of nonequilibrium systems, there are still some questions remaining unsolved.

1. Why the effective temperatures of a strongly sheared system are direction-dependent? Is there any physical meaning? Since the temperatures are different along various directions, is there any heat flow inside

the system? What is the direction of the heat flow? To answer this question, it might be helpful to study a much larger system, so the effective temperatures of many different regions can be calculated and compared.

2. When a very large shear is imposed to the system, the average power supplied by the shear is large, while the energy dissipation caused by the fluctuation may be not as large as that injected into the system. In this case, defining an effective temperature based on the extended fluctuation-dissipation theorem may be questionable [1].

3. In chapter 3, the effective temperatures were defined in a very simple, and kind of naive way. The validation of the definitions needs to be examined carefully. In addition, for sheared glassy systems, the shear rate dependence of the effective temperature is necessary to be studied. Berthier et al. argued that one may get the effective temperature for the corresponded aging glass, when the shear rate is continuously reduced to approach zero [2]. Given that there are multiple relaxation time scales for the aging glass, in each time scale, there exists an effective temperature. The question is which one is equal to $T_{\text{eff}, \dot{\gamma} \rightarrow 0}$?

4. As shown in chapter 3, the effective temperature can control the density distribution even outside the linear response regime. Can the effective temperature also be used to describe the thermodynamic properties of the system, such as the entropy and energy?

5.2 Dynamic behavior of glass-forming liquids

The main topic of chapter 3 and 4 is on the dynamic behavior of glass-forming liquids. It is commonly accepted that it is the dynamic constrain, (not the static disorder or frustration), that causes the glass-forming processes [3].

In chapter 3, the Kob-Andersen binary Lennard-Jones mixture was simulated at various temperature with Brownian dynamics simulation. A small shear ($\dot{\gamma} = 0.01$) was imposed on the system. Many dynamic quantities, such as the mean square displacement, diffusion coefficient, self-intermediate scattering function, α -relaxation time, and van Hove function were calculated. The validation of Stokes-Einstein relation was checked. Above the glass transition, the effect of the small shear is limited. The dynamic behavior is mainly controlled by the temperature. The diffusive motion of particles slow down, and the relaxation time increases. The violation of Stokes Einstein relation is observed, showing that the dynamics is spatially heterogeneous. Dynamic heterogeneity is also evident from the self-part of the van Hove function. On the other hand, below the glass transition, the system is not frozen into the glass state, but it is still in a liquid-like state even at very low temperature ($T = 0.0$) due to the imposed shear. Extra energy is injected into the system by the shear flow, causing accelerated diffusion of particles and faster structural relaxation of the system.

Furthermore, the Stokes-Einstein relation is restored, and dynamics crosses over from heterogeneous behavior to homogeneous manner.

In chapter 4, a binary hard-sphere mixture introduced by Brambilla et al. [4] was simulated with a standard Monte Carlo algorithm [5]. An average overlap function $F_o(a, t)$, defined by equation 4.6, was calculated. Various parameters a were chosen as ‘measuring sticks’, some four-point correlation functions were measured for the systems with different volume fractions. The a -dependent behavior of these four-point correlation functions at the alpha relaxation time was analyzed. Specifically, the four-point susceptibility expressed by equation 4.14 remains constant when the parameter a is large enough, indicating that the strength of dynamic heterogeneity is almost independent of the ‘measuring stick’. The four-point structure factors were fitted by the Ornstein-Zernicke function, and the dynamic correlation lengths ($\xi(\tau_\alpha(\phi, a))$) were estimated. Although their statistics are poor, $\xi(\tau_\alpha(\phi, a))$ are roughly independent of a when a is larger than 0.6. The value of $\xi(\tau_\alpha(\phi, a \geq 0.6))$ is consistent with ξ_{\max} obtained at $a = 0.3$ [6]. The envelope fits of the four-point pair correlation functions also show that the dynamic correlation lengths ($\xi(\tau_\alpha(\phi, a))$) are independent of the ‘measuring stick’ a .

When a system is approaching the glass transition, either by reducing its temperature (chapter 3) or by compressing (chapter 4), dynamic heterogeneity is a robust feature. With the self-part of the van Hove function, the heterogeneous dynamics can be analyzed qualitatively. The following question is how to measure dynamic heterogeneity quantitatively? Different methods have been proposed. For example, Eaves and Reichman [7] suggested the following equation,

$$D \sim \tau^{1+\omega} , \tag{5.1}$$

where ω is called the violation exponent, which is zero if the Stokes Einstein relation is valid. This quantity can be used to measure dynamic heterogeneity [7]. On the other hand, the four-point susceptibility is widely employed to probe the strength of dynamic heterogeneity recently. The details have been discussed in chapter 4. Both methods should be explored for the same system, and the probable relation between them needs to be found.

In addition to the strength, the time scale characterizing dynamic heterogeneity need to be investigated. To find the time scale, several critical times listed in the table are worthy to be checked.

Rotman et al. pointed out that $\tau(\chi_4)$ is different from $\tau(\xi_{\max})$ [8]. In the previous work, Flenner et al. [6] also found that $\tau(\xi_{\max})$ is larger than τ_α when the parameter a equals 0.3. Thus these critical times are not the same. There are several questions regarding them. Are there any relations between them? Which one can be chosen as a characteristic time of dynamic heterogeneity? (Or none of them?) Generally speaking,

Table 5.1: Critical times during the glass transition

times	description
τ_α	α relaxation time
$\tau(\chi_4)$	the four-point susceptibility arrived at the maximum
$\tau(\xi_{\max})$	the correlation length reaches the plateau

what are the relations between these times and the lifetimes of clusters of immobile particles and mobile particles? Do immobile clusters and mobile clusters have the same lifetime?

After considering the time scales, let us think about the dynamic correlation length at these critical times. For a fixed parameter a , $\xi(a, t)$ increases with time and reaches a plateau at the time τ_{\max} . When a is small, τ_{\max} is large than the α relaxation time; thus ξ_{\max} is larger than $\xi_{\tau_\alpha(\phi, a)}$ [6]. As a grows, both times increase. We further speculate that τ_α climbs faster. As a consequence, τ_{\max} becomes smaller than τ_α and $\xi_{\tau_\alpha(\phi, a)}$ is equal to ξ_{\max} , when a is larger than 0.6. According to the results discussed in chapter 4, it is very possible that the maximum of the correlation length (ξ_{\max}) is independent of the choice of ‘ruler’ a . To verify these speculations, the time dependent behavior of the four-point susceptibility will be studied, and other ‘rulers’ (with different a values) will be used. Moreover, the dependences of $\tau(\xi_{\max})$ and $\tau(\chi_4)$ on the parameter a need to be tested, since it may help to figure out which one is a proper ‘measuring stick’.

Before closing the summary, there are some more general questions regarding the dynamics of glass-forming liquids need to be considered carefully. What are the relations between the dynamic correlation length scales, time scales and the strength of dynamic heterogeneity? How to connect the dynamic correlation length and the size of cluster of mobile particles and that of immobile particles? Why does dynamic heterogeneity happen during the glass transition? In chapter 4, four-point correlations were calculated to study dynamic heterogeneity of the system. Other multi-point correlation functions also need to be considered to probe the system, and may help to figure out the reason causing dynamic heterogeneity [9]. Furthermore, it is interesting to consider the effects of shear on the dynamics of a glass former. As shown in chapter 3, shear tends to stop heterogeneity and to restore homogeneity. In this case, one can also expect that the dynamic correlation length decreases due to shear. Can we find an equation to describe the shear dependence of the dynamic length scales? Can we find a quantitative relation between the strength of dynamic heterogeneity and shear rate? How to relate the effective temperature to the correlation time, length scales and even dynamic heterogeneity? To figure out these questions, the project reported in chapter 3 needs to be extended, the system under various shear rates needs to be studied. Multi-point correlation functions are necessary to be defined and calculated. I certainly expect that the results reported in my thesis

and the questions proposed here can trigger an enormous activity encompassing theoretical, numerical, and also experimental work, trying to further understand the effective temperature of nonequilibrium systems and the dynamics of glass-forming liquids.

Bibliography

- [1] I. K. Ono, C. S. O'Hern, D. J. Durian, S. A. Langer, A. J. Liu, and S. R. Nagel, *Phys. Rev. Lett.* *89*, 095703 (2002).
- [2] L. Berthier, J.-L. Barrat, and J. Kurchan, *Phys. Rev. E* *61*, 5464 (2000).
- [3] J. P. Garrahan and D. Chandler, *Phys. Rev. Lett.* *89*, 035704 (2002).
- [4] G. Brambilla, D. El Masri, M. Pierno, L. Berthier, L. Gipelletti, G. Petekidis, and A. B. Schofield, *Phys. Rev. Lett.* *102*, 085703 (2009).
- [5] L. Berthier and W. Kob, *J. Phys.: Condens. Matter* *19*, 205130 (2007).
- [6] E. Flenner, M. Zhang, and G. Szamel, *Phys. Rev. E* *83*, 051501 (2011).
- [7] J. D. Eaves and D. R. Reichman, *PNAS* *106*, 15171 (2009).
- [8] Z Rotman and E. Eisenberg, *Phys. Rev. Lett.* *105*, 225503 (2010).
- [9] L. Berthier, G. Biroli, J. -P Bouchaud, W. Kob, k. Miyazaki, and D. R. Reichman, *J. Chem. Phys.* *126*, 184503 (2007).